Synthesis and characterization of MOFs, COFs and HOFs for selective gas adsorption and separation

Dissertation

Zur Erlangung des Doktorgrades
Dr. rer. nat.
der Mathematisch-Naturwissenschaftlichen Fakultät
der Heinrich-Heine-Universität Düsseldorf

vorgelegt von

Robert Oestreich

Aus Düsseldorf

Düsseldorf, Januar 2026

aus dem Institut für Anorganische Chemie und Strukturchemie I
der Heinrich-Heine-Universität Düsseldorf

Gedruckt mit der Genehmigung der
Mathematisch-Naturwissenschaftlichen Fakultät der
Heinrich-Heine-Universität Düsseldorf

1. Berichterstatter: Univ.-Prof. Dr. Christoph Janiak
2. Berichterstatter: Univ.-Prof. Dr. Christian Ganter

Tag der mündlichen Prüfung:

Eidesstattliche Erklärung

Ich, Herr Robert Oestreich, versichere an Eides statt, dass die vorliegende Dissertation von mir selbstständig und ohne unzulässige fremde Hilfe unter Beachtung der „Grundsätze zur Sicherung guter wissenschaftlicher Praxis“ an der Heinrich-Heine-Universität Düsseldorf erstellt worden ist. Die aus fremden Quellen direkt oder indirekt übernommenen Gedanken sind als solche kenntlich gemacht. Die Arbeit wurde bisher weder im Inland noch im Ausland in gleicher oder ähnlicher Form einer anderen Prüfungsbehörde vorgelegt. Es wurden keine früheren erfolglosen Promotionsversuche unternommen.

……

Ort, Datum

……..

Unterschrift

Danksagung

An dieser Stelle möchte ich mich zunächst bei Herrn Prof. Dr. Christoph Janiak bedanken, der mir die Chance gegeben hat, hier meine Doktorarbeit zu schreiben und mich dabei trotz zahlreicher Probleme unterstützt hat.
Weiterhin möchte ich mich bei Herrn Prof. Dr. Christian Ganter bedanken, der sich mir freundlicherweise als Zweitkorrektor angeboten hat.
Vielen Dank auch an alle meine Mitarbeiter, aktuelle und bereits weitergezogene, mit denen ich manche schöne Stunde und interessante Diskussion hatte. Dies gilt ebenso für die Festangestellten, die bei den vielen auftretenden Problemen, Fragen und Nachfragen stets hilfsbereit waren.
Und natürlich danke ich auch meinen Freunden (besonders Malte, der diesmal viel Hilfestellung geleistet hat) und meiner Familie, die mich stets unterstützt haben.

Die vorliegende Arbeit wurde in der Zeit von Dezember 2020 bis Januar 2026 an der Heinrich-Heine-Universität Düsseldorf im Institut für Anorganische Chemie und Strukturchemie I im Arbeitskreis von Prof. Dr. Christoph Janiak angefertigt.

Table of Contents

I. List of Publications

Publications as shared first author:

Xu, K.;‡ **Oestreich, R.**;‡ Haj Hassani Sohi, T.;‡ Lounasvuori, M.; Ruthes, J. G. A.; Zorlu, Y.; Michalski, J.; Seiffert, P.; Strothmann, T.; Tholen, P.; Ozgur Yazaydin, A.; Suta, M.; Presser, V.; Petit, T.; Janiak, C.; Beckmann, J.; Schmedt auf der Günne, J. & Yücesan, G.

Polyphosphonate covalent organic frameworks

Nature Communications, Springer Science and Business Media LLC, **2024**, 15. DOI: 10.1038/s41467-024-51950-1

Oestreich, R.; Fetzer, M. N. A.; Zhang, Y.; Schreiber, A.; Knebel, A.; Suta, M.; Janiak, C.; Hanna, G. & Yücesan, G.

Stable Ultramicroporous Metal–Organic Framework with Hydrophilic and Hydrophobic Domains for Selective Gas Adsorption

Angewandte Chemie International Edition, Wiley, **2025**, 64. DOI: 10.1002/anie.202513788

Publications as co-author:

Monjezi, B. H.; Sapotta, B.; Moulai, S.; Zhang, J.; **Oestreich, R.**; Ladewig, B. P.; Müller-Buschbaum, K.; Janiak, C.; Hashem, T. & Knebel, A.

Metal-Organic Framework MIL-68(In)-NH_2 on the Membrane Test Bench for Dye Removal and Carbon Capture

Chemie Ingenieur Technik, Wiley, **2022**, 94, 135-144. DOI: 10.1002/cite.202100117

Fleck-Kunde, T.; Wolpert, E. H.; zur , L. z.; Oestreich, R.; Janiak, C.; Jelfs, K. E. & Schmidt, B. M. Observation of Rare Tri^6Di^9 Imine Cages Using Highly Fluorinated Building Blocks Organic Materials, Georg Thieme Verlag KG, **2022**, 4, 255-260. DOI: 10.1055/a-1977-1765

Woschko, D.; Millan, S.; Ceyran, M.-A.; **Oestreich, R.** & Janiak, C. Synthesis of a Chiral 3,6T22-Zn-MOF with a T-Shaped Bifunctional Pyrazole-Isophthalate Ligand Following the Principles of the Supramolecular Building Layer Approach Molecules, MDPI AG, **2022**, 27, 5374. DOI: 10.1039/D2CE01170K

Gvilava, V.; Vieten, M.; Oestreich, R.; Woschko, D.; Steinert, M.; Boldog, I.; Bulánek, R.; Fokina, N. A.; Schreiner, P. R. & Janiak, C.
A diamantane-4,9-dicarboxylate based UiO-66 analogue: challenging larger hydrocarbon cage platforms
CrystEngComm, Royal Society of Chemistry (RSC), **2022**, 24, 7530-7534.
DOI: 10.1039/D2DT03719J

Woschko, D.; Yilmaz, S.; Jansen, C.; Spieß, A.; Oestreich, R.; Ntep, T. J. M. M. & Janiak, C.
Enhanced sorption in an indium-acetylenedicarboxylate metal–organic framework with unexpected chains of *cis*-μ-OH-connected {InO_6}octahedra
Dalton Transactions, Royal Society of Chemistry (RSC), **2023**, 52, 977-989.
DOI: 10.1039/D2DT03719J

Lu, Y.; Liu, Y.-X.; Wang, Y.; **Oestreich, R**.; Xu, Z.-Y.; Zhang, W.; Hügenell, P.; Janiak, C. & Yang, X.-Y. A facile spray-pressing synthesis approach for reusable photothermal masks iScience, Elsevier BV, **2023**, 26, 107286.
DOI: 10.1016/j.isci.2023.107286

Gvilava, V.; Vieten, M.; Heinen, T.; **Oestreich, R**.; Boldog, I. & Janiak, C. [$Zr_6(\mu_3\text{-}O)_4(\mu_3\text{-}OH)_4$](1-adamantanecarboxylate)$_{12}$]: a model for extrinsic “defect-engineerable” porosity
Zeitschrift für anorganische und allgemeine Chemie, Wiley, **2023**, 649.
DOI: 10.1002/zaac.202300106

Beglau, T. H. Y.; Rademacher, L.; **Oestreich, R**. & Janiak, C.
Synthesis of Ketjenblack Decorated Pillared Ni(Fe) Metal-Organic Frameworks as Precursor Electrocatalysts for Enhancing the Oxygen Evolution Reaction
Molecules, MDPI AG, **2023**, 28, 4464.
DOI: 10.3390/molecules28114464

Apostol, A. A.; **Oestreich, R.**; Maxim, C.; Romanitan, C.; Badea, M.; Janiak, C. & Andruh, M. Nano-Sized Channels Resulting from the Packing of Discrete 3d–4f Metal Complexes in Crystals Crystal Growth & Design, American Chemical Society (ACS), **2023**, 23, 3740-3746.
DOI: 10.3390/molecules28062716

Hassan, Z. M.; Guo, W.; Welle, A.; **Oestreich, R**.; Janiak, C. & Redel, E. Formation of Gold Nanoclusters from Goldcarbonyl Chloride inside the Metal-Organic Framework HKUST-1

Molecules, MDPI AG, **2023,** 28, 2716.

DOI: 10.1039/D3DT03695B

Abdpour, S.; Fetzer, M. N. A.; **Oestreich, R**.; Beglau, T. H. Y.; Boldog, I. & Janiak, C. Bimetallic CPM-37(Ni,Fe) metal–organic framework: enhanced porosity, stability and tunable composition

Dalton Transactions, Royal Society of Chemistry (RSC), **2024**, 53, 4937-4951.

DOI: 10.1039/D3DT03695B

David, T.; **Oestreich, R**.; Pausch, T.; Wada, Y.; Fleck-Kunde, T.; Kawano, M.; Janiak, C. & Schmidt, B. M. Fluorinated vs. non-fluorinated tetrahedral Tri^4Tri^4 porous organic cages for H_2, CO_2, and CH_4 adsorption

Chemical Communications, Royal Society of Chemistry (RSC), **2024**, 60, 14762-14765.

DOI: 10.1039/D4CC05277C

Jordan, D. N.; Müller, T.; **Oestreich, R**.; Strothmann, T.; Boldog, I. & Janiak, C.

Metal–Organic Azolate Frameworks with an Acetylene-bis-pyrazolate Linker: Assessing the Role of the Triple-Bond Spacer in Gas and Vapor Sorption

Crystal Growth & Design, American Chemical Society (ACS), **2024**, 24, 3837-3854.

DOI: 10.1021/acs.cgd.4c00165

Navid, S. S.; Hosseinzadeh, R.; **Oestreich, R**.; Abdpour, S.; Beglau, T. H. Y. & Janiak, C.

Calix[4]arene@MIL-101 as host@MOF for cage-in-cage pore space partitioning for enhanced CO_2 separation and catalysis

Journal of Materials Chemistry A, Royal Society of Chemistry (RSC), **2025**, 13, 3894-3902.

DOI: 10.1039/D4TA07357F

Maxeiner, M.; Maile, R.; Cuvalli, M.; Wolf, A.; Komal, A.; **Oestreich, R**.; Janiak, C.; Mandel, K.; Knebel, A. & Müller-Buschbaum, K.

NanoMOF-Based Multilevel Anti-Counterfeiting by a Combination of Visible and Invisible

Photoluminescence and Conductivity
Advanced Functional Materials, Wiley, **2025**.
DOI: 10.1002/adfm.202500794

Khotchasanthong, K.; Wannarit, N.; Díaz Torres, R.; Arayachukiat, S.; Kielar, F.; Dungkaew, W.; Rungtaweevoranit, B.; Kheawhom, S.; **Oestreich, R.**; Janiak, C. & Chainok, K. Carbon dioxide adsorption properties in 3D ultramicroporous diamondoid lanthanide-oxalate frameworks
Journal of Materials Chemistry A, Royal Society of Chemistry (RSC), **2025**, 13, 36091-36103
DOI: 10.1039/D5TA03285G

II. Kurzfassung

Polymere poröse Materialien, also MOFs (Metal-organic frameworks), COFs (covalent-organic frameworks) und HOFs (hydrogen-bonded organic frameworks), sind neuartige und vielseitige Materialien, deren chemische Eigenschaften und deren Variabilität, kombiniert mit den hohen Oberflächen durch die hohe Porosität, sie für eine Vielzahl von Anwendungen interessant machen. Die Charakterisierung der Oberflächeneigenschaften erfolgt dabei üblicherweise durch Gassorptionsmessungen, welche viele Informationen liefern können, besonders auch im Hinblick auf die Nutzung im Zusammenhang mit Gasen und diesbezüglicher Selektivität.

In einem ersten Paper wurde ein Vertreter einer neuartigen Familie kovalenter organischer Gerüste (COFs) vorgestellt, nämlich Pyrophosphonat-COFs, die über Pyrophosphonat-Verbindungen aufgebaut sind. Pyrophosphonat-COFs konnten durch eine einstufige Kondensationsreaktion des ladungsunterstützten, wasserstoffgebundenen organischen Gerüsts (HOF) GTUB5 synthetisiert werden, das aus Phenylphosphonsäure und 5,10,15,20-Tetrakis[p-phenylphosphonsäure]porphyrin aufgebaut ist. Das beschriebene Pyrophosphonat-COF, das wir GTUB5-COF nennen, wurde durch einfaches Erhitzen seines Zwei-Linker-HOF-Vorläufers GTUB5 ohne Verwendung chemischer Reagenzien synthetisiert. GTUB5-COF zeigte während der Gassorptionsmessungen eine gute Wasser- und Wasserdampfstabilität. Darüber hinaus wies GTUB5-COF eine außergewöhnliche elektrochemische Stabilität in 0,5 M Na_2SO_4-Elektrolyt in Wasser auf. Die Bildung von Pyrophosphonat-Bindungen beim Erhitzen wurde durch Kernspinresonanzspektroskopie mit magischem Winkel, Fourier-Transform-Infrarotspektroskopie und Massenspektrometrie in Verbindung mit thermischer Analyse bestätigt. Das kondensierte Produkt Pyrophosphonat-COF kann CO_2 effizient adsorbieren. Es hat einen günstigeren Adsorptionswärmewert für die CO_2-Abscheidung bei niedrigen Drücken, was es

zu einem geeigneten Kandidaten für die selektive CO_2-Abscheidung in Gegenwart von Wasserdampf macht. Die Absorption und Emission von GTUB5-COF wird durch lokalisierte Übergänge (Soret- und Q-Bänder) innerhalb der Porphyrin-Einheit gesteuert, was zu einer breitbandigen Fluoreszenz im nahen Infrarotbereich bei etwa 800 nm führt. Analysen der mittleren quadratischen Verschiebung bestätigten, dass beide Gase räumlich innerhalb der Poren eingeschlossen bleiben. Diese Ergebnisse unterstreichen die chemische Robustheit und hohe Selektivität von TUB41 als MOF, das sich für Anwendungen in der Gastrennung, der photokatalytischen Wasserspaltung und der CO2-Reduktion unter schwierigen Bedingungen eignet.

In dieser Arbeit wurde weiterhin die thermische und chemische Stabilität sowie das Gasadsorptionsverhalten eines Phosphonat-MOF mit gemischten Linkern, [Cu(4,4'-bpy)0,5(1,4-$NDPAH_2$)] (wobei bpy = Bipyridin und NDPAH4 = Naphthalindiphosphonsäure), genannt TUB41, untersucht. TUB41 weist eine bemerkenswerte chemische Stabilität über einen breiten pH-Bereich (1–11) auf und behält seine strukturelle Integrität auch nach zwei Jahren wiederholter Adsorptionszyklen und Aktivierung bei 80 °C unter Umgebungsfeuchtigkeit bei. Kryogene Adsorptionsversuche zeigten, dass die Poren von TUB41 selektiv Gase mit größeren kinetischen Durchmessern wie N_2 und Ar ausschließen, während sie bei erhöhten Temperaturen kleinere Moleküle wie CO_2 und H_2O aufnehmen. Die Adsorptionsenthalpien für CO_2 bei einer Beladung von 0,01 mmol g−1 und H_2O bei einer Beladung von 0,7 mmol g^{-1} betragen −41 bzw. −38 kJ mol^{-1}, was ihre starken Anziehungswechselwirkungen mit TUB41 unter verschiedenen Bedingungen widerspiegelt. Molekulardynamiksimulationen zeigen, dass CO_2-Moleküle unter dem Einfluss starker nichtbindender Wechselwirkungen eine geordnete Anordnung in den zentralen hydrophoben Bereichen der Poren einnehmen, während H_2O-Moleküle bevorzugt an die hydrophilen sekundären Bausteine binden. Analysen der mittleren quadratischen Verschiebung bestätigen, dass beide Gase räumlich innerhalb der Poren eingeschränkt bleiben. Diese Ergebnisse unterstreichen die Bedeutung von TUB41 als chemisch robustes und hochselektives MOF mit Potenzial für Anwendungen in der Gastrennung, der photokatalytischen Wasserspaltung und der CO_2-Reduktion unter schwierigen Bedingungen.
Darüber hinaus wurden in einigen Kooperationen zahlreiche poröse Verbindungen (MOFs mit integriertem Makrozyklus, fluorierte Käfigverbindungen, bimetallische MOFs, etc.) auf Ihre Gassorptionseigenschaften, Selektivitäten und Interaktionen bezüglich verschiedener Gase und Dämpfe charakterisiert.

III. Abstract

Polymeric porous materials, i.e., MOFs (metal-organic frameworks), COFs (covalent-organic

frameworks), and HOFs (hydrogen-bonded organic frameworks), are novel and versatile materials whose chemical properties and variability, combined with their high surface area due to high porosity, make them interesting for a wide range of applications. The surface properties are usually characterized by gas adsorption measurements, which can provide a wealth of information, especially with regard to their use in connection with gases and their selectivity in this context.

A first paper presented a representative of a novel family of covalent organic frameworks (COFs), namely pyrophosphonate COFs, which are built up from pyrophosphonate compounds. Pyrophosphonate COFs were synthesized by a one-step condensation reaction of the charge-assisted, hydrogen-bonded organic framework (HOF) GTUB5, which is built from phenylphosphonic acid and 5,10,15,20-tetrakis[p-phenylphosphonic acid]porphyrin. The pyrophosphonate COF described, which we call GTUB5-COF, was synthesized by simply heating its two-linker HOF precursor GTUB5 without the use of chemical reagents. GTUB5-COF exhibited good water and water vapor stability during gas adsorption measurements.

Furthermore, GTUB5-COF exhibited exceptional electrochemical stability in 0.5 M Na_2SO_4 electrolyte in water. The formation of pyrophosphonate bonds upon heating was confirmed by magic angle nuclear magnetic resonance spectroscopy, Fourier transform infrared spectroscopy, and mass spectrometry coupled with thermal analysis. The condensed product pyrophosphonate-COF can efficiently adsorb CO_2. It has a more favorable adsorption heat value for CO2 capture at low pressures, making it a suitable candidate for selective CO_2 capture in the presence of water vapor. The absorption and emission of GTUB5-COF is controlled by localized transitions (Soret and Q bands) within the porphyrin unit, resulting in broadband fluorescence in the near-infrared range at around 800 nm. Analysis of the mean square displacement confirmed that both gases remain spatially confined within the pores. These results underscore the chemical robustness and high selectivity of TUB41 as a MOF suitable for applications in gas separation, photocatalytic water splitting, and CO_2 reduction under harsh conditions.

This work also investigated the thermal and chemical stability as well as the gas adsorption behavior of a phosphonate MOF with mixed linkers, [Cu(4,4'-bpy)0.5(1,4-$NDPAH_2$)] (where bpy = bipyridine and NDPAH4 = naphthalenediphosphonic acid), called TUB41. TUB41 exhibits remarkable chemical stability over a wide pH range (1–11) and maintains its structural integrity even after two years of repeated adsorption cycles and activation at 80 °C under ambient humidity. Cryogenic adsorption experiments showed that the pores of TUB41 selectively exclude gases with larger kinetic diameters, such as N2 and Ar, while absorbing smaller molecules, such as CO_2 and H_2O, at elevated temperatures. The adsorption enthalpies for CO_2 at a loading of 0.01 mmol g^{-1} and H_2O at a loading of 0.7 mmol g^{-1} are −41 and −38 kJ mol^{-1}, respectively, reflecting their strong attractive interactions with TUB41 under

different conditions. Molecular dynamics simulations show that CO_2 molecules, under the influence of strong non-bonding interactions, adopt an ordered arrangement in the central hydrophobic regions of the pores, while H_2O molecules preferentially bind to the hydrophilic secondary building blocks.

Analyses of the mean square displacement confirm that both gases remain spatially confined within the pores. These results underscore the importance of TUB41 as a chemically robust and highly selective MOF with potential for applications in gas separation, photocatalytic water splitting, and CO_2 reduction under harsh conditions.

In addition, numerous porous compounds (MOFs with integrated macrocycles, fluorinated cage compounds, bimetallic MOFs, etc.) were characterized in several collaborations for their gas sorption properties, selectivities, and interactions with various gases and vapors.

IV. List of Abbreviations

a.s.	As synthesized, directly after synthesis
at.%	Atom percentage
AIMD	ab initio molecular dynamics
ATR-IR	Attenuated total reflection infrared spectroscopy
bpy	bipyridine
BET	Brunauer, Emmett and Teller
Calc	calculated
COD	Crystallography Open Database
COF	Covalent-organic framework
CTF	Covalent triazine network
deg.	degassed
DFG	Deutsche Forschungsgemeinschaft
DFT	Density Functional Theory
DQCT	Double Quantum Constant Time
DQ NMR	Double Quantum NMR
EDX	Energy dispersive x-ray spectroscopy
eq.	equivalents
et al.	Et alia
exp.	experimental
Fig.	Figure
GCMC	Grand Canonical Monte Carlo

$HDMA^+$	Dimethylammonium cations
HoA	Heat of Adsorption
HOF	Hydrogen-bonded organic framework
HR-TEM	High Resolution Transmission Electron Microscopy
IAST	Ideal Adsorbed Solution Theory
In-fum	Indium fumarate
IR	Infrared spectroscopy
IUPAC	International Union of Pure & Applied Chemistry
Lit.	Literature
MAS	Magic angle spinning
MD	Molecular dynamics
MIL	Matériaux de l'Institut Lavoisier
MOF	Metal-organic framework
MSD	Mean square displacement
$NDPAH_4$	Naphthalenediphosphonic acid
NMR	Nuclear magnetic resonance
NLDFT	Non-local density functional theory
p	pressure
PXRD	Powder X-ray diffraction
RDF	Radial distribution function
RT	Room temperature, 293 K
SBU	Secondary building unit
scd	super critically dried
SEM	Scanning electron microscopy
STEM	Scanning transmission electron microscopy
T	Temperature
TEM	Transmission electron microscopy
TGA	Thermogravimetric analysis
theo.	theoretical
TUB	Technische Universität Berlin
UiO	Universitetet i Oslo
UV	Ultraviolet (light)
VOC	Volatile organic compounds

VT-PXRD	Variable temperature powder X-ray diffraction
wt. %	weight-%
XPS	X-ray photoelectron spectroscopy

1. Introduction

1.1 Porous coordination polymers

MOFs (**M**etal-**o**rganic **f**rameworks) are a class of porous coordination polymers consisting of metal ions, known as SBUs (**s**econdary **b**uilding **u**nits), connected via organic linkers. These organic linkers coordinate to the metal ions for example by carboxylate, phosphonate, azide, or heterocyclic groups, forming 1-, 2-, or 3-dimensional networks. [1] [2] [3] [4]

They have gathered an ever-rising amount of interest, shown in the yearly increasing number of publications (Figure 1) and the recently awarded Nobel prize of chemistry 2025 for some of the founding fathers of the research field.

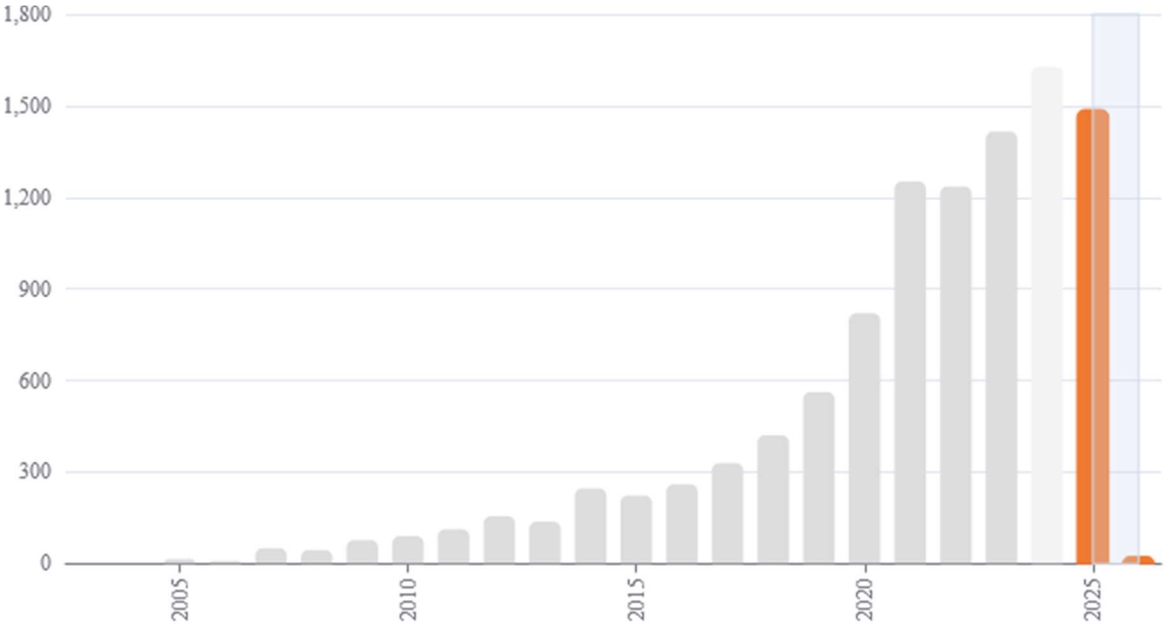

Figure 1: Yearly publications concernings MOFs according to SciFinder [5]

These materials offer a wide range of possible applications due to their high surface area, tunable pore size and volume, and sheer number of possible linker-SBU-combinations, presenting many different available chemistries. Possible uses include gas sorption [6] [7], gas separation [8], gas storage [9], sensor technology, ion exchange, hosts for drugs, nanoparticles, dyes and polymerization reactions, cooling applications, and catalysis. [10] [11]

Similarly, COFs (**C**ovalent **o**rganic **f**rameworks) build their network via covalent bonds while HOFs (**H**ydrogen bonded **o**rganic **f**rameworks) do so via hydrogen bonds. [12] [13] They offer similar application potentials as MOFs with also a very broad range of forms, while the different type of binding may lead to advantages, depending on final use. [14] [15] [16] [17] [18] [19]

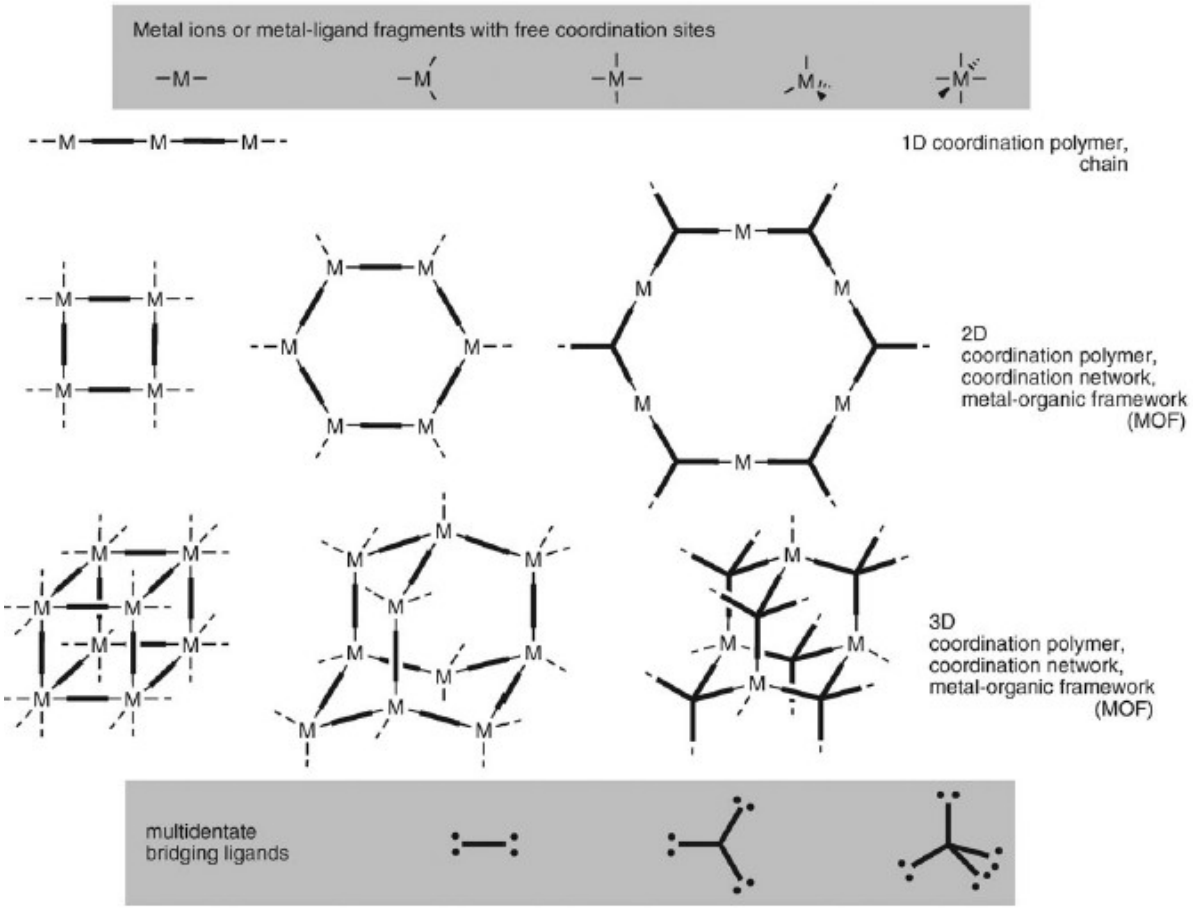

Figure 2: Schematic presentation of different MOF structures, reprinted with permission from [1] © Royal Society of Chemistry 1987

1.2 Gas adsorption

Adsorption is the process of gas (or fluid) atoms, ions or molecules, called adsorbate in the attached, and adsorptive in the fluid or gaseous state, attaching to a solid surface, the adsorbent. Alternatively, a gas could be adsorbed on a fluid film. In contrast to the related absorption, the adsorbate does not infiltrate the interior of the adsorbent. Bonding between adsorbate and adsorbent can be based on chemi- or physisorption. This work only deals with aspects of the physisorption of gases. [20]

Gas ad- and desorption is often used to characterize materials, especially porous solids and fine powders, and their surface properties. Gas sorption properties are important characteristics for materials for gas capture, gas separation and gas storage, heterogenous catalysis, batteries, drug delivery, or simply as a quick tool of quality control.

There are two main methods for the measurement of gas sorption properties, one based on direct

measurement of the uptaken gas by gravimetry, the other based on manometric measurements of the gas uptake by determining the amount removed from the gas phase. Independent of measurement method, before the measurement guest molecules have to be removed from the sample to empty pores and make adsorption of gas molecules possible. This activation step is crucial for precise and reproducible measurements. Usually it is performed under vacuum conditions and increased temperatures, which have to be high enough to remove solvent molecules, and possibly water adsorbed under ambient conditions, while not damaging the sample.

Equally, a sufficient amount of material has to be used to minimize weighing errors and guarantee adsorption high enough to be measured precisely with the equipment available, while too much material will lead to unnecessary long measurement times.

For the volumetric measurements known amounts of the adsorbtive gas are dosed into the measurement cell. After equilibrium has been reached, the pressure is measured and by comparison to the theoretical pressure without adsorbate the amount adsorbed by the sample is calculated.

Pore classes

Pores are usually distributed into macropores with widths larger than 50 nm, mesopores, whose widths lie between 2 and 50 nm, and micropores, which are even smaller. Micropores can be further subclassified into ultramicropores (width < 0.7 nm) and supermicropores (width 0.7-2 nm).

The most commonly used gas is nitrogen at cryogenic temperatures (77 K), due to its inertness, size, availability, prize and ease of measurement (usually using liquid nitrogen in a dewar for temperature control). The largest part of characterizations and measurements is done by this and most evaluation methods, at least initially, are based on its use. [20]

1.3 Isotherm types

The shape of the isotherm recorded gives information about the material properties. The most important classification is that by IUPAC, first published by Sing et al. in 1985 [21] and updated by Thommes et al. in 2015. [22]

Type I (a) and (b) show a reversible course, a steep increase in the low pressure region and reach a plateau value afterwards. This type is characteristic for microporous materials, where adsorbent-adsorbate interactions cause a fast adsorbate uptake. For measurements with nitrogen and argon at cryogenic temperatures, 77 K and 87 K respectively, Type I (a) is characteristic for materials with narrow micropores (width < $\sim$ 1 nm), while Type I (b), with a slower rise in the beginning, stems from a wider pore size distribution and pores of a width of up to $\sim$ 2.5 nm. [22]

Type II isotherms are characteristic for macroporous or nonporous materials and show a reversible

progression. Especially important is the point B, which marks the finished monolayer coverage in the case of a sharp knee. If this point is less distinctive this difference cannot be clearly determined from the isotherm. The adsorbed amount seems to increase limitlessly with p/p_0 approaching 1. [22]

Type III isotherms in contrast show no discernible Point B and thus no identifier for the completion of monolayer formation. Adsorbent-adsorptive interactions are relatively weak and clusters form around the most favourable sites of nonporous or macroporous solids. At saturation point a limit is reached. [22]

Type IV isotherms stem from mesoporous materials. Both the adsorbent-adsorptive interactions and intermolecular forces in the condensed phase determine the adsorption behaviour. After formation of a monolayer, condensation inside the pores follows. In the case of IV (a) isotherms capillary condensation coincides with hysteresis. For this to happen, the pore widths have to exceed a certain critical width dependent on the combination of adsorbate, adsorbent and temperature (for example for nitrogen and argon at cryogenic temperatures hysteresis occurs for cylindrical pores wider than ca. 4 nm). [23] [24] Smaller widths lead to reversible isotherms without hysteresis. [22]

Type V isotherms have a similar shape as Type III in the low p/p0 range, because they also show weak adsorbent-adsorbate interactions. At higher pressures molecular interactions of the adsorbate lead to pore condensation and a quick rise in the amount adsorbed. [22]

Finally, Type VI isotherms are observed in the case of layer-by-layer adsorption on highly uniform nonporous surfaces, with the height of singular steps correlating with the layer capacity and sharpness of the steps depending on system and temperature. [22]

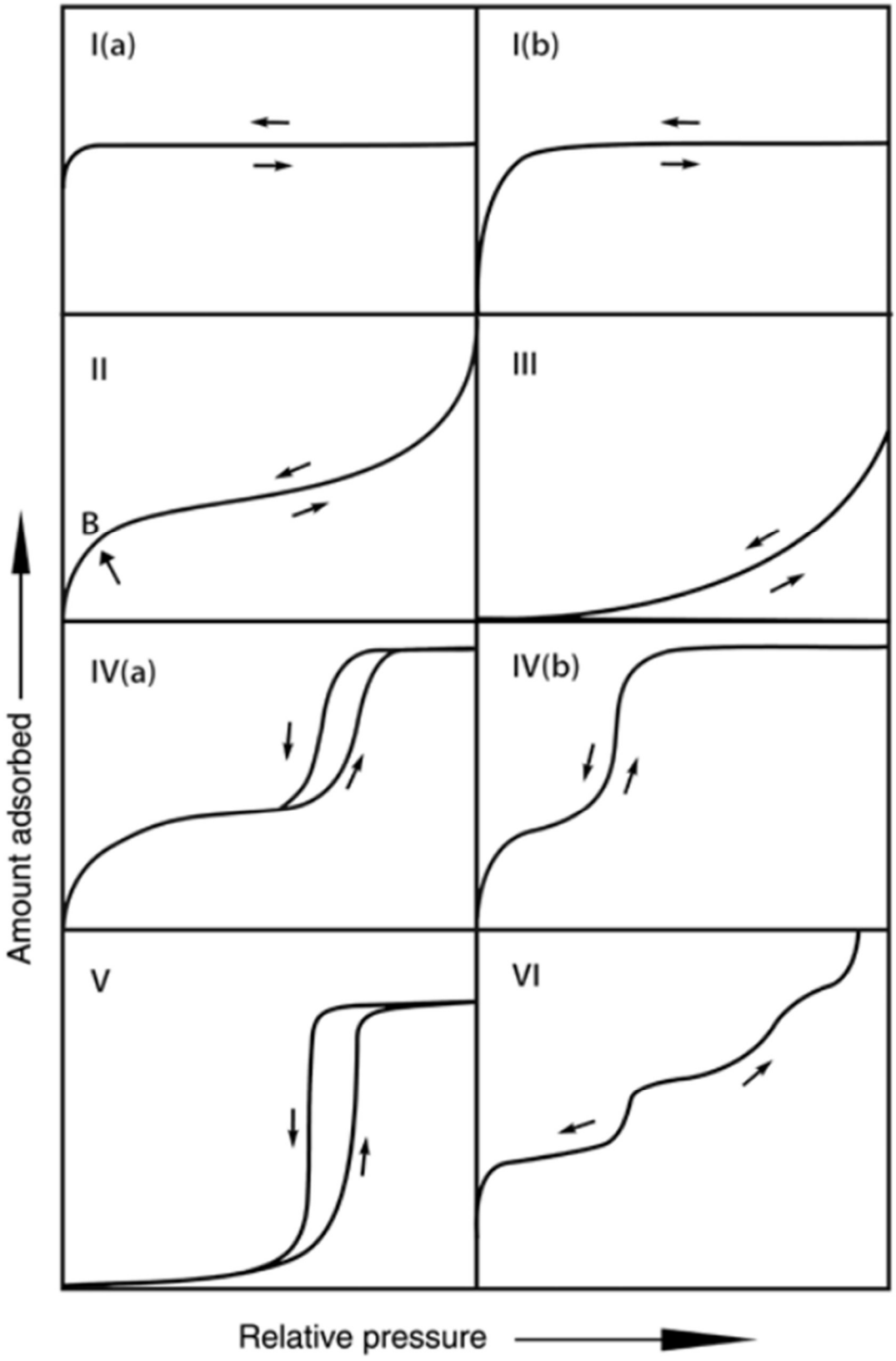

Figure 3: Isotherm types according to IUPAC [22], reprint with permission by © IUPAC & De Gruyter 2015

1.4 Desorption and Hysteresis

Hysteresis in isotherms on the most basic level shows, that ad- and desorption follow different pathways, usually associated with capillary condensation. Metastable adsorption and/or network effects are the usual underlying reasons. For open-ended pores, for example cylindrical ones, metastability of the adsorbed multilayer can lead to delayed condensation and hinder the reaching of equilibrium on the adsorption branch. Evaporation, as the equivalent of a reversible liquid-vapour transition, does not involve nucleation and the desorption branch is thus in thermodynamic equilibrium. [24] [25]

In materials with complex pore structures, for example with blocked pores or network effects, desorption can be influenced. One specific phenomenon occurs with wide pores with narrow necks (e.g., ink-bottle pore shape): The pore filling happens as before, but the desorption is dependent on the necks and occurs thus at a lower pressure and leads to a hysteresis. For networks, diameter and spatial distribution of pore necks effects desorption and cause, for sufficiently large neck sizes, a coordinated emptying of the pores at a characteristic relative pressure. By this, inferences can be made from the desorption curve regarding the pore necks.

Both theoretical and experimental studies were conducted to explore the desorption mechanism in porous materials. It was found, that neck sizes smaller than an adsorbate specific value (estimated as roughly 5-6 nm for nitrogen at cryogenic temperatures), combined with larger pores, show a desorption mechanism involving cavitation, the formation and growth of gas bubbles within the metastable condensed fluid. In this case no quantitative inferences regarding neck sizes can be gained from the desorption curve. [22]

6 distinct hysteresis shapes, linked to a particular kind of pore structure and adsorption mechanism, have been classified by IUPAC (see Figure 4). [22]

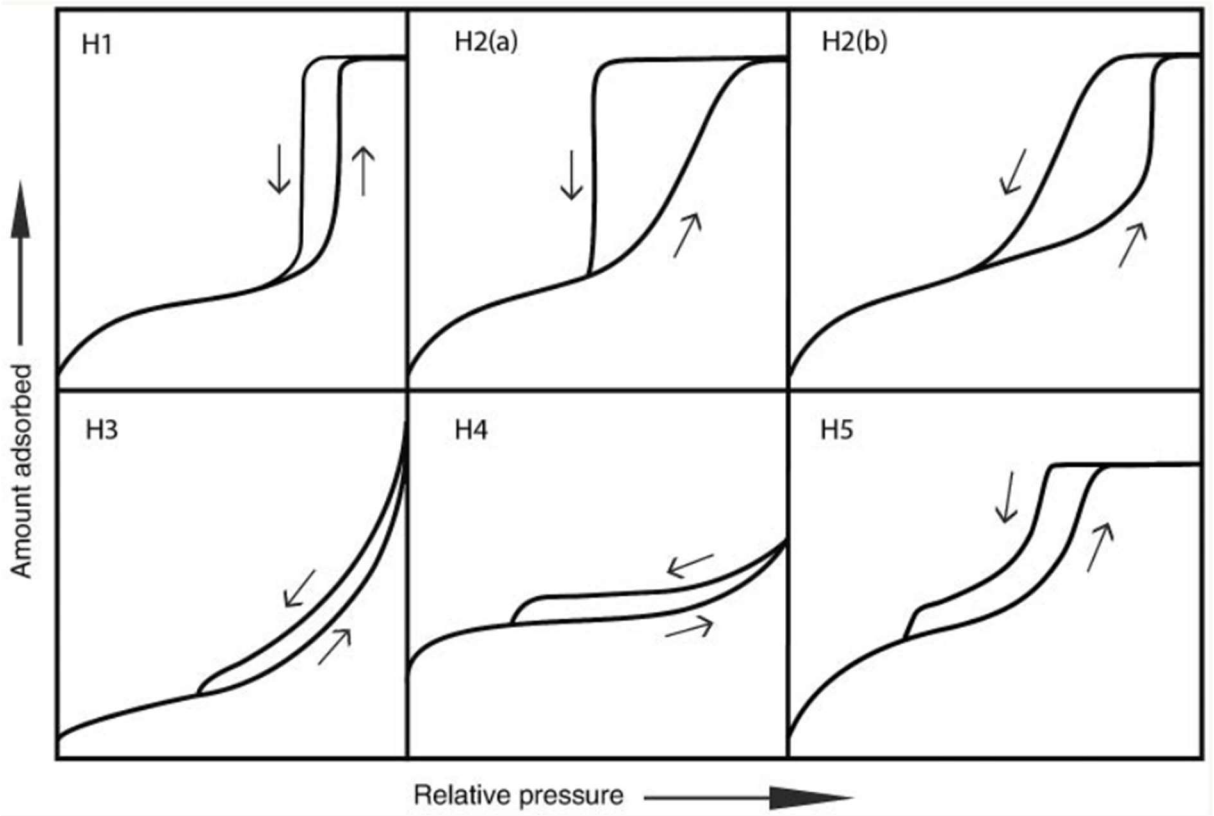

Figure 4: Hysteresis shapes according to IUPAC [22], reprint reprint with permission by © IUPAC & De Gruyter 2015

Type H1 is typical for solids with a narrow pore size distribution of mesopores, but can also be seen in networks of ink bottle pores. Network effects are irrelevant and the loop with a steep gradient of both adsorption and desorption curve, close to each other, shows the delayed condensation in the mesopores during adsorption. [22]

More complicated pore structures with significant network effects show hysteris loops of Type H2. H2(a) is marked by a precipitious gradient of the hysteresis desorption loop, attributable to either pore -blocking/percolation of a narrow range of neck sizes or evaporation characterized by cavitation. H2(b) is typical for a much broader neck size distribution while still being connected to pore blocking. [22]

H3 types are marked by a Type (II) adsorption branch (see above) and a lower end of the loop determined by the relative pressure necessary for cavitation formation.

Type H4 is similar, but the adsorption branch now resembles a mixture of Type I and Type II, with a steep uptake increase at low relative pressures due to micropores.

The unusual Type H5 loop is connected to pore structures with both open and partially blocked mesopores. [22]

The steep fall of the desorption branch of Types H3, H4 and H5 is common to all of them and the position on the x-axis is usually defined by temperature and adsorbate, for example p/p0 is roughly

0.4-0.5 for nitrogen at 77 K. [22]

1.5 Analysis of gas sorption isotherms

Besides just characterizing the shapes of isotherms, many different ways to analyze the results have been developed over the last century. A few important ones are explained in a little bit more detail below.

1.5.1. Brunauer-Emmett-Teller – BET

The Brunauer-Emmett-Teller method is still the most common way to access the surface area of porous materials and fine powders, despite several known issues. Only for nonporous, macroporous or mesoporous solids with well-defined isotherms (Type II or Type IV (a) a "true" surface area can be determined. Despite this limitation it is widely used for all kinds of materials and the values gained still allow some comparison between materials and quality control, but it's important to keep in mind, that for all other conditions, and especially microporous materials, the value is only the apparent surface area. [23] [26] [27]

To use the BET method, the isotherm first has to be transformed into the "BET-plot", from which the monolayer capacity, n_m, is calculated. By multiplication with the corresponding molecular cross-sectional area σ of the used adsorptive a surface area can be calculated. The linear form of the BET equation is this

$$\frac{p/p^0}{n(1-\frac{p}{p^0})} = \frac{1}{n_m} + \frac{C-1}{n_m C}(\frac{p}{p^0}) \quad (1)$$

where n is the specific amount adsorbed at the relative pressure p/p^0, n_m is the specific monolayer capacity and C is exponentially related to the energy of monolayer adsorption. To derive n_m from the BET equation, the linear relation between $(p/p^0)/n(1-p/p^0)$ and p/p^0 is used. When put into a graph, this is called the BET plot. It is important to choose only that area of the graph, where this equation gives a good fit and C is positive. The traditional range lies between a relative pressure of 0.05 and 0.3, usually for type II and type IVa isotherms, but can vary depending on pore sizes and interactions [22].

1.5.2. NLDFT and GCMC

Non-localized density functional theory (NLDFT) and Grand Canonical Monte Carlo (GCMC) method have been developed as new ways to evaluate sorption results based on the increase in computational power available.

First steps were made by Evans and Tarazon, studying adsorption and fluid phases in pores through molecular modeling based on DFT (density functional theory). [28] [29] Seaton et al., based on that work, calculated pore size distributions. Since this method still had several issues, especially regarding micropores, NLDFT was developed by Lastoskie, Gubbins and Quirke [30] [31]. With this, adsorption of many adsorbents and adsorbates can be explained and then be used to calculate the pore size distribution. [32] One important feature of these theories is the assumption of a periodic chance of adsorption density from solid surfaces, in contrast to the classical assumption of liquid state adsorption (Kelvin theory). NLDFT uses a molecular-based statistical thermodynamic theory, which allows for a variety of factors to be included. For correct results, proper choice of these calculation parameters is essential. These include pore structure (slit, cylindrical or cage), temperature, adsorptive (e. g. N_2, Ar, CO_2) and adsorbent (e. g. carbon, zeolites).

Based on these parameters various theoretical isotherms are calculated and by minimizing deviation the best fit to the experimental isotherm is found, providing a full description of the pore structure. Erroneous choice of parameters invalidates the results. Since proper models for MOFs are often not available, all results have to be seen as approximations, but if a good fit can be found, that can still give some valuable information.

GCMC on the other hand, repeatedly defines the parameters (adsorptive molecule, adsorbent surface atom, pore diameter and shape, etc.), placing the virtual adsorptive molecule within the simulated pore, simulates movement and checks whether the step lead to a more stable system (negative energy) or not. With this whole process, GCMC practically performs an actual adsorption experiment. [33]

1.5.3. Enthalpy of adsorption

The isosteric enthalpy of adsorption, ΔH_{ads}, is defined as the heat to be released or required when an adsorptive binds to or detaches from the surface of an adsorbent. By measuring adsorption isotherms at different temperatures, close enough to each other to make the processes comparable (usually 10 K apart), and use of the Clausius-Clapeyron approach, this value can be determined. For a favourable binding, this value should be negative, and the higher the magnitude the stronger the binding. The

relevant equation is the Clausius-Clapeyron equation [34]:

$$\Delta H_{ads}(n) = -R * \ln(\frac{p_2}{p_1}) \frac{T_1 T_2}{T_2 - T_1} \quad (2)$$

R here is the ideal gas constant, p pressure and T temperature. To find the enthalpy of adsorption, points of equal adsorption amount have to found. Usually the actual isotherms don't offer enough points to make that feasible, thus a mathematic fit to the isotherms is necessary. Different models can be used for that, for example Langmuir, dual-site Langmuir, Toth, Sips, Freundlich-Langmuir or another fit. [35]

From the heat of adsorption one can estimate the strength of binding between adsorbent and adsorptive, compare this value between materials and also possibly gain an insight into different binding sites, in case of a strong change over the course of adsorption.

1.5.4. IAST

An easy method to evaluate selectivity of different gases in a mixture from single component isotherms, which is much easier to accomplish than working with mixed gases, is IAST (Ideal Adsorbed Solution Theory) . It was first published in 1965 by Myers und Prausnitz and offers predictions regarding multi-component gas mixtures from single-component adsorption isotherms, based on thermodynamic theories.

Three assumptions are made for this theory: Molecules in the adsorbate have equal access to the adsorbent, the adsorbent is homogenous and the adsorbate behaves as an ideal solution. [36] [37]

The reality is obviously more complex, but in many cases IAST predictions have shown good agreement with later experiments. [38] [39]

2. Motivation

The aim of this dissertation was to explore and understand the sorption properties of different porous materials, gases and vapours.

A multitude of materials was researched and the interactions with different gases over wide temperature ranges were measured and characterized.

A variety of analysis devices and methods were used and measurement conditions and procedures were optimized for each material to give optimal results and gain as much information as possible.

Special interest was paid to phosphonate compounds, which show promise for selective adsorptions of carbon dioxide, the most important greenhouse gas, under harsh conditions.

To properly characterize these materials, many different measurement methods had to be tested because of the difficulty of access to the pores for the gas molecules.

3. Cumulative Part

The following chapters show the results of the dissertation, which have been published with a first authorship in international journals. Publications are sorted by publication date. Each of them stands for itself, including its own references and its own order of figures, tables and schemes. Both publications will be introduced by title, author and journal names, a short summary and a marking of the author's contributions.

3.1 Polyphosphonate covalent organic frameworks

Ke Xu, **Robert Oestreich** und Takin Haj Hassani Sohi, Mailis Lounasvuori, Jean G. A. Ruthes, Yunus Zorlu, Julia Michalski, Philipp Seiffert, Till Strothmann, Patrik Tholen, Ozgur Yazaydin, Markus Suta, Volker Presser, Tristan Petit, Christoph Janiak, Jens Beckmann, Jörn Schmedt auf der Günne, Gündoğ Yücesan
Nature Communications **15**, Article number: 7862 (2024)
DOI: 10.1038/s41467-024-51950-1

Summary:
A polyphosphonate covalent organic framework (COF) constructed via P-O-P linkages was synthesized by a simple single-step condensation reaction from the HOF precursor material, which is composed of phenylphosphonic acid and 5,10,15-20-tetrakis[p-phenylphosphonic acid]porphyrin. The structural change is triggered by a simple heating procedure without additional chemical reagents. When a temperature of 210 °C is surpassed, an amorphous microporous polymeric structure is formed by oligomerization of P-O-P bonds. This could be confirmed by constant-time solid-state double-quantum ^{31}P nuclear magnetic resonance experiments. This polyphosphonate COF shows good water and water vapor stability during gas sorption measurements, and electrochemical stability in 0.5 M Na_2SO_4 electrolyte in water. This family of COFs fills an important gap in the literature in the form of stable microporous COFs suitable for use in water and electrolytes, accessible by an easy and sustainable synthesis route, and able to effectively capture CO_2 in its narrow pores.
Contributions to this work:

- Design of experiments, writing and check of manuscript iterations
- Measurement of gas and water sorption
- Stability tests
- Resynthesis of TUB5 for further measurements
- Organization of TEM measurements at Jülich
- Performance of optical measurements in collusion with Professor Suta
- Ke Xu performed the NMR characterization, generated the corresponding figures and contributed to the manuscript
- Professor Jörn Schmedt auf der Günne did the analysis of the DQ NMR experiments
- Takin Haj Hassani Sohi performed the PXRD work and the chemical stability testing
- Mailis Lounasvuori performed the temperature variable FT-IR measurements and wrote the corresponding section.
- Professor Jean G.A. Ruthes performed the SEM-EDX analysis and the electrochemical stability testing and wrote the corresponding section.
- Julia Michalski performed the XPS measurements and wrote the corresponding section.
- Philipp Seiffert performed the TGA experiments and Till Strothmann designed the TGA-MS experiments.
- Patrik Tholen synthesized reproduced GTUB5 to be used in this work.
- Yunus Zorlu synthesized the second batch of GTUB5 and contributed to the figures.
- A.Ozgur Yazaydin performed the DFT calculations and wrote the corresponding section.
- Professor Markus Suta performed the optical measurements and wrote the corresponding section.
- Volker Presser supervised the work of Jean G.A.Ruthes and contributed to the corresponding text.
- Tristan Petit supervised the FT-IR studies and contributed to the corresponding text.
- Professor Christoph Janiak supervised the gas sorption for BET measurements and edited the manuscript.
- Gündoğ Yücesan and Jörn Schmedt auf der Günne created the hypothesis, supervised the entire project and wrote the introduction and conclusion and edited the entire manuscript. Jens Beckmann provided helpful insights and discussions during the work and contributed to the manuscript
- Submission of the final manuscript at the international journal Nature Communications after final discussions with Doctor Yücesan and Professor Doctor Christoph Janiak

nature communications

Article

https://doi.org/10.1038/s41467-024-51950-1

Polyphosphonate covalent organic frameworks

Received: 29 February 2024

Accepted: 20 August 2024

Published online: 09 September 2024

Check for updates

Ke Xu[1,10], Robert Oestreich[2,10], Takin Haj Hassani Sohi[2,10], Mailis Lounasvuori[3], Jean G. A. Ruthes[4,5], Yunus Zorlu[6], Julia Michalski[2], Philipp Seiffert[2], Till Strothmann[2], Patrik Tholen[7], A. Ozgur Yazaydin[8], Markus Suta[2], Volker Presser[4,5], Tristan Petit[3], Christoph Janiak[2], Jens Beckmann[9], Jörn Schmedt auf der Günne[1] ✉ & Gündoğ Yücesan[2] ✉

Herein, we report polyphosphonate covalent organic frameworks (COFs) constructed via P-O-P linkages. The materials are synthesized via a single-step condensation reaction of the charge-assisted hydrogen-bonded organic framework, which is constructed from phenylphosphonic acid and 5,10,15,20-tetrakis[p-phenylphosphonic acid]porphyrin and is formed by simply heating its hydrogen-bonded precursor without using chemical reagents. Above 210 °C, it becomes an amorphous microporous polymeric structure due to the oligomerization of P-O-P bonds, which could be shown by constant-time solid-state double-quantum ^{31}P nuclear magnetic resonance experiments. The polyphosphonate COF exhibits good water and water vapor stability during the gas sorption measurements, and electrochemical stability in 0.5 M Na_2SO_4 electrolyte in water. The reported family of COFs fills a significant gap in the literature by providing stable microporous COFs suitable for use in water and electrolytes. Additionally, we provide a sustainable synthesis route for the COF synthesis. The narrow pores of the COF effectively capture CO_2.

Covalent organic frameworks (COFs) are microporous materials closely related to metal-organic frameworks (MOFs) and hydrogen-bonded organic frameworks (HOFs)[1–3]. COFs are synthesized via the covalent linkage of organic building blocks to form two or three-dimensional microporous frameworks[2]. Since the first report on boroxine-linked COFs in 2005[2], COF research has been a very active research area due to their tunable porosity and potential for pore functionalization via organic linker design or post-synthesis modifications[4]. To date, many different COF families have been reported in the literature based on their covalent linkage. COFs can be synthesized through a wide range of reactions, including condensation reactions (i.e., boroxine linkage), Schiff base reactions (i.e., imine, hydrazone, enamine, phenazine linkages), click reactions (i.e., triazole linkage), metal-catalyzed coupling reactions (i.e., C-C linkages), etc[5–9]. The vast structural diversity and porosity of COFs enable potential applications such as gas storage, water adsorption, catalysis, water harvesting, CO_2 capture, catalysis, photocatalysis, semiconductors, energy storage, and luminescence[5,10–15].

Recently, we have reported on the synthesis of hydrogen-bonded organic frameworks constructed using arylphosphonic acids[16,17]. Due

[1]Department of Chemistry and Biology, Inorganic Materials Chemistry, University of Siegen, Adolf-Reichwein-Straße 2, Siegen, Germany. [2]Institut für Anorganische Chemie und Strukturchemie, Heinrich-Heine-Universität Düsseldorf, Universitätsstraße 1, Düsseldorf, Germany. [3]Young Investigator Group Nanoscale Solid-Liquid Interfaces, Helmholtz-Zentrum Berlin für Materialien und Energie GmbH, Albert-Einstein-Straße 15, Berlin, Germany. [4]INM – Leibniz Institute for New Materials, Campus D22, Saarbrücken, Germany. [5]Department of Materials Science and Engineering, Saarland University, Campus D22, Saarbrücken, Germany. [6]Department of Chemistry, Gebze Technical University, Kocaeli, Türkiye. [7]Technische Universität Berlin, Lebensmittelchemie und Toxikologie, Gustav-Meyer-Allee 25, Berlin, Germany. [8]Department of Chemical Engineering, University College London, London, UK. [9]Institut für Anorganische Chemie und Kristallographie, Universität Bremen, Bremen, Germany. [10]These authors contributed equally: Ke Xu, Robert Oestreich, Takin Haj Hassani Sohi. ✉e-mail: gunnej@chemie.uni-siegen.de; guendog.yuecesan@hhu.de

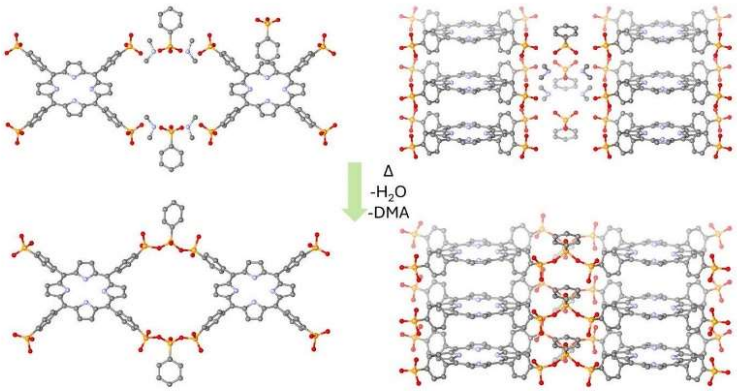

Fig. 1 | Synthesis route for forming the proposed polyphosphonate-COF GTUB5-COF. Heating of the precursor HOF GTUB5, which is constructed from phenylphosphonic acid and 5,10,15,20-tetrakis[p-phenylphosphonic acid] porphyrin and $HDMA^+$ cations leading to the partially condensed **GTUB5-COF** (proposed structure obtained by DFT calculations, hydrogen atoms are omitted for clarity), and the packing of aromatic porphyrin cores in GTUB5 (above) and GTUB5-COF (bottom).

to their short hydrogen bond distances around ca. 2.5 Å (at shorter than 2.4 Å of donor oxygen-acceptor oxygen pair distances involved in hydrogen bonds are considered to have ca. 50 kJ/mol bond dissociation energy[18]) and formation of multiple hydrogen bonds between the arylphosphonic acid linkers, these HOFs exhibited good stability at 90 °C and 90% relative humidity (RH) and after proton conductivity experiments at 75 °C and 75% RH. Other groups also reported the stability of phosphonic acid HOFs after proton conduction[19]. Our recent unit cell checks on the first batch of GTUB5 (derived from phenylphosphonic acid and 5,10,15,20-tetrakis[p-phenylphosphonic acid]porphyrin) crystals are still providing the same unit cell after 4 years of storage at room temperature and ambient humidity. In the literature, arylphosphonic acids resist thermal decomposition, hydrolysis, and decomposition under ultraviolet light[20]. Expectations on polyphosphonate-COFs, synthesized after condensation of phosphonic acid HOFs, are high stability and structural versatility. They are also expected to generate flexible pores due to flexible P-O-P bonds. Such flexible and stable microporous platforms have the potential to spawn realistic industrial applications to capture gases selectively.

It has been recently shown that branched condensed phosphates exhibit good stability in water[21,22]. Hypothetically, organic diphosphonates and higher polymeric phosphonic acid anhydrides (polyphosphonates) are expected to create even better stability in water as compared to inorganic pyrophosphates as the P-O-P groups are located in between bulky organic moieties (such as the porphyrin linker as shown in this work). Furthermore, hydrolysis of phosphonate esters requires the presence of 37% HCl under reflux conditions to form the corresponding phosphonic acids, indicating a high stability of phosphonic acids in an acidic environment[23]. There is limited information in the literature about the condensation of phosphonic acids. For example, there are a few reports about the ab initio calculations studying the condensation of phosphinic acids and methylphosphonic acid to provide geometry and reaction energies to form dimers, trimers, tetramers, and cyclization[24,25]. There are also only few experimental reports in the literature reporting the condensation of phosphonic acid to form dimers, that is, diphosphonates. For example, a proton-conducting polymer poly(vinyl phosphonic acid) is known to condense forming dimers at higher temperatures, which limits its proton-conducting ability. There is another study by Yücesan et al. that reports the crystal structure of solvothermally condensed phenyl phosphonic acid in acetonitrile at 150 °C, at which the respective product generates a metallomacrocycle with Cu(II) ions and 2,2′-bipyridine[26]. A similar work utilizing condensing agents was reported later by Zheng using Ag(I) ions[27,28]. The other reports in the literature about the formation of phosphonate dimers, trimers or macrocycles were synthesized using methods, such as ring-opening polymerization of cyclic phosphonates[29,30]. In this work, we used our previously reported charge-assisted HOF GTUB5 as a model system to form the polymeric phosphonic anhydride-COF, namely a polyphosphonate-COF formed by condensation of the phosphonic acids phenylphosphonic acid and 5,10,15,20-tetrakis[p-phenylphosphonic acid] porphyrin by simple heating (Fig. 1). Furthermore, we report the structural characterization of a polyphosphonate-COF and explore its thermal, chemical, and electrochemical stability, CO_2 capture, water harvesting, and optical properties.

Results and Discussion

Synthesis and characterization of phosphonic acid anhydrides

As seen in Fig. 1, the donor-acceptor O-O distances between hydrogen-bonded phosphonic acid moieties of GTUB5 is ca. 2.5 Å, which is slightly higher than 2.4 Å. Hydrogen bonds with shorter donor-acceptor O-O distances than 2.4 Å can have high bond dissociation energies up to 50 kJ/mol[18] (for more detailed information about the hydrogen bond lengths in phosphonic acids, see refs. 16 and 17). Therefore, the phosphonic acid groups in GTUB5 crystals are aligned in a favorable position to initiate the condensation reaction[16,17]. Furthermore, $HDMA^+$ (dimethylammonium cations) might act as a condensing agent during the heating. The charge-assisted hydrogen-bonded network of GTUB5 with the presence of fully deprotonated phenylphosphonic acid moieties and $HDMA^+$ cations could hypothetically help promote the condensation reaction following the nucleophilic substitution on 5,10,15,20-tetrakis[p-phenylphosphonic acid]porphyrin and fully deprotonated phenylphosphonic acid phosphorus atoms. Thermogravimetric analysis (TGA) coupled with mass spectrometry (MS) of GTUB5 and FT-IR suggests condensation of HOF begins after ca. 130 °C due to evaporation of water and continues until ca. 230 °C. The solid crystals of GTUB5 were heated gradually in an oven to 270 °C to promote the condensation of phosphonic acids to form polyphosphonate units. As detailed below, the GTUB5-COF retained its crystallinity until 210 °C. At this stage, GTUB-COF linkages consist of condensed diphosphonates. The crystals retained their initial color and shape at higher temperatures after heating to 230 °C and 270 °C. Despite the crystalline look of the final product GTUB5-COF, as we discuss below, the samples are X-ray amorphous due to further oligomerization of condensed polyphosphonates.

Evidence for P-O-P bonds by MAS NMR

Motivated by the amorphous state of the material produced by annealing at 270 °C, we used solid-state ^{1}H, ^{13}C, and ^{31}P NMR spectroscopy to monitor the structural changes induced by heating between the arylphosphonic acid linkers in GTUB5 under ex-situ conditions, that is, taking samples after annealing steps at different temperatures and characterizing the material subsequently at about 21 °C. Magic angle spinning (MAS) NMR experiments were performed with a 7.04 T magnet spectrometer with Topspin V4.0.5, operating at the frequencies of 121 MHz for ^{31}P, respectively (See SI for more experimental details). The peaks observed in the ^{1}H and ^{13}C MAS NMR spectra of both untreated HOF GTUB5 and the annealed GTUB5-COF (Supplementary Figs. 1–2, Supplementary Information) were successfully assigned to their corresponding environments (Supplementary Fig. 4, Supplementary Table 1–2, Supplementary Information). These results confirm that no decomposition has happened within the organic moieties of GTUB5 after initial annealing to 220 °C. The ^{31}P MAS NMR spectra show that the peaks of the untreated crystalline GTUB5 (starting material) broaden gradually at higher temperatures, and a second peak at 5 ppm steadily emerges as the sample is gradually heated to 220 °C (Fig. 2). In the case of inorganic phosphate salts, condensation to pyrophosphates is recognized to induce a shift in resonances, typically shifting them by approximately 10 ppm to lower values than for monophosphates[31,32]. The characterization of protonated phosphates by the isotropic chemical shift is hampered by the substantial influence of the hydrogen-bonded protons[33,34]. To our knowledge, there is no similar correlation tool for phosphonate ^{31}P shifts. Therefore, we gathered the isotropic chemical shift values for monophosphonates, condensed diphosphonates, and higher condensation products from the literature (Supplementary Table 4, Fig. 2)[31,32]. A similar trend for phosphate groups can also be seen for phosphonate groups. Salts of monophosphonates and hydrogenphosphonate feature a similar isotropic chemical shift range. However, there is a significant overlap between the chemical shift ranges for mono- and condensed-diphosphonate groups. The anisotropic chemical tensor was investigated for differences in the chemical shift anisotropy (Supplementary Table 3, Supplementary Information), but, similar to hydrogen-phosphates, the hydrogen-bonded protons strongly influence the chemical shift tensor, and only insignificant differences were observed.

The magnetic dipole-dipole coupling between neighboring P atoms is a more reliable tool to distinguish condensed diphosphonates from mono-phosphonic acids. The condensation of the R-PO_3H_2 moieties in GUTB5 to form R-P(O)(OH)-O-P(O)(OH)-R (Fig. 1) moieties upon annealing can be tested by measuring the distances between neighboring P atoms using homonuclear ^{31}P double-quantum NMR (Fig. 3). In a P-O-P bridge, as in a condensed-diphosphonate group, the shortest P-P distances can be estimated to be of the order of 300 pm[27,28], while in between monophosphonates, the minimum distance would amount to about 460 pm[35,36]. The dipole-dipole coupling relates to the inverse cubic internuclear distance. Therefore, the P-P distances in two-spin systems can be estimated from the magnetic dipole-dipole coupling, for example, by ^{31}P-^{31}P double-quantum NMR experiments with an error of about 10%, including effects by the anisotropic J-coupling[37]. To this end, a homonuclear ^{31}P-^{31}P double-quantum constant-time (DQCT) experiment was conducted on heated GTUB5, in which the peak at 15 ppm under the chosen conditions

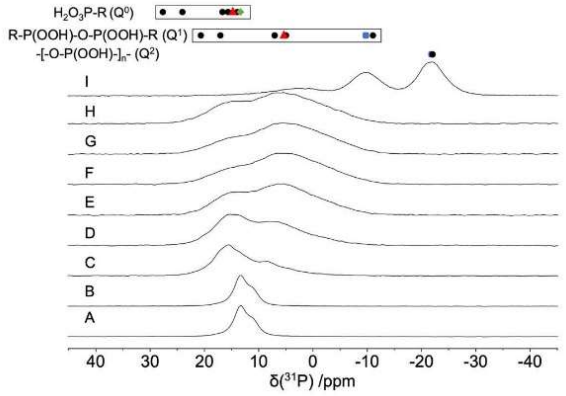

Fig. 2 | A stack plot of ^{31}P MAS NMR spectra of the sample. a GTUB5 and GTUB5 annealed at (**b**) 100 °C, **c** 120 °C, **d** 140 °C, **e** 160 °C, **f** 180 °C, **g** 200 °C, **h** 220 °C and (**i**) 270 °C under vacuum. The measurements were performed with a rotor with 2.5 mm outer diameter spinning at 20 kHz (**a**–**h**) or 14.3 kHz (**i**) under a 7.04 T magnet. The box chart indicates the range of the isotropic ^{31}P NMR chemical shift values of hydrogenmonophosphonates (top, Q^0)[31], that of phosphonates with a single bridging O atom including diphosphonates (middle, Q^1)[32], and of phosphonates with two bridging O atoms (ring/chain) attached to the observed P-atom (bottom, Q^2)[33,34]. The black circles refer to literature values (Supplementary Table 4), the colored symbols refer to the isotropic chemical shift values observed for GTUB5 and GTUB5 annealed at 220 °C and 270 °C.

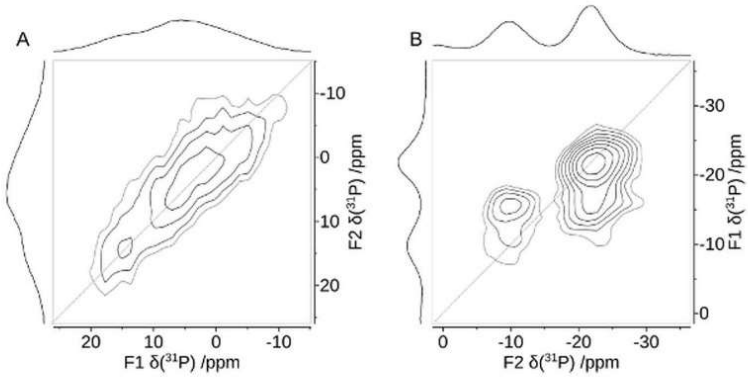

Fig. 3 | ^{31}P MAS NMR double-quantum single-quantum correlation spectra MAS NMR spectra of GTUB5. After annealing at 220 °C (**a**) and after annealing at 270 °C (**b**). The phase-adapted PostC7 pulse sequence[68,69] was used under a magnetic field of 7.04 T at a spinning frequency of ν_r = 14286 Hz (left) and 10 kHz (right), respectively. Double-quantum conversion periods for excitation and reconversion period were 1.4 ms (left) and 0.8 ms (right). The drawn diagonal corresponds to the hypothetical position of the signal of an isochronous spin-pair.

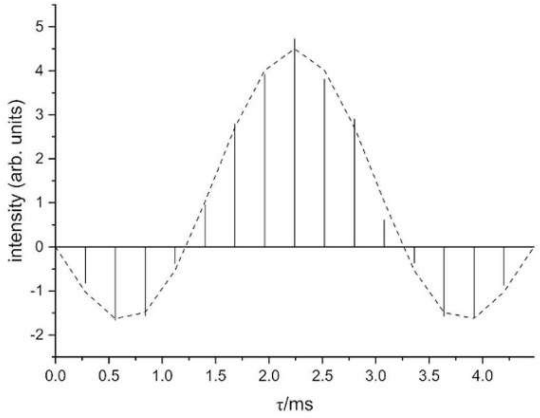

Fig. 4 | ^{31}P MAS NMR double-quantum constant-time build-up curve of the pyrophosphonate peak (peak A, Table 2) of the sample GTUB5 after annealing at 220 °C. The droplines are the experimental data, while the dashed line indicates the fitted data points for a dipole-dipole coupling of -828 Hz. A phase-tuned PostC7 pulse sequence[68,69] was used at a spinning frequency of ν_r = 14286 Hz. The constant-time double-quantum conversion period consists of 224 C-elements[38].

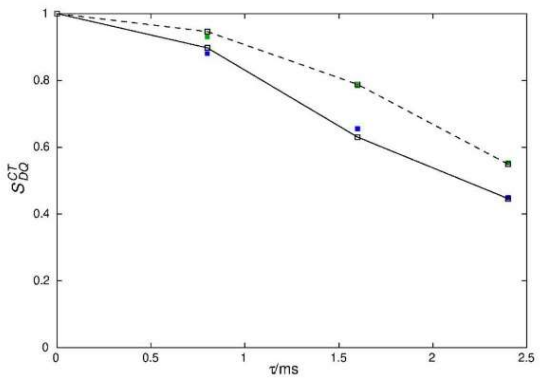

Fig. 5 | ^{31}P MAS NMR double-quantum constant-time dephasing curves of the resonance of the sample GTUB5 after annealing at 270 °C. The experimental double-quantum dephasing ratio S_{DQ}^{CT} for the peaks at −10.1 ppm (filled green squares) and −22.4 ppm (filled blue squares) were fitted by employing numerical simulations of the spin-dynamics with the SIMPSON package[59,60] and yielded effective dipole couplings of ν_{eff} of −673 Hz and −1067 Hz, respectively. The constant-time double-quantum dephasing experiment[39] employed a phase-tuned PostC7 pulse sequence[68,69] for excitation, dephasing, and reconversion at a spinning frequency of ν_r = 10000 Hz. The double-quantum excitation and reconversion period consisted of 56 C-elements, the double-quantum dephasing period consisted of integer multiples of 14 C-elements, that is, a full supercycle.

shows no zero-crossing while the peak at 5 ppm does (Fig. 4, Supplementary Fig. 5, Supplementary Information)[38]. Based on these observations, the two peaks were unambiguously assigned to condensed-diphosphonate and monophosphonate groups, respectively, which means the annealing to 220 °C only led to a partial condensation.

Double-quantum constant-time (DQCT) conversion curves with well-expressed zero-crossings (Supplementary Fig. 5), as in this case, can be analyzed for the magnetic dipole-dipole coupling by fitting the experimental data in a two-spin approximation (Fig. 4), which for the condensed-diphosphonate group is a good approximation because further spins are significantly farther away[38]. The analysis revealed a dipole-dipole coupling of $\nu_{P\text{-}P}$ = −828 Hz for the signal at δ = 5 ppm, corresponding to a P-P distance of $r_{P\text{-}P}$ = 2.9 Å within the condensed-diphosphonate group. The bond length includes a small uncertainty of around 10% for the effective coupling constant caused by the anisotropic $^2J(^{31}P,^{31}P)$-coupling, translating into an error of about 0.1 Å[37]. It can be concluded that the presence of a condensed-diphosphonate group can be unambiguously evidenced by solid-state NMR.

From the higher temperature annealing experiments, a GTUB5 sample that was annealed at 270 °C and activated under vacuum for adsorption studies was singled out for further characterization by solid-state NMR, because of the promising mass loss observed in DTA/TG experiments (vide infra). In principle, phosphonate groups could further be condensed forming chain or ring-phosphonates. Regarding the Q^n nomenclature introduced for silicate and phosphate groups, where n corresponds to the number of bridging O atoms attached to a P atom, phosphonates can form Q^0, Q^1, and Q^2 groups but not Q^3 groups, which phosphates can do. The tendency to show smaller isotropic chemical shift values the higher the number of bridging O-atoms n, is also followed for the GTUB5 compound annealed at 270 °C[22]. Two new resonances are observed at lower shift values (Fig. 2). To prove that the condensation at higher temperatures yields polyphosphonates, again, double-quantum ^{31}P NMR can be used. Qualitatively, the 2D double-quantum (DQ) single-quantum correlation NMR spectra of GTUB5 annealed at 220 °C and 270 °C show the expected DQ correlation peaks of a condensed-diphosphonate (Fig. 3) and that of a chain phosphonate (Fig. 3) where the peak at −10 ppm is assigned to terminal phosphonate groups (Q^1) and the peak at −22 ppm is assigned to chain or ring-phosphonate groups (Q^2), respectively. The peak area ratio between the peaks of these two groups of 0.61 indicates an average chain length of 5.3, assuming a chain structure. The assignment via the chemical shift and the occurrence of double-quantum correlation signals can be validated by measuring the effective dipole coupling of the individual ^{31}P atoms[39]. The effective dipole coupling constant is calculated from the square root of the sum of the squared dipole couplings of an observed nucleus. Because of two bridging P-O-P linkages for Q^2 instead of one for Q^1, the effective dipole coupling for Q^2 can be expected to be 41% larger than that of a Q^1 P-atom. The effective dipole couplings were measured with the help of a constant-time double-quantum dephasing experiment (Fig. 5) and indeed amount to −673 Hz for the Q^1 peak and −1067 Hz for the Q^2 peak[39]. This can be considered an unambiguous confirmation of the above peak assignment and proof of polyphosphonates forming at higher annealing temperatures. The peaks of different Q^n groups observed for GTUB5 annealed at different temperatures were added to the box plot of typical isotropic chemical shift values for further reference (Fig. 2).

Characterization of polyphosphonate units via FT-IR

The condensation of HOF GTUB5 to GTUB5-COF at higher temperatures was monitored with temperature variable FT-IR spectroscopy. First, the sample was heated to 50 °C, and a spectrum was recorded. Then, the sample was evacuated at 50 °C overnight. This resulted in increased transmittance at 3400 cm^{-1} and 1635 cm^{-1}, indicating a loss of water, either structural water incorporated in the HOF or contamination in the KBr used to prepare the pellet (Supplementary Fig. 6).

Then, the sample was maintained in a vacuum as the temperature was increased (Fig. 6a). As the sample was heated, increased transmittance was observed at 2700 cm^{-1}, 2450 cm^{-1}, 1710 cm^{-1}, and 1050 cm^{-1} and assigned to the loss of phosphonic acid groups[40–44]. Decreased transmittance at 970 cm^{-1} was assigned to forming P-O-P linkages[45]. The P-O-H deformation mode in a phosphonic acid is also expected to absorb at around 960 cm^{-1}[41,43]. Difference spectra (Fig. 6b)

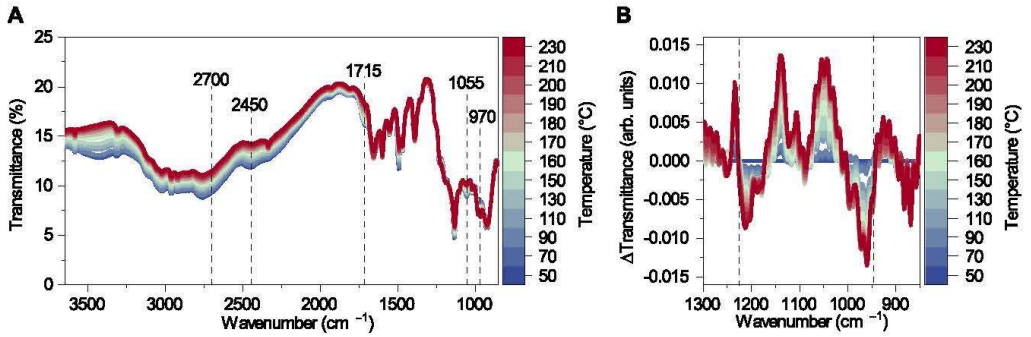

Fig. 6 | Temperature variable FT-IR. a FT-IR spectra of HOF GTUB5 during the heating up to 230 °C. **b** FT-IR difference spectra of GTUB5 during the heating.

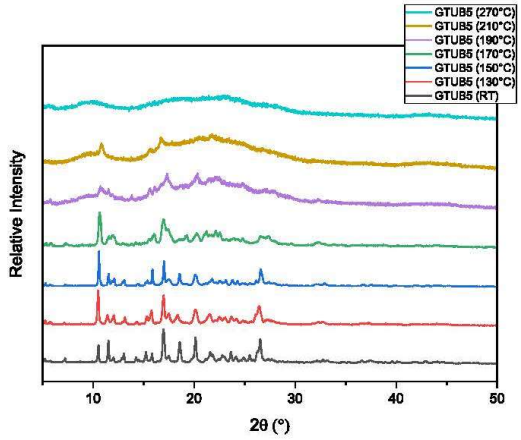

Fig. 7 | Temperature variable powder X-ray measurements. Powder X-ray diffractograms were measured from 5° to 50° 2θ for GTUB5-COF at room temperature (20 °C) and heated for 2 h each time at 130 °C, 150 °C, 170 °C, 190 °C, 210 °C, and 270 °C. This figure can be used with Fig. 2. to compare the crystallinity at each temperature-dependent COF phase.

show a bipolar band at this frequency range, supplementary the conclusion that phosphonic acid groups are condensing to form P-O-P linkages. Similarly, difference spectra show a bipolar band around 1230 cm^{-1} where the P = O bond in both phosphonic acid and condensed-diphosphonate absorbs, and the condensation or the phosphonic acid groups results in a subtle change in the vibrational frequency of the P = O bond (P = O bond is also represented as $^{+}$P-O^{-}, as it is not a classical double bond with π-contribution)[40–45].

DFT calculations

To confirm the proposed synthesis route, the idealized structure in Fig. 1 was geometry optimized with density functional theory (DFT), as shown in Fig. 1 (bottom). The atom-to-atom distance between hydrogens on the opposing porphyrins in the same pore is about 8.5 Å. To elaborate further on the pore opening of GTUB-COF up on stacking, we placed three geometry-optimized idealized structures on top of each other. We ran a 5 ps ab initio molecular dynamics (AIMD) simulation using the same DFT formalism at room temperature. We observed a gradual constriction of the pore opening, yielding a 5.3 Å atom-to-atom distance at its narrowest section (Fig. 1 and methods section for experimental details).

Thermal and chemical stability

Although there are several stable COFs in the literature, searching for stable COFs in the presence of water and water vapor and their thermal stability is an ongoing research area[46]. The thermal stability of GTUB5-COF was investigated by initial heating of a sample starting at room temperature up to 270 °C and comparing the powder X-ray diffractograms measured at ambient temperature (Fig. 7). While the crystallinity gradually decreases up to 210 °C, a very similar amorphous diffraction pattern above 210 °C until 270 °C has been observed. We obtained the original unit cell via single crystal X-ray diffraction up to 130 °C, suggesting that the GTUB5 HOF is thermally stable at 130 °C. Although the PXRD data of the original HOF structure pattern is mostly retained up to 190 °C, the single crystal diffraction experiments did not provide a unit cell for the samples heated above 130 °C; due to the gradually decreased crystallinity no further single crystal diffraction measurements could be followed up. As the heated sample at 270 °C retained its crystalline shape and color, we tried 3D electron diffraction to identify the structure of the resulting HOF. Still, getting a data set suitable for structural characterization was impossible. The heated crystals of GTUB5-COF break up in muscle pattern, which is generally seen in glass materials. Figure 7 displays the powder X-ray diffractograms measured at ambient temperature (20 °C), at 130 °C, at 150 °C, at 170 °C, at 190 °C, at 210 °C, and 270 °C from 5° 2θ to 50° 2θ in comparison to each other and the NMR data from Fig. 2. Each time, the same sample was heated for 2 h at the respective temperature.

The heated sample of GTUB5-COF was then added to cold water and boiling water for one hour to test its chemical stability. Due to its amorphous structure, it was impossible to confirm whether GTUB5-COF retained its original structure using PXRD. The crystal shape and color stayed stable in the cold and boiled water after 1 h and did not dissolve or dissipate. The overall structure might have experienced phase transfers due to the presence of flexible P-O-P bonds; we could not confirm this due to the amorphous nature of the GTUB5-COF (Supplementary Fig. 7, Supplementary Information). Furthermore, as larger P-O-P oligomers formed at higher temperatures, the presence of DMA molecules in the pores might have reduced the crystallinity of the resulting COFs. Supplementary Fig. 7 displays the powder X-ray diffractograms of the sample measured after 210 °C heating, after 1 h in cold water, and the activated sample at 270 °C. Although amorphous at this point, a characteristic diffraction pattern can still be identified, thus suggesting the presence of an intact sample.

Furthermore, the constant reproducibility of the water adsorption isotherms for one month also suggests the stability of the reported GTUB5-COF in the presence of water vapor. The water-treated GTUB5-COF at 210 °C and activated GTUB5-COF at 270 °C have two similar broad peaks in their X-ray diffractogram. The disappearance of relatively sharper peaks at the water-treated sample at 210 °C might be due

to the potential release of DMA molecules in the pores, which are miscible with water, increasing the amorphous nature of GTUB5-COF after water treatment. Furthermore, MAS-NMR experiments also proved the presence of linkers at 220 °C.

X-ray photoelectron spectroscopy (XPS)

XPS measurements were conducted to determine the oxidation state and bonding environment of the nonmetal ions (P, O, N, C) in the heated sample of GTUB5 to 270 °C. The XPS survey spectrum of GTUB5 confirmed the presence of all the elements (C, N, O, and P) of the synthesized material. The survey spectra are shown in Supplementary Fig. 8, and the high-resolution spectra are in Supplementary Fig. 9. The high-resolution carbon 1 s spectrum (C *1 s*) can be fitted into 3 peaks with binding energies of 284.5 eV, 284.8 eV, and 286 eV, which indicate the presence of (C = C), (C-C), and (C-N) bonds suggesting the presence of aromatic groups and the porphyrin core. The position of each peak is assigned in Supplementary Table 5. The oxygen spectrum (O *1 s*) can be deconvoluted into two peaks positioned at 531 eV and 532.7 eV, which are related to the bridging oxygen (P-O-P) and the non-bridging oxygen (P-O). The positions of these peaks are provided in Supplementary Table 6. The nitrogen *1 s* spectrum (N 1 s) consists of three peaks with a binding energy of 400.0 eV, 397.9 eV, and 402.4 eV, which correspond to the presence of (C = N) and (C-N) bonds. The binding energy peaks of N *1 s* are listed in Supplementary Table 7. The third peak indicates that traces of the solvent DMA can still be detected, which is also confirmed by TGA-MS. The high-resolution spectrum of phosphorus 2p (P *2p*) showed two characteristic peaks at 133.5 eV and 134.9 eV, which were ascribed to (P-C) and (P-O) bonds. The binding energy peaks of P *2p* are listed in Supplementary Table 8.

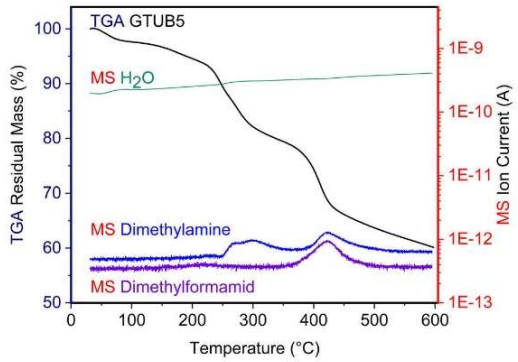

Fig. 8 | Thermogravimetric analysis. Mass spectrometry coupled thermogravimetric analysis (H_2O, dimethylamine, and dimethylformamide) were measured between 30 °C to 600 °C under a nitrogen atmosphere at a 10 K/min heating rate for GTUB5.

MS-TGA

We coupled thermogravimetric analysis with mass spectrometry to better understand the underlying reaction mechanism. As seen in Fig. 8, the TGA measurement was performed between 30 °C and 600 °C. The green curve displays the number of H_2O ions detected by mass spectrometry, the dark blue line shows the amount of detected dimethylamine, and the light blue line represents the detected DMF. The first step of the TGA curve can be observed at 50 °C, likely due to the loss of the solvent or guest molecules. A second step is noticeable at 230 °C, which is connected to the detection of dimethylamine by mass spectrometry. This affirms the hypothesis that a condensation reaction involving deprotonating the dimethylamine cations and the phosphonic acid groups of GTUB5 occurred. Starting at 390 °C, the third step is connected to detecting dimethylamine and DMF by mass spectrometry. At 390 °C, the complete decomposition of the porphyrin core begins. The formation of DMA and DMF at 390 °C may be explained as pyrolysis products observed after the decomposition of the porphyrin residue.

Electrochemical stability

The reactivity and stability of the GTUB5-COF sample, which was annealed at 270 °C, were investigated in a three-electrode cell setup with a platinum wire and Ag/AgCl (3 M) as counter and reference electrodes, respectively. The open circuit potential (OCP) was measured in an aqueous 0.5 M Na_2SO_4 electrolyte for 1 h to evaluate the thermodynamic behavior of the material, followed by linear sweep voltammetry (LSV) in a potential window from −1 V to 2 V vs. Ag/AgCl (3 M) with a scan rate of 1 mV s^{-1} to assess the electrochemical stability window. To perform the experiments, 50 µL of a 0.5 mg mL^{-1} aqueous GTUB5-COF dispersion was drop-casted on a glassy carbon electrode (GCE) with a 7 mm^2 surface area and dried at room temperature. The OCP measurement illustrated in Fig. 9a suggests stability of the GTUB5-COF material in an aqueous neutral environment, exhibiting a noble and stable E_{OCP} = +0.425 V vs. Ag/AgCl, highlighting long-term stability of the material in aqueous electrolytes[47]. The GTUB5-COF was further investigated through LSV, as shown in Fig. 9b. The material exhibited an electrochemical stability window ranging from -0.6 V to +1.3 V vs. Ag/AgCl followed by an oxidation of the aqueous media[48].

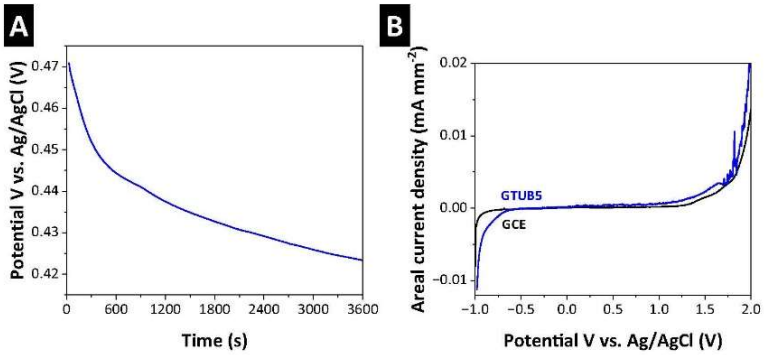

Fig. 9 | Electrochemical stability of the activated GTUB5-COF sample. a Open circuit potential (OCP) measurement for 1 h and **b** linear sweep voltammogram recorded at 1 mV s^{-1} in aqueous 0.5 M Na_2SO_4 electrolyte.

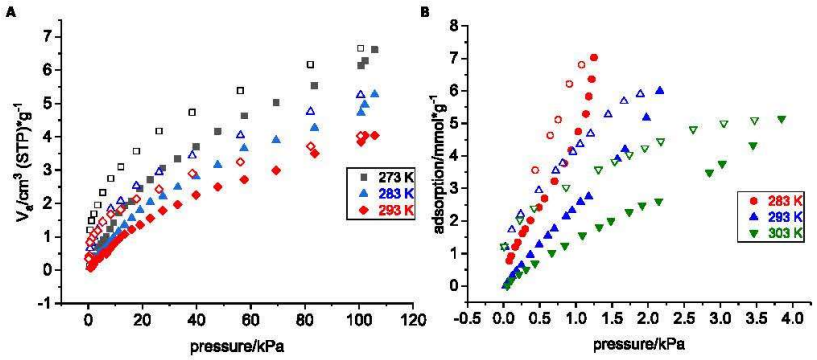

Fig. 10 | Gas and vapor sorption. a CO_2 sorption at different temperatures (filled symbols adsorption, empty symbols desorption) **b** water sorption isotherms at 283 K, 293 K, and 303 K (filled symbols adsorption, empty symbols desorption).

Such behavior suggests potential application in electrochemical systems such as catalysis, combining a layered compact material, as shown in Supplementary information Supplementary Fig. 10A–F and Supplementary Fig. 11, with favorable electrochemical stability.

Gas sorption

While COFs have shown potential to capture CO_2, there are only a very small number of COFs and MOFs that can capture CO_2 in the presence of water vapor, according to a recent comprehensive review article published by Zhao et al.[46,49–51]. To gain more insight into the material and estimate the activation temperature, we performed TGA-MS experiments. According to TGA-MS data, DMA molecules started to leave the pores at ca. 230 °C. Therefore, large needles of GTUB5-COF with sizes between 1 mm and 3 mm (not ground) were activated by heating to 270 °C under vacuum for 2 h to ensure that most of the DMA molecules were evaporated to empty the pores of GTUB5-COF. The activated GTUB5-COF at 270 °C and water-treated GTUB5-COF have an X-ray diffraction pattern aligning with an amorphous material (Supplementary Fig. 7, Supplementary Information). Each CO_2 and N_2 sorption measurement was repeated three times, and in between each measurement, GTUB5-COF was heated to 60 °C to clear pores from the remaining residual CO_2 and N_2 gases. Water sorption measurements were performed using a Quantachrome V-STAR4. Between each water sorption measurement, GTUB5-COF was heated to 200 °C for 2 h to remove the residual water from GTUB5-COF's pores. Each of the repeated gas sorption and water sorption measurements provided similar reproducible adsorption isotherms.

Nitrogen sorption measurements at 77 K revealed negligible N_2 adsorption capacity and low surface area for GTUB5-COF, which is below 1 m^2/g according to BET calculations. In contrast, GTUB5-COF (needles between ca. 1 mm and 3 mm) exhibits notable CO_2 and water vapor uptake at room temperature compared to the N_2 sorption studies. As we used 1–3 mm long needle-shaped GTUB5-COF sample in the measurements, the error that might originate from fine powder surface area is estimated to be minimal. As seen in Fig. 10a, isotherms at 273 K, 283 K, and 293 K were measured for CO_2 adsorption. Much higher CO_2 adsorption compared to nitrogen was observed. The distinct adsorption behavior at different temperatures suggests the dynamic nature of GTUB5-COF's porous structure and potential phase transfers due to flexible P-O-P bonds in GTUB5-COF. It is kinetically difficult for N_2 to access the pores GTUB5-COF at 77 K. Nevertheless, GTUB5-COF demonstrates that its pores are suitable for CO_2 compared to N_2. Similar to the N_2 adsorption experiments, CH_4 also did not show any adsorption, which can be explained by the larger kinetic radius of N_2 and CH_4 compared to CO_2 and water vapor.

The CO_2 adsorption isotherms showed a distinct hysteresis over the whole pressure range, indicating favorable interaction between adsorbent and adsorbate. The observed hysteresis in Fig. 10b closely resembles the characteristic features of type H4, as shown by Sing in 2015[52,53]. This observation suggests the presence of small and narrow pores with a polar surface. Following the observed hysteresis, the BET calculation derived from the adsorption isotherm at 273 K gave a CO_2-accessible surface area of 47 m^2/g and a total pore volume of 0.014 cm^3/g. We calculated the enthalpy of adsorption for CO_2 by measuring the CO_2 adsorption at three different temperatures at 273 K, 283 K, and 293 K via fitting the adsorption isotherms by Langmuir-Freundlich model (Supplementary Fig. 12) and using the Clausius-Clapeyron equation[54]. The enthalpy of adsorption ΔH of CO_2 was calculated to be −27 kJ/mol at a CO_2 loading of 0.01 mmol/g. This value is relatively constant over the observed pressure range.

$$\Delta H(n) = -R \cdot ln(p_2/p_1)(T_1 \cdot T_2/(T_2 - T_1)) \quad (1)$$

As seen in Fig. 10 (right), water vapor sorption measurements at 283 K, 293 K, and 303 K showed an adsorption pattern with a slight convex curvature, exhibiting a type II isotherm[52]. This observation also confirms the presence of limited porosity and polar pore surfaces. The enthalpy of water adsorption was also calculated using the same method, giving a value of −21 kJ/mol for a loading of 0.2 mmol/g at a pressure of 10^{-4} bar. The load of 0.2 mmol/g was used due to lower accuracy within the low-pressure region for water sorption and according to the available measure points (Supplementary Fig. 12). Unlike CO_2, the enthalpy of adsorption for water vapor becomes more negative with increased pressure. The formation of the hydrogen bonds between adsorbed water molecules probably caused the more favorable change in the enthalpy of adsorption for water. Both CO_2 gas and water vapor show favorable interaction with the pore surface of GTUB5-COF. Comparability to the enthalpy of carbon dioxide adsorption is complicated due to the distinct characteristics inherent to CO_2 gas and water vapor. Nevertheless, the more negative -27 kJ/mol enthalpy of adsorption value for CO_2 sorption at lower pressure suggests the potential of GTUB-COF for selective CO_2 capture. Furthermore, the repeated consistency of water adsorption isotherms also proves the stability of GTUB5-COF in water vapor. Flue gas contains water vapor, N_2, CO_2, and O_2. To our knowledge, no other works exist that compare the enthalpy of adsorption for CO_2 gas and water vapor. Most of the CO_2 adsorption with COFs was performed for CO_2 against N_2. A list of COFs that are stable in water or water vapor with favorable enthalpy of adsorption for CO_2 can be seen in Supplementary Table 9.

Supplementary Fig. 13 depicts the diffuse reflectance and luminescence spectra of GTUB5-COF derived from its diffuse reflectance. The localized transitions of the porphyrin entities within the COF characterize it. It reveals the characteristic Soret band at around 350 nm and the Q bands between 430 nm and 700 nm. This suggests the presence of an intact porphyrin core in heated GTUB5-COF, which was activated at 270 °C. The compound shows weak broad-banded fluorescence of the porphyrin units in the near-infrared range, peaking at around 800 nm.

Herein, we report polyphosphonate-COFs. This report presents a straightforward and environmentally friendly method to condense phosphonic acid HOF crystals to synthesize polyphosphonate-COFs in a single step, accomplished by heating the precursor phosphonic acid HOF crystals without additional chemical reagents. Upon gradual heating of the HOF precursor, we initially observed partial condensation of phosphonic acids to generate phosphonic acid anhydride linkages at 220 °C, and after annealing it to 270 °C, we observed the further condensation of phosphonic acids to polyphosphonate chains (or polymeric phosphonic acid anhydride) and rings. We used PXRD, MAS-NMR, FT-IR, XPS, and TGA-MS experiments to monitor the formation of the condensed phosphonate bonds in GTUB5-COF. PXRD data suggests the presence of crystallinity until 210 °C, but crystallinity disappears gradually as the degree of polymerization increases to generate amorphous phases at higher temperatures. The heated sample of GTUB5 retains crystalline COF characteristics until 210 °C. It becomes an amorphous porous polymer with a higher degree of P-O-P bonds at higher temperatures. Based on the MS-TGA data, the $HDMA^+$ cations in GTUB5 donate their protons to the phosphonate groups to promote the condensation of phosphonic acid groups. After the condensation of GTUB5 to form GTUB5-COF, the neutral DMA molecules gradually leave the GTUB5-COF structure at ca. 230 °C, generating void spaces suitable for small molecule capture. GTUB5-COF provides a very dynamic tunable platform leading to a gradually increased degree of P-O-P bond oligomerization at increasing temperatures. The enthalpy of adsorption indicates that GTUB5-COF exhibits higher selectivity for CO_2 molecules than water vapor at lower pressures. In contrast, it becomes more selective for water vapor at higher pressures. The reported GTUB5-COF exhibits stability in water and water vapor during the BET measurements, and it is not visually dissolved in cold and boiling water (the dissolved 5,10,15,20-tetrakis[p-phenylphosphonic acid]porphyrin linker produces a very dark red solution).

Furthermore, we have shown that GTUB5-COF is electrochemically stable in 0.5 M Na_2SO_4 electrolyte in water, and MAS-NMR data have shown that the linker cores of GTUB5-COF did not chemically decompose at 270 °C. Furthermore, after repeated gas sorption, XPS data have also shown the presence of intact organic linkers and P-O-P bonds. While COF research has yielded diverse families and applications across various fields, a significant and desirable advancement in COF chemistry is the creation of water-stable and CO_2-selective COFs. The presented polyphosphonate-COF GTUB5-COF in this work may provide the required stability in water, boiling water, and neutral electrolytes. Both MOFs and COFs are composed of hydrophilic linkages, resulting in a competition between CO_2 and water vapor, which mostly favors water adsorption. The small pores exemplify how to utilize the kinetic radii of gases to enhance selectivity for CO_2 in the COF research field, and it can address the diverse problems and find industrial use. These findings show GTUB5-COF's potential in controlled gas adsorption and selective CO_2 capture, promising directions in sustainable gas storage and separation. Due to the easy synthesis, GTUB5-COF can be easily synthesized on an industrial scale to address a variety of applications. We are currently exploring the full potential of polyphosphonate-COFs, determining their long-term stability in different media, COF thin films, and using longer tethered arylphosphonic acids to improve the surface areas of polyphosphonate-COFs.

Methods

Synthesis of GTUB5-COF

Phenyl phosphonic acid and the starting materials for the synthesis of 5,10,15,20-tetrakis[p-phenylphosphonic acid]porphyrin have been purchased commercially from Alfa Aesar and Merck and used without further purification. 5,10,15,20-tetrakis[p-phenylphosphonic acid]porphyrin and HOF GTUB5 were prepared using our previously reported methodology[16]. The condensation of HOF crystals of GTUB5 was performed in oven between 130 and 270 °C.

Magic Angle Spinning (MAS) NMR

To study the samples GTUB5 heated up to 270 °C, magic angle spinning (MAS) NMR experiments were performed with a 7.04 T magnet spectrometer with Topspin V2.1, operating at the frequencies of 121 MHz for ^{31}P, respectively. Magic angle sample spinning was done with a commercial 2.5 mm MAS probe head and a self-made 3.5 mm MAS probe head[55]. The chemical shift values refer to the IUPAC reference compound[56]. MAS NMR experiments were also performed with Avance Neo with a 14.1 T magnet spectrometer with Topspin V4.0.5, operating at the frequencies of 242 MHz for ^{31}P, respectively. Magic angle sample spinning was done with a commercial 1.3 mm MAS probe head. Tetramethyl silane and phosphoric acid were used to reference the shift scale of ^1H and ^{31}P NMR, which have the same Ξ values published by IUPAC[56]. The software packages deconv2Dxy-0.4[57] and Simpson-4.2.1[58,59] were used to analyze and fit the NMR spectra. The following equations define the anisotropic chemical shift δ_{aniso} and the asymmetry parameter η:

$$\delta_{aniso} = \delta_{zz} - \delta_{iso} \quad (2)$$

$$\eta = (\delta_{yy} - \delta_{xx})/\delta_{aniso} \quad (3)$$

XPS

X-ray photoelectron spectroscopy (XPS) was performed with an ULVAC-PHI VersaProbe II microfocus X-ray photoelectron spectrometer. The spectra were recorded using polychromatic aluminum Kα X-ray source (1486.8 eV) and referenced to the carbon 1 s orbital with a binding energy of 284.4 eV. Fitting of the experimental XP spectra was done with the Program CasaXPS, version 2.3.19PR1.0, copyright 1999---2018 Casa Software Ltd.

DFT calculations

Geometry optimization and AIMD simulation of GTUB-COF were carried out using the CP2K[60] simulation package and employed periodic density functional theory (DFT) calculations within the generalized gradient approximation using the revised Perdew–Burke–Ernzerhof (revPBE-D3) functional and Grimme's D3 dispersion corrections to calculate the energies and the forces[61–63]. The core electrons were treated using the Goedecker-Tetter-Hutter (GTH) pseudo-potentials[64–66], and the valence electrons were expanded using the Gaussian and Plane-Wave (GPW) combined basis sets (double-zeta DZVP along with a plane wave basis set with 400 Ry cut-off energy) as implemented in CP2K/quickstep (version 8.2). The AIMD simulation was run for 5 ps within the Born-Oppenheimer approximation with a time step of 0.5 fs. The temperature was fixed using the Canonical Sampling through Velocity Rescaling (CSVR) thermostat with a time constant of 100 fs[67].

Transmission electron microscopy

The Tecnai G2 F20 was used to obtain transmission electron micrographs of GTUB5-COF heated to 270 °C.

FT-IR

FT-IR spectra were recorded with a Bruker 70 v spectrometer (Bruker). For the measurements, 1.6 mg of the HOF powder was mixed with

200 mg KBr and pressed into a pellet with the Atlas Power 15 t hydraulic press (Specac). The pellet was mounted in a vacuum-jacketed variable temperature cell holder (Specac) with pressure <1 mbar. The FT-IR spectra were measured in the transmission mode in the temperature range 50–230 °C.

Powder X-ray diffraction

Powder X-ray diffraction (PXRD) was performed on a Rigaku Miniflex powder diffractometer in θ/2θ geometry with Cu-Kα radiation (1.54184 Å).

Optical spectroscopy

Diffuse reflectance and emission spectra were measured on an Edinburgh FLS1000 luminescence spectrometer with 450 W Xe arc lamp, double grating monochromators (Czerny-Turner configuration, blazed at 400 nm in excitation and 500 nm in emission) and a thermoelectrically cooled (−20 °C) PMT980 (Hamamatsu) photomultiplier tube as detection unit. All spectra were acquired at room temperature. Diffuse reflectance was measured using an integrating sphere (diameter 120 mm) setup with the inner surface coated with BenFlect (reflectance >99 % between 350 nm and 2500 nm). All spectra were corrected for the grating efficiency, the lamp intensity, and the wavelength-dispersive sensitivity of the detection unit.

Gas sorption

Gas sorption measurements were done on the BELSorp-max II by MicrotracBEL Corporation.

Scanning electron microscopy

A ZEISS GEMINI 500 scanning electron microscope (SEM) was used to obtain the GTUB5 micrographs by applying an accelerating voltage of 1 kV at a working distance of 4.8 mm. Before the measurements, the samples were mounted on an aluminum stub fixed with copper tape.

Energy dispersive X-ray spectroscopy

A SEM (ZEISS GEMINI 500) coupled with an Xmax detector from Oxford instrument employing an acceleration voltage of 1 kV for imaging and 10 kV for energy dispersive X-ray (EDX) spectroscopy analysis was used for the GTUB5 mapping and the elemental analysis.

Data availability

Details of synthesis, NMR data, FT-IR data, DFT calculations, XPS data, scanning electron micrographs, transmission electron micrographs, and details of gas sorption studies. All data can be obtained from the corresponding authors upon request. NMR data is accessible at https://fodasi.e-science-service.uni-siegen.de/handle/fodasi/48.

References

1. El-Kaderi, H. M. et al. Designed synthesis of 3D covalent organic frameworks. *Science* **316**, 268 (2007).
2. Côté, A. P. et al. Porous, crystalline, covalent organic frameworks. *Science* **310**, 1166 (2005).
3. Lin, R.-B. et al. Multifunctional porous hydrogen-bonded organic framework materials. *Chem. Soc. Rev.* **48**, 1362–1389 (2019).
4. Qian, C. et al. Toward covalent organic frameworks bearing three different kinds of pores: the strategy for construction and COF-to-COF transformation via heterogeneous linker exchange. *J. Am. Chem. Soc.* **139**, 6736 (2017).
5. Geng, K. et al. Covalent organic frameworks: design, synthesis, and functions. *Chem. Rev.* **120**, 8814–8933 (2020).
6. Lohse, M. S. & Bein, T. Covalent organic frameworks: structures, synthesis, and applications. *Adv. Funct. Mater.* **28**, 1705553 (2018).
7. Segura, J. L., Mancheno, M. J. & Zamora, F. Covalent organic frameworks based on schiff-base chemistry: synthesis, properties and potential applications. *Chem. Soc. Rev.* **45**, 5635 (2016).
8. Han, X.-H. et al. Syntheses of covalent organic frameworks via a one-pot suzuki coupling and schiff's base reaction for C_2H_4/C_3H_6 separation. *Angew. Chem. Int. Ed.* **61**, e202202912 (2022).
9. Abuzeid, H. R., El-Mahdy, A. F. M. & Kuo, S.-W. Covalent organic frameworks: design principles, synthetic strategies, and diverse applications. *Giant* **6**, 100054 (2021).
10. Han, S. S., Furukawa, H., Yaghi, O. M. & Goddard, W. A. Covalent organic frameworks as exceptional hydrogen storage materials. *J. Am. Chem. Soc.* **130**, 11580 (2008).
11. Doonan, C. J., Tranchemontagne, D. J., Glover, T. G., Hunt, J. R. & Yaghi, O. M. Exceptional ammonia uptake by a covalent organic framework. *Nat. Chem.* **2**, 235 (2010).
12. Furukawa, H. & Yaghi, O. M. Storage of hydrogen, methane, and carbon dioxide in highly porous covalent organic frameworks for clean energy applications. *J. Am. Chem. Soc.* **131**, 8875 (2009).
13. Cai, S. L. et al. Tunable electrical conductivity in oriented thin films of tetrathiafulvalene-based covalent organic framework. *Chem. Sci.* **5**, 4693 (2014).
14. Klontzas, E., Tylianakis, E. & Froudakis, G. E. Designing 3D COFs with enhanced hydrogen storage capacity. *Nano Lett.* **10**, 452 (2010).
15. Liu, S. et al. All-organic covalent organic framework/polyaniline composites as stable electrode for high-performance supercapacitors. *Mater. Lett.* **236**, 354 (2019).
16. Tholen, P. et al. Semiconductive microporous hydrogen-bonded organophosphonic acid frameworks. *Nat. Commun.* **11**, 3180 (2020).
17. Tholen, P. et al. Tuning structural and optical properties of porphyrin-based hydrogen-bonded organic frameworks by metal insertion. *Small* **18**, 2204578 (2022).
18. Jeffrey, G. A. *An introduction to hydrogen bonding*. (Oxford University Press, 1997).
19. Sun, Y. et al. Bio-inspired synthetic hydrogen-bonded organic frameworks for efficient proton conduction. *Adv. Mater.* **35**, 2208625 (2023).
20. Harsági, N. & Keglevich, G. The hydrolysis of phosphinates and phosphonates: a review. *Molecules* **26**, 2840 (2021).
21. Dürr-Mayer, T. et al. The chemistry of branched condensed phosphates. *Nat. Commun.* **12**, 5368 (2021).
22. Jessen, H. J., Dürr-Mayer, T., Haas, T. M., Ripp, A. & Cummins, C. C. Lost in condensation: poly-, cyclo-, and ultraphosphates. *Acc. Chem. Res.* **54**, 4036–4050 (2021).
23. Schütrumpf, A. et al. Tetrahedral tetraphosphonic acids. new building blocks in supramolecular chemistry. *Cryst. Growth Des.* **15**, 4925–4931 (2015).
24. Heggen, B., Roy, S. & Müller-Plathe, F. Ab initio calculations of the condensation of phosphonic acid and methylphosphonic acid: chemical properties of potential electrolyte materials for fuel cell applications. *J. Phys. Chem. C.* **112**, 14209–14215 (2008).
25. Zhang, C. et al. Low-Temperature Thermal Formation of the Cyclic Methylphosphonic Acid Trimer [c-(CH3PO2)3.*Chem. Phys. Chem.* **24**, e202200660 (2023).
26. Yucesan, G., Ouellette, W., Golub, V., O'Connor, C. J. & Zubieta, J. Solid state coordination chemistry: temperature dependence of the crystal chemistry of the oxovanadium-phenylphosphonate-copper(II)-2,2′-bipyridine system. Crystal structures of the one-dimensional [{Cu(bpy)}$VO_2(O_3PC_6H_5)(HO_3PC_6H_5)$], [{$Cu_3(bpy)_3$($H_2O$)}$V_4O_9(O_3PC_6H_5)_4$], [{Cu(bpy)}$_2V_3O_6(O_3PC_6H_5)_3(HO_3PC_6H_5)$] and [{Cu(bpy)}$VO(O_3PC_6H_5)$2.*Solid State Sciences* **7**, 445–458 (2005).
27. Guo, L.-R., Bao, S.-S., Li, Y.-Z. & Zheng, L.-M. Ag(i)-mediated formation of pyrophosphonate coupled with C–C bond cleavage of acetonitrile. *Chemical Communications*, 2893–2895 (2009).
28. Guo, L.-R. et al. Silver(i) pyrophosphonates: structural, photoluminescent and thermal expansion studies. *Dalton Trans.* **40**, 6392–6400 (2011).

29. Arz, M. I., Annibale, V. T., Kelly, N. L., Hanna, J. V. & Manners, I. Ring-opening polymerization of cyclic phosphonates: access to inorganic polymers with a PV–O main chain. *J. Am. Chem. Soc.* **141**, 2894–2899 (2019).
30. Dürr-Mayer, T. et al. Non-hydrolysable analogues of cyclic and branched condensed phosphates: chemistry and chemical proteomics. *Chem. A Eur. J.* **29**, e202302400 (2023).
31. Schülke, U., Kayser, R. & Neumann, P. Zur Darstellung von Cyclophosphaten, Cyclophosphatophosphonaten, Diphosphonaten und Diphosphiten in Harnstoffschmelzen. *Z. Anorg. Allg. Chem.* **576**, 272–280 (1989).
32. Ohms, G., Großmann, G., Schwab, B. & Schiefer, Synthesis and ^{31}P and ^{13}C NMR studies of pyrophosphonic acids. *Phosphorus, Sulfur, Silicon Relat. Elem.* **68**, 77–89 (1992).
33. Hartmann, P., Vogel, J. & Schnabel, B. The Influence of Short-Range Geometry on the ^{31}P chemical-shift tensor in protonated phosphates. *J. Magn. Reson., Ser. A* **111**, 110–114 (1994).
34. Iuga, A., Ader, C., Gröger, C. & Brunner, E. in *Annual Reports on NMR Spectroscopy* Vol. 60 (ed G. A. Webb) 145–189 (Academic Press, 2006).
35. Demadis, K. D., Katarachia, S. D. & Koutmos, M. Crystal growth and characterization of zinc–(amino-tris-(methylenephosphonate)) organic–inorganic hybrid networks and their inhibiting effect on metallic corrosion. *Inorg. Chem. Commun.* **8**, 254–258 (2005).
36. Demadis, K. D., Katarachia, S. D., Raptis, R. G., Zhao, H. & Baran, P. Alkaline earth metal organotriphosphonates: inorganic–organic polymeric hybrids from dication–dianion association. *Cryst. Growth Des.* **6**, 836–838 (2006).
37. Burck, S. et al. Diphosphines with strongly polarized P–P bonds: hybrids between covalent molecules and donor–acceptor adducts with flexible molecular structures. *J. Am. Chem. Soc.* **131**, 10763–10774 (2009).
38. Schmedt auf der Günne, J. Distance measurements in spin-1/2 systems by ^{13}C and ^{31}P solid-state NMR in dense dipolar networks. *J. Magn. Reson.* **165**, 18–32 (2003).
39. Schmedt auf der Günne, J. Effective dipolar couplings determined by dipolar dephasing of double-quantum coherences. *J. Magn. Reson.* **180**, 186 (2006).
40. Luschtinetz, R., Seifert, G., Jaehne, E. & Adler, H.-J. P. Infrared spectra of alkylphosphonic acid bound to aluminium surfaces. *Macromol. Symposia* **254**, 248–253 (2007).
41. Illy, N. et al. New prospects for the synthesis of N-alkyl phosphonate/phosphonic acid-bearing oligo-chitosan. *RSC Adv.* **4**, 24042–24052 (2014).
42. Vega, A., Thissen, P. & Chabal, Y. J. Environment-controlled tethering by aggregation and growth of phosphonic acid monolayers on silicon oxide. *Langmuir* **28**, 8046–8051 (2012).
43. Thissen, P., Valtiner, M. & Grundmeier, G. Stability of phosphonic acid self-assembled monolayers on amorphous and single-crystalline aluminum oxide surfaces in aqueous solution. *Langmuir* **26**, 156–164 (2010).
44. Turner, A. M., Abplanalp, M. J., Blair, T. J., Dayuha, R. & Kaiser, R. I. An infrared spectroscopic study toward the formation of alkylphosphonic acids and their precursors in extraterrestrial environments. *Astrophysical J. Suppl. Ser.* **234**, 6 (2018).
45. Moedritzer, K. Synthesis and properties of phosphinic and phosphonic acid anhydrides. *J. Am. Chem. Soc.* **83**, 4381 (1961).
46. Li, H., Dilipkumar, A., Abubakar, S. & Zhao, D. Covalent organic frameworks for CO_2 capture: from laboratory curiosity to industry implementation. *Chem. Soc. Rev.* **52**, 6294–6329 (2023).
47. del Olmo, D., Pavelka, M. & Kosek, J. Open-Circuit Voltage Comes from Non-Equilibrium Thermodynamics. *J. Non-Equilib.Thermodyn.* **46**, 91–108 (2021).
48. Liu, M. et al. Post-synthetic modification of covalent organic frameworks for CO_2 electroreduction. *Nat. Commun.* **14**, 3800 (2023).
49. Lin, J.-B. et al. A scalable metal-organic framework as a durable physisorbent for carbon dioxide capture. *Science* **374**, 1464–1469 (2021).
50. Boyd, P. G. et al. Data-driven design of metal–organic frameworks for wet flue gas CO_2 capture. *Nature* **576**, 253–256 (2019).
51. Zeng, Y., Zou, R. & Zhao, Y. Covalent organic frameworks for CO_2 capture. *Adv. Mater.* **28**, 2855 (2016).
52. Sing, K. S. W. Reporting physisorption data for gas/solid systems with special reference to the determination of surface area and porosity (Recommendations 1984). **57**, 603–619 (1985).
53. Thommes, M. et al. Physisorption of gases, with special reference to the evaluation of surface area and pore size distribution. *Pure Appl. Chem.* **87**, 1051–1069 (2015).
54. Nuhnen, A. & Janiak, C. A practical guide to calculate the isosteric heat/enthalpy of adsorption via adsorption isotherms in metal–organic frameworks, MOFs. *Dalton Trans.* **49**, 10295–10307 (2020).
55. Xu, K., Pecher, O., Braun, M. & Schmedt auf der Günne, J. Stable magic angle spinning with Low-Cost 3D-Printed parts. *J. Magn. Reson.* **333**, 107096 (2021).
56. Harris, R. & Becker, E. NMR nomenclature: nuclear spin properties and conventions for chemical shifts—IUPAC recommendations. *J. Magn. Reson.* **156**, 323–326 (2002).
57. Jardón-Álvarez, D. & Schmedt auf der Günne, J. Reduction of the temperature gradients in laser assisted high temperature MAS NMR. *Solid State Nucl. Magn. Reson.* **94**, 26–30 https://doi.org/10.1016/j.ssnmr.2018.08.002 (2018)
58. Bak, M., Rasmussen, J. T. & Nielsen, Simpson, N. C. A general simulation program for solid-state NMR spectroscopy. *J. Magn. Reson.* **147**, 296–330 (2000).
59. Tošner, Z. et al. Computer-intensive simulation of solid-state NMR experiments using SIMPSON. *J. Magn. Reson* **246**, 79–93 (2014).
60. Kühne, T. D. et al. CP2K: an electronic structure and molecular dynamics software package - quickstep: efficient and accurate electronic structure calculations. *J. Chem. Phys.* **152**, 194103 (2020).
61. Grimme, S., Antony, J., Ehrlich, S. & Krieg, H. A consistent and accurate ab initio parametrization of density functional dispersion correction (DFT-D) for the 94 elements H-Pu. *J. Chem. Phys.* **132**, 154104 (2010).
62. Grimme, S., Ehrlich, S. & Goerigk, L. Effect of the damping function in dispersion corrected density functional theory. *J. Computational Chem.* **32**, 1456–1465 (2011).
63. Perdew, J. P., Burke, K. & Ernzerhof, M. Generalized gradient approximation made simple. *Phys. Rev. Lett.* **77**, 3865 (1996).
64. Goedecker, S., Teter, M. & Hutter, J. Separable dual-space Gaussian pseudopotentials. *Phys. Rev. B* **54**, 1703–1710 (1996).
65. Hartwigsen, C., Goedecker, S. & Hutter, J. Relativistic separable dual-space Gaussian pseudopotentials from H to Rn. *Phys. Rev. B* **58**, 3641–3662 (1998).
66. Krack, M. Pseudopotentials for H to Kr optimized for gradient-corrected exchange-correlation functionals. *Theor. Chem. Acc.* **114**, 145–152 (2005).
67. Bussi, G., Donadio, D. & Parrinello, M. Canonical sampling through velocity rescaling. *J. Chem. Phys.* **126**, 014101 (2007).
68. Weber, J., Seemann, M. & Schmedt auf der Günne, J. Pulse-transient adapted C-symmetry pulse sequences. *Solid State Nucl. Magn. Reson.* **43–44**, 42–50 https://doi.org/10.1016/j.ssnmr.2012.02.009 (2012)
69. Lee, Y. K. et al. Levitt Efficient dipolar recoupling in the NMR of rotating solids. A sevenfold symmetric radiofrequency pulse sequence. *Chem. Phys. Lett.* **242**, 304–309 (1995).

Acknowledgements
K.X., R.O. and T.H.H.S. are equally contributing first authors. We appreciate the support of the Interdisciplinary Centre for Analytics on the Nanoscale of the University of Duisburg. Gündoğ Yücesan and Jens Beckmann thank DFG for funding their research with grant numbers YU 267/2-1, YU 267/9-1, and BE 3716/9-1. M.S. gratefully acknowledges funding by a materials cost allowance of the Fonds der Chemischen Industrie e.V. and financial support by the "Young College" of the North-Rhine Westphalian Academy of Sciences, Humanities and the Arts. K.X., R.O., and T.H.H.S. are equally contributing first authors.

Author contributions
K.X. performed the NMR characterizations, generated the corresponding figures and contributed to the manuscript. J.S.G. did the analysis of the DQ NMR experiments. R.O. resynthesized the compound, performed gas sorption measurements, organized the TEM measurements at Forschungszentrum Julich, and performed TGA-MS measurements, and wrote the corresponding gas sorption section. T.H.H.S. performed the PXRD work and the chemical stability testing. M.L. performed the temperature variable FT-IR measurements and wrote the corresponding section. J.G.A.R. performed the SEM-EDX analysis and the electrochemical stability testing and wrote the corresponding section. J.M. performed the XPS and wrote the corresponding section. Philipp Seiffert performed the TGA experiments and Till Strothmann designed the TGA-MS experiments. P.T. synthesized reproduced GTUB5 to be used in this work. Y.Z. synthesized the second batch of GTUB5 and contributed to the figures. A.O.Y. performed the DFT calculations and wrote the corresponding section. M.S. performed the optical measurements and wrote the corresponding section. V.P. supervised the work of J.G.A.R. and contributed to the corresponding text. T.P. supervised the FT-IR studies and contributed to the corresponding text. C.J. supervised the gas sorption for BET measurements and edited the manuscript. G.Y. and J.S.G. created the hypothesis, supervised the entire project and wrote the introduction and conclusion and edited the entire manuscript. J.B. provided helpful insights and discussions during the work and contributed to the manuscript. All authors have approved the final version of the manuscript.

Funding
Open Access funding enabled and organized by Projekt DEAL.

Competing interests
Gündoğ Yücesan has filed a patent for the condensed microporous phosphonic acids. The other authors declare no competing interests.

Additional information
Supplementary information The online version contains supplementary material available at https://doi.org/10.1038/s41467-024-51950-1.

Correspondence and requests for materials should be addressed to Jörn Schmedt auf der Günne or Gündoğ Yücesan.

Peer review information *Nature Communications* thanks Henning Jessen, Ruqiang Zou and the other, anonymous, reviewer(s) for their contribution to the peer review of this work. A peer review file is available.

Supplementary Information

Polyphosphonate Covalent Organic Frameworks

Ke Xu,[‡1] Robert Oestreich,[‡2] Takin Haj Hassani Sohi,[‡2] Mailis Lounasvuori,[3] Jean G. A.Ruthes,[4,5] Yunus Zorlu,[6] Julia Michalski,[2] Philipp Seiffert,[2] Till Strothmann,[2] Patrik Tholen,[7] A. Ozgur Yazaydin,[8] Markus Suta,[2] Volker Presser,[4,5] Tristan Petit,[3] Christoph Janiak,[2] Jens Beckmann,[9] Jörn Schmedt auf der Günne[1], Gündoğ Yücesan[2]**

1. Department of Chemistry and Biology, Inorganic Materials Chemistry, University of Siegen, Adolf-Reichwein-Straße 2, 57076 Siegen, Germany
2. Institut für Anorganische Chemie und Strukturchemie, Heinrich-Heine-Universität Düsseldorf, Universitätsstraße 1, 40225 Düsseldorf, Germany
3. Young Investigator Group Nanoscale Solid-Liquid Interfaces, Helmholtz-Zentrum Berlin für Materialien und Energie GmbH, Albert-Einstein-Straße 15,12489 Berlin, Germany
4. INM – Leibniz Institute for New Materials, Campus D22, 66123 Saarbrücken, Germany.
5. Department of Materials Science and Engineering, Saarland University, Campus D22, 66123 Saarbrücken, Germany.
6. Department of Chemistry, Gebze Technical University, Kocaeli, Türkiye.
7. Technische Universität Berlin, Lebensmittelchemie und Toxikologie, Gustav-Meyer-Allee 25, 13355 Berlin, Germany
8. Department of Chemical Engineering, University College London, London WC1E 7JE, United Kingdom
9. Institut für Anorganische Chemie und Kristallographie, Universität Bremen, Leobener Str. 7, Bremen 28359, Germany

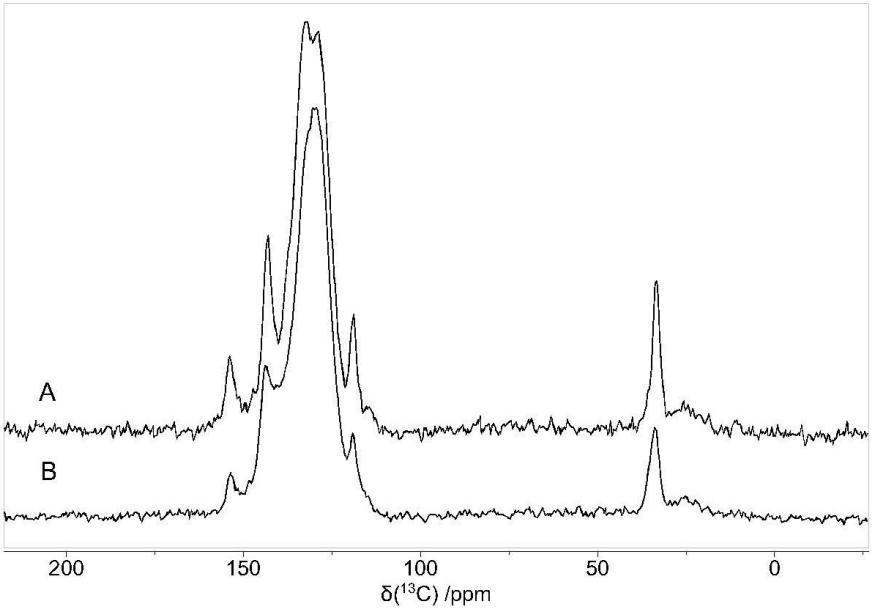

Supplementary Figure 1. $^{13}C\{^{1}H\}$ CP MAS NMR spectra of (A) GTUB5 and (B) GTUB5 after annealing at 220 °C.

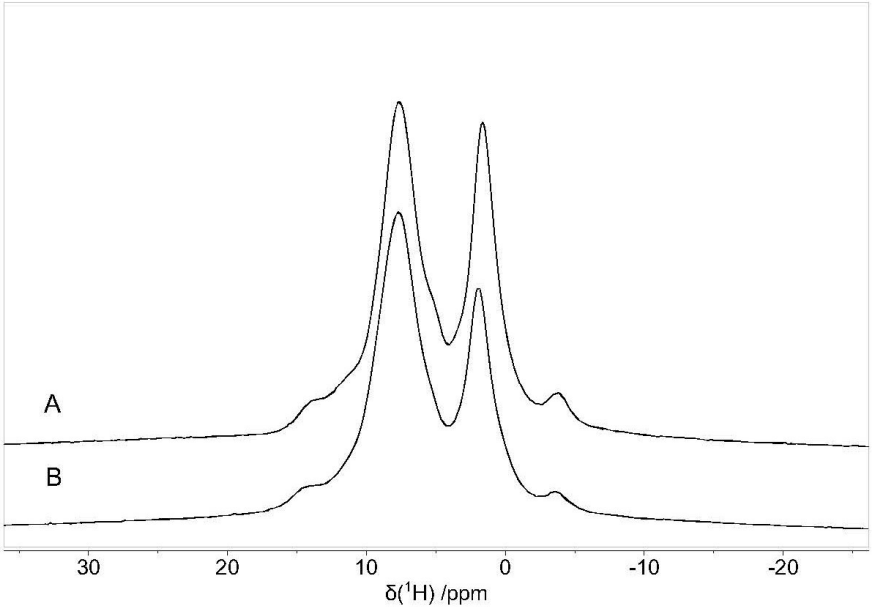

Supplementary Figure 2. ^{1}H MAS NMR spectra of (A) GTUB5 and (B) GTUB5 after annealing at 220 °C.

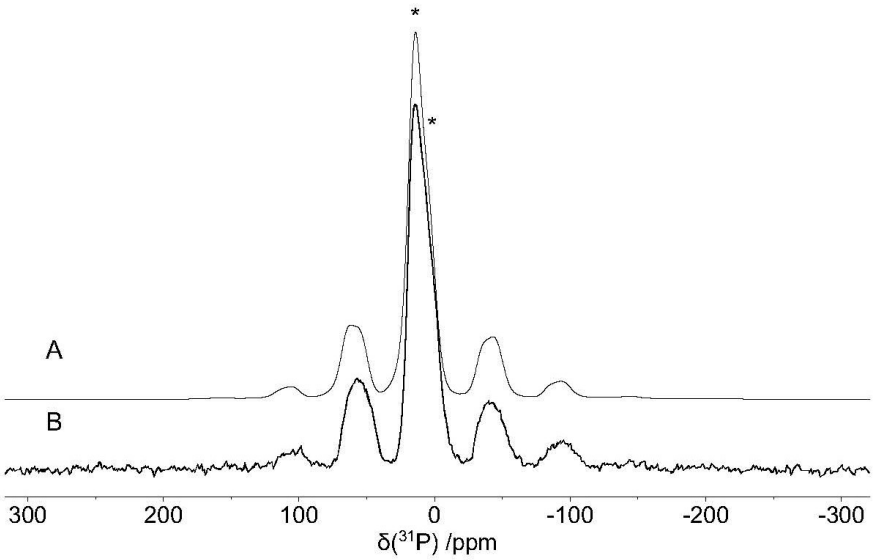

Supplementary Figure 3. Experimental (B) and simulated (A) ^{31}P MAS NMR of the GTUB5 sample after annealing at 220°C at a magnetic field of 14.1 T and a sample spinning frequency of 12 kHz.

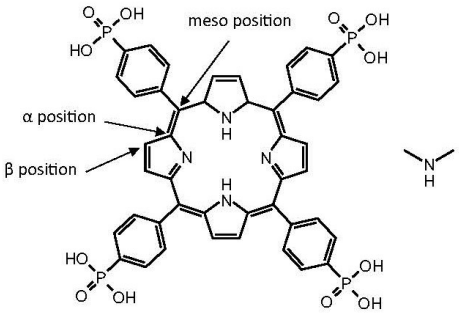

Supplementary Figure 4. Nomenclature of GTUB5 based on the nomenclature of porphyrin.

Supplementary Table 1. Isotropic chemical shift values by ^{1}H MAS NMR of GTUB5 before and after annealing at 220 °C (**Supplementary Figure 1**)

Environments	**δ_{iso}/ppm**
Ph	~7.7
N-CH_3	1.7
N-H	-3.8
H_β	~11
P-OH	11.0, 14.0

Supplementary Table 2. Isotropic chemical shift values of GTUB5 by ^{13}C MAS NMR before and after annealing at 220°C (**Supplementary Figure 2**) and peak assignment.

Environment	**δ_{iso}/ppm**
Ph	~130
N-CH_3	34
C_{meso}	119
C_α (C=N-C)	153
C_α (C-NH-C)	~130
C_β (C=N-C)	143
C_β (C-NH-C)	~130

Supplementary Table 3. The result of a non-linear least square fit of the ^{31}P MAS spinning spectrum using the SIMPSON simulation package[1] in combination with home-written fitting libraries of a sample of GTUB5 annealed at 230 °C.

	Peak A	Peak B
δ_{iso}/ppm	14.8	5.0
δ_{xx}/ppm	67.8	89.4
δ_{yy}/ppm	28.5	13.1
δ_{zz}/ppm	-52.0	-87.4
δ_{aniso}/ppm	-66.8	-92.4
η	0.59	0.83

Supplementary Table 4. The ^{31}P chemical shift values of a series of phosphonic acids and pyrophosphate from literature.

	R -PO_3H_2 [2]	R-P(OOH)-O-P(OOH)-R [3]	-[-O-P(O)OH-]$_n$- [4,5]	
R	δ_{iso}/ppm	δ_{iso}/ppm	$\delta_{iso}(Q^1)$/ppm	$\delta_{iso}(Q^2)$/ppm
Ph	15.7	7.1	-11	-22
$PhCH_2$	24.1	17.1		
$PhCH_2CH_2$	27.7	20.7		
PhCH=CH	16.7	7.1		
$PhC(CH_2)$	14.0	5.4		

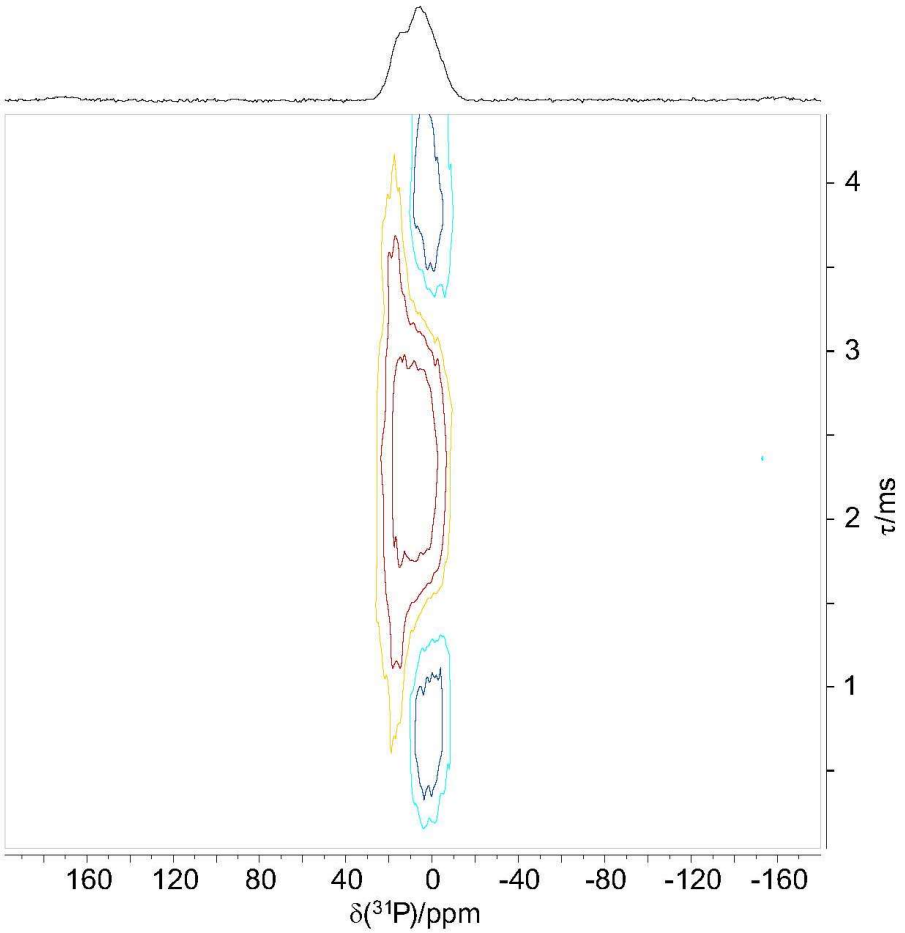

Supplementary Figure 5. Contour level plot of a ^{31}P double-quantum constant-time (DQCT) MAS NMR experiment of GTUB5 after annealing at 220 °C. The phase-adapted PostC7 pulse sequence was used at a spinning frequency of ν_r = 14286 Hz with a 7.04 T magnet and with a total double-conversion time of 4.48 ms.[6,7] The signal assigned to the monophosphonate groups does not show a zero crossing.

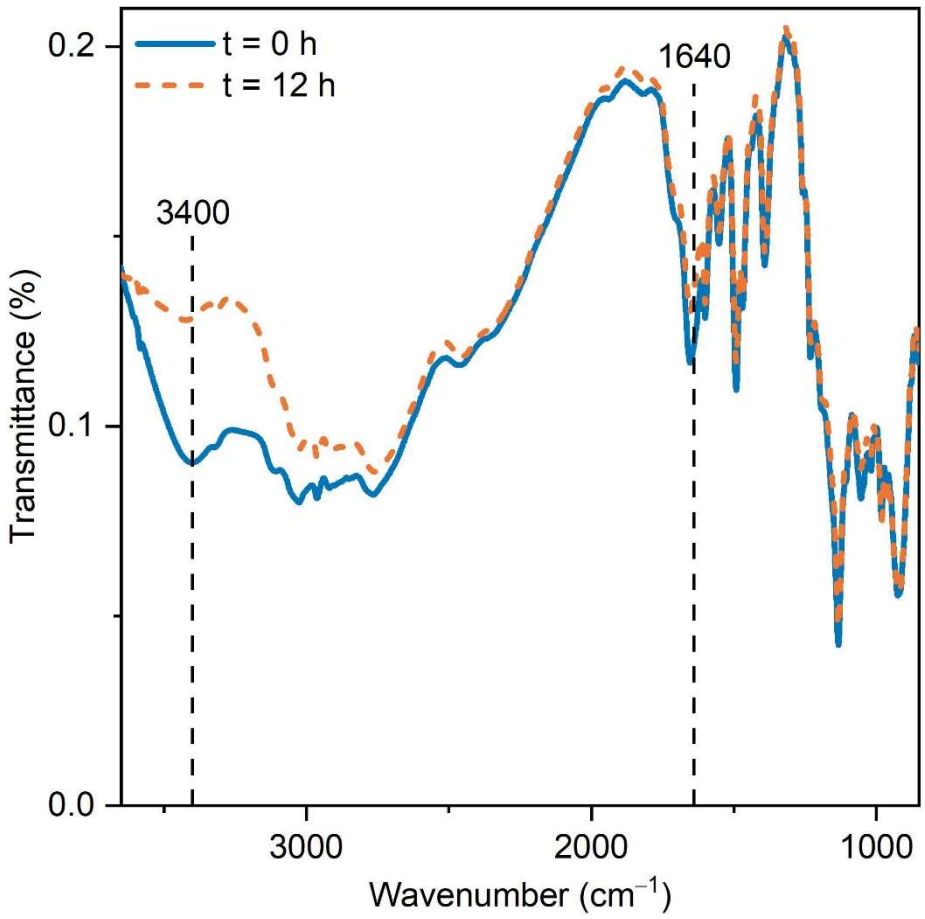

Supplementary Figure 6. Transmission spectra of GTUB-5 HOF at 50 °C (blue) and at 50 °C after 12 h in vacuum (orange).

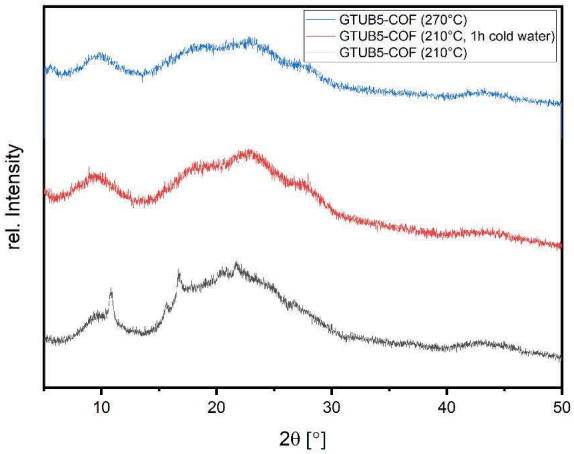

Supplementary Figure 7: Powder X-ray diffractograms measured from 5° to 50° 2θ after heating to 210 °C and 270 °C, and subsequent test in cold water for 1 h.

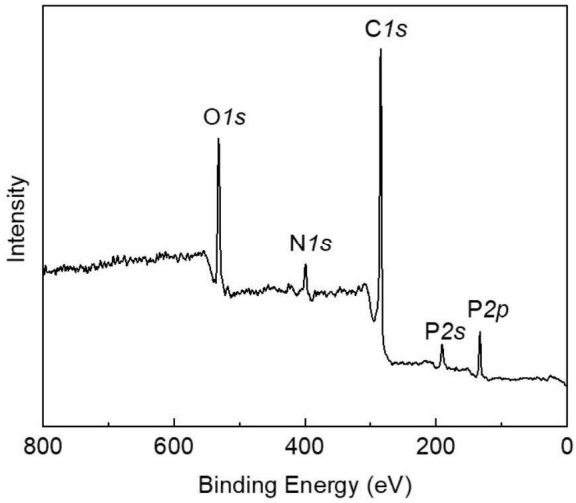

Supplementary Figure 8. X-ray photoelectron spectra of GTUB5 heated to 270. °C .

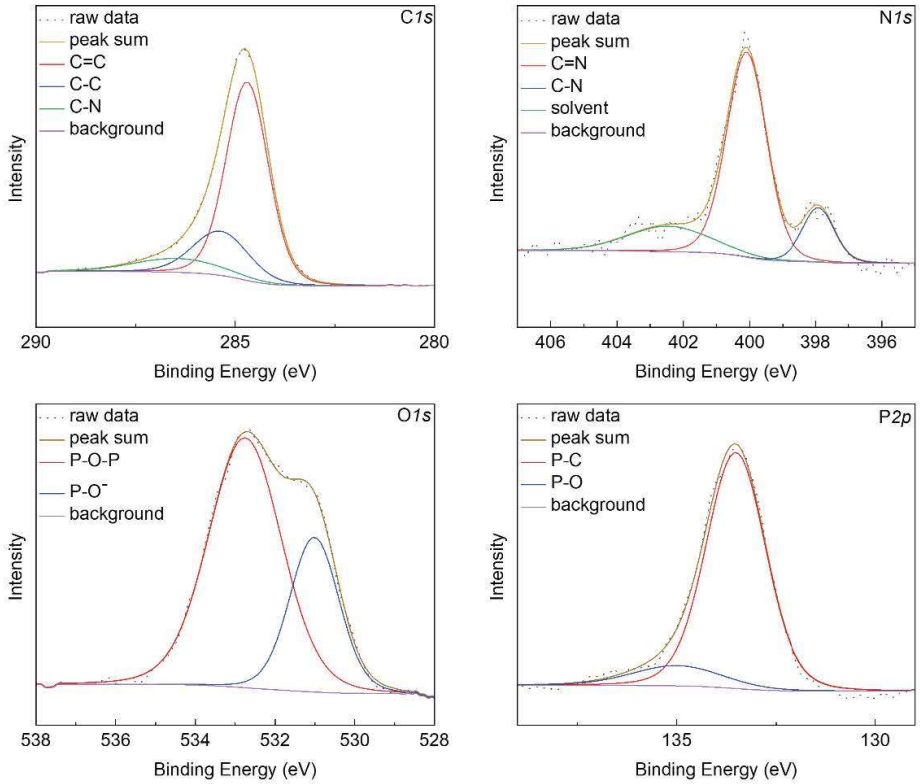

Supplementary Figure 9. High resolution X-ray photoelectron spectra of C *1s*, N *1s*, O *1s*, and P *2p* of GTUB5.

Supplementary Table 5. XPS peak types and corresponding binding energies of carbon in GTUB5.

Element	Characteristic peak	C=C (eV)	C-C (eV)	C-N (eV)
C	C *1s*	284.5	284.8	286

Supplementary Table 6. XPS peak types and corresponding binding energies of oxygen in GTUB5.

Element	Characteristic peak	P-O-P (eV)	$P\text{-}O^-$ (eV)
O	O *1s*	532.7	531

Supplementary Table 7. XPS peak types and corresponding binding energies of nitrogen in GTUB5.

Element	Characteristic peak	C=N (eV)	C-N (eV)	Solvent (eV)
N	N *1s*	400	397	402.4

Supplementary Table 8. XPS peak types and corresponding binding energies of nitrogen in GTUB5.

Element	Characteristic peak	P-C (eV)	P-O (eV)
P	P *2p*	133.5	134.9

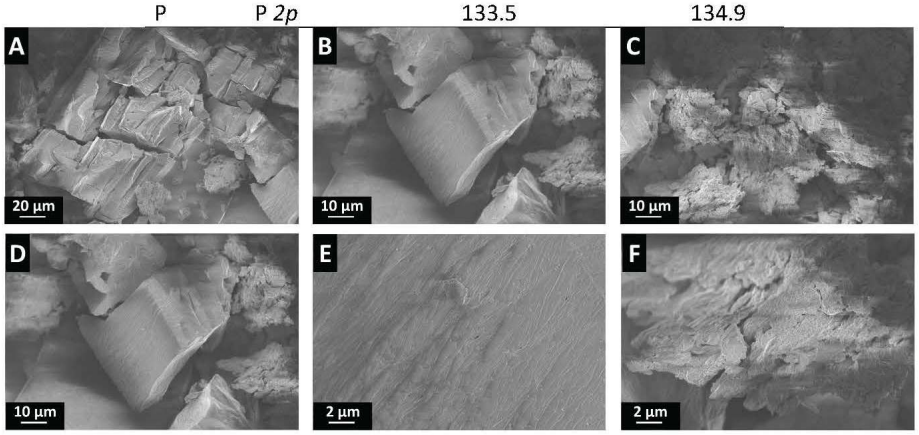

Supplementary Figure 10. Scanning electron micrographs of GTUB5-COF heated after 270 °C in different magnifications. A) 20 µm, B) 10 µm, C) 10 µm from depicting the right side of B, D) 10µm, E) 2µm view of B, F) 2µm view of C.

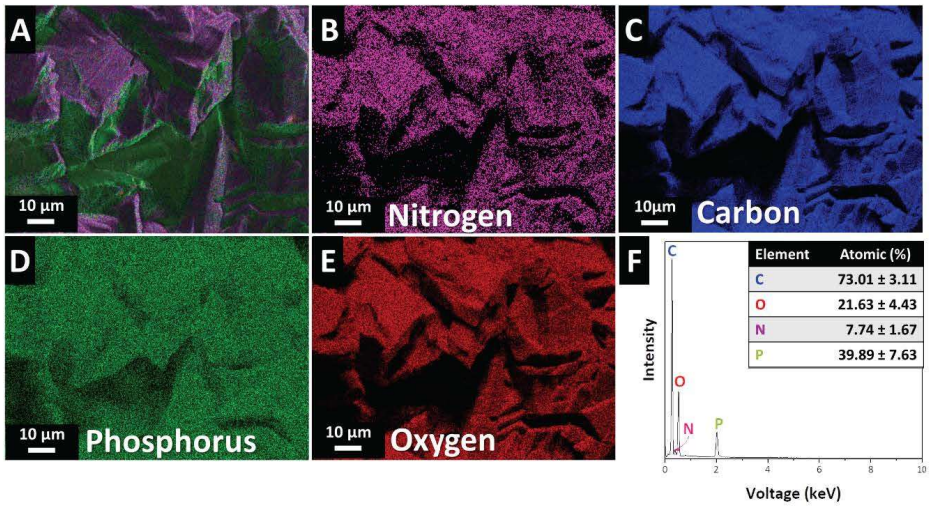

Supplementary Figure 11. Energy dispersive X-ray spectroscopy mapping of GTUB-COF heated 270 °C in different magnifications. A) Region mapped, B) Nitrogen mapping, C) Carbon mapping, D) Phosphorous mapping, E) Oxygen mapping, and F) Elemental analysis from 25 points collected. Inset: Atomic ratio of elemental analysis.

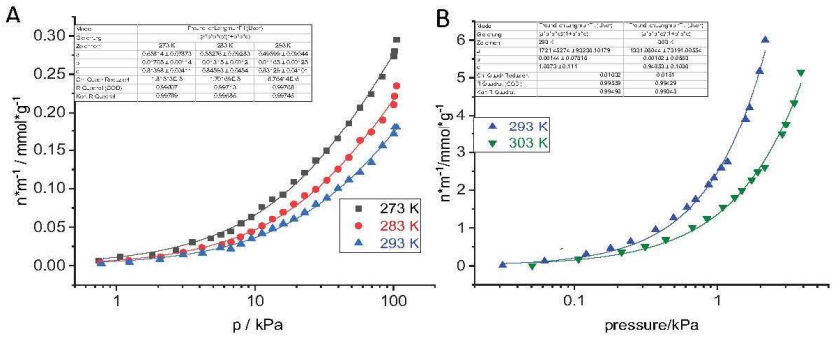

Supplementary Figure 12. A) CO_2 adsorption isotherms at different temperatures with Freundlich-Langmuir-Fit and corresponding equations. B) Water adsorption isotherms at different temperatures with Freundlich-Langmuir-Fit and corresponding equations.

Supplementary Table 9. Selected COFs from the literature with respect to their stabilities and heat of adsorption. The data are taken from references [8-10]

COF	CO_2 adsorption at 273 K and 0.95 bar (cm^3g^{-1})	Enthalpy of adsorption of CO_2 ($kJmol^{-1}$)	Stability tests
GTUB-5	6	-27	Cold and hot water; heat
TEPA(10)-COF-1	58	-37.5	Storage under humid air
POSS-TPA-COF	58	-26.3	Heat; water, acid, base, organic solvents
CO_2-COF	23	Not given	Heat; humidity
CTF-1	55	-31	Humidity

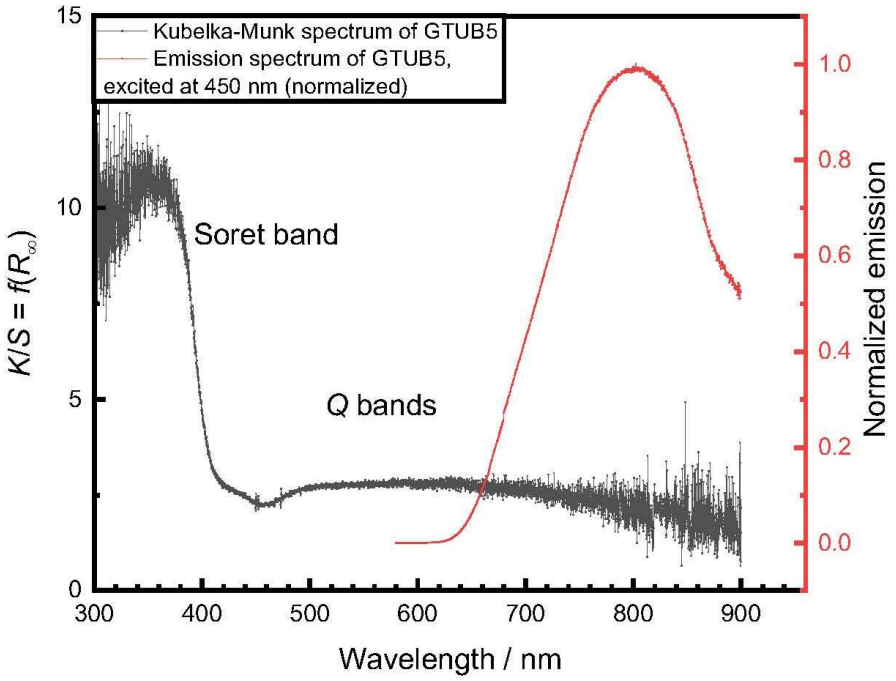

Supplementary Figure 13. Optical spectra of GTUB5 at 270 °C. Kubelka-Munk spectrum (black) as derived from diffuse reflectance spectra at room temperature and emission spectrum (excited at 450 nm at room temperature) of GTUB5 crystals heated at 270 °C.

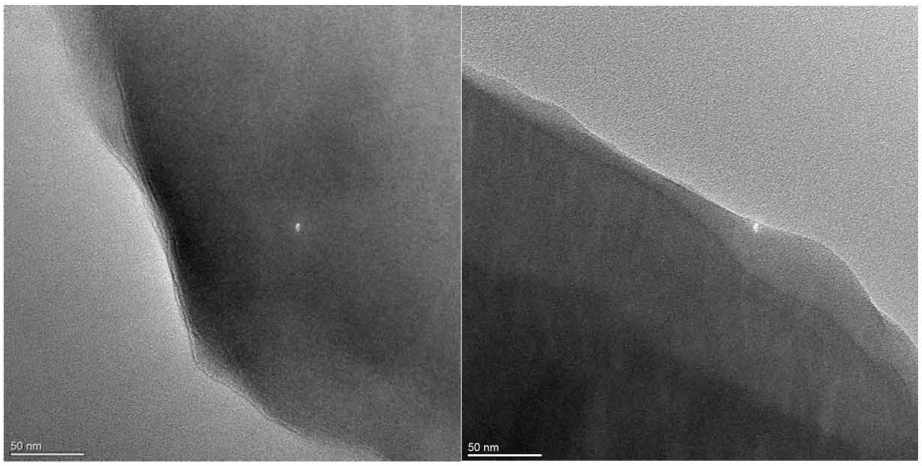

Supplementary Figure 14. Transmission electron micrographs of GTUB5 heated to 270°C.

Supplementary Information References

(1) Bak, M., Rasmussen, J. T., Nielsen, Simpson, N. C. A General Simulation Program for Solid-State NMR Spectroscopy. *Journal of Magnetic Resonance*, 147, 296-330 (2000). DOI: https://doi.org/10.1006/jmre.2000.2179.

(2) Han, X.-H., Gong, K.; Huang, X., Yang, J.-W., Feng, X., Xie, J., Wang, B. Syntheses of Covalent Organic Frameworks via a One-Pot Suzuki Coupling and Schiff's Base Reaction for C_2H_4/C_3H_6 Separation. *Angewandte Chemie International Edition*, 61, e202202912 (2022), https://doi.org/10.1002/anie.202202912.

(3) Abuzeid, H. R., El-Mahdy, A. F. M., Kuo, S.-W. Covalent organic frameworks: Design principles, synthetic strategies, and diverse applications. *Giant*, 6, 100054 (2021). DOI: https://doi.org/10.1016/j.giant.2021.100054.

(4) Jessen, H. J., Dürr-Mayer, T., Haas, T. M., Ripp, A.; Cummins, C. C. Lost in Condensation: Poly-, Cyclo-, and Ultraphosphates. *Accounts of Chemical Research*, 54, 4036-4050 (2021). DOI: 10.1021/acs.accounts.1c00370.

(5) Schülke, U., Kayser, R., Neumann, P. Zur Darstellung von Cyclophosphaten, Cyclophosphatophosphonaten, Diphosphonaten und Diphosphiten in Harnstoffschmelzen. *Zeitschrift für anorganische und allgemeine Chemie*, 576, 272-280 (1989). DOI: https://doi.org/10.1002/zaac.19895760131

(6) Weber, J., Seemann, M., Schmedt auf der Günne, J. Pulse-transient adapted C-symmetry pulse sequences. *Solid State Nuclear Magnetic Resonance*, 43-44, 42-50 (2012). DOI: https://doi.org/10.1016/j.ssnmr.2012.02.009.

(7) Schmedt auf der Günne, J. Distance measurements in spin-1/2 systems by ^{13}C and ^{31}P solid-state NMR in dense dipolar networks. *Journal of Magnetic Resonance*, 165, 18-32 (2003). DOI: https://doi.org/10.1016/S1090-7807(03)00242-8.

(8) Jia, C., Liang, R.-R., Gan, S.-X., Jiang, S.-Y., Qi, Q.-Y., Zhao, X. Boosting Hydrostability and Carbon Dioxide Capture of Boroxine-Linked Covalent Organic Frameworks by One-Pot Oligoamine Modification. *Chemistry – A European Journal*, 29, e202300186 (2023). DOI: https://doi.org/10.1002/chem.202300186

(9) Qiao, G.-Y., Wang, X.; Li, X., Li, J., Geng, K., Jin, E., Xu, J.-J., Yu, J. Unlocking Synthesis of Polyhedral Oligomeric Silsesquioxane-Based Three-Dimensional Polycubane Covalent Organic Frameworks. *Journal of the American Chemical Society*, 146, 3373-3382 (2024). DOI: 10.1021/jacs.3c12650.

(10) Zhang, S., Lombardo, L., Tsujimoto, M., Fan, Z., Berdichevsky, E. K., Wei, Y.-S., Kageyama, K., Nishiyama, Y., Horike, S. Synthesizing Interpenetrated Triazine-based Covalent Organic Frameworks from CO_2. *Angewandte Chemie International Edition*, 62, e202312095 (2023). DOI: https://doi.org/10.1002/anie.202312095.

3.2 Stable Ultramicroporous Metal–Organic Framework with Hydrophilic and Hydrophobic Domains for Selective Gas Adsorption

Oestreich, R.; Fetzer, M. N. A.; Zhang, Y.; Schreiber, A.; Knebel, A.; Suta, M.; Janiak, C.; Hanna, G. & Yücesan, G.

Stable Ultramicroporous Metal–Organic Framework with Hydrophilic and Hydrophobic Domains for Selective Gas Adsorption

Angewandte Chemie International Edition, Wiley, **2025**, *64*

Summary: In this publication the thermal and chemical stability as well as the gas adsorption behavior of a phosphonate MOF with mixed linkers, [Cu(4,4'-bpy)0.5(1,4-$NDPAH_2$)], called TUB41 (where bpy = bipyridine and $NDPAH_4$ = naphthalenediphosphonic acid) were described. TUB41 exhibits remarkable chemical stability over a wide pH range (1–11) and maintains its structural integrity even after two years of repeated adsorption cycles and activation at 80 °C under ambient humidity. Cryogenic adsorption experiments show that the pores of TUB41 selectively exclude gases with larger kinetic diameters, such as N_2 and Ar, while absorbing smaller molecules, such as CO_2 and H_2O, at elevated temperatures. The adsorption enthalpies for CO_2 at a loading of 0.01 mmol g−1 and H_2O at a loading of 0.7 mmol g−1 are −41 and −38 kJ mol−1, respectively, reflecting their strong attractive forces with TUB41 under different conditions. Molecular dynamics simulations show that CO_2 molecules, under the influence of strong non-bonding interactions, adopt an ordered arrangement in the central hydrophobic regions of the pores, while H_2O molecules preferentially bind to the hydrophilic secondary building blocks. Analyses of the mean square displacement confirm that both gases remain spatially confined within the pores.

Contributions to this work:

- Design and Performance of gas sorption studies
- Performance of optical measurements under supervision by Professor Markus Suta
- Writing of these parts for the manuscript
- Control and reworking of the manuscript
- Marcus Fetzer resynthesized TUB41, developed a new method for the linker synthesis, and performed the stability experiments and took SEM pictures.
- Yifei Zhang set up and performed the MD simulations, generated the corresponding figures, and wrote the initial drafts of the computational parts of the manuscript.
- Andreas Schreiber performed the repeat of N_2 and Ar adsorption measurements,

- Alexander Knebel performed the in situ temperature variable PXRD measurements and wrote the corresponding section,
- Professor Markus Suta supervised the optical measurements, wrote the corresponding section, and edited the manuscript.
- Professor Doctor Christoph Janiak supervised and interpreted the gas adsorption work, created the crystallographic figures, and edited the manuscript.
- Gabriel Hanna supervised the work of Yifei Zhang, provided critical feedback on several experimental sections of the manuscript, revised the computational parts of the manuscript, and edited the entire manuscript.
- Gündoğ Yücesan created the hypothesis, supervised the work of Marcus Fetzer and Robert Oestreich, and wrote the majority of the abstract, introduction, conclusion sections, and contributed experimental sections of the manuscript.

GDCh Research Article Angewandte Chemie International Edition www.angewandte.org

Check for updates

How to cite: *Angew. Chem. Int. Ed.* **2025**, *64*, e202513788
doi.org/10.1002/anie.202513788

Metal-Organic Frameworks

Stable Ultramicroporous Metal–Organic Framework with Hydrophilic and Hydrophobic Domains for Selective Gas Adsorption

Robert Oestreich[+], Marcus N. A. Fetzer[+], Yifei Zhang, Andreas Schreiber, Alexander Knebel, Markus Suta, Christoph Janiak, Gabriel Hanna,* and Gündoğ Yücesan**

Abstract: Herein, we report the thermal and chemical stability, and the gas adsorption behavior, of a mixed-linker phosphonate MOF, $[Cu(4,4'\text{-bpy})_{0.5}(1,4\text{-NDPAH}_2)]$, namely TUB41 (where bpy = bipyridine and $NDPAH_4$ = naphthalenediphosphonic acid). TUB41 demonstrates remarkable chemical stability across a wide pH range (1–11) and retains its structural integrity after 2 years of repeated adsorption cycles and activation at 80 °C under ambient humidity. Cryogenic adsorption experiments reveal that TUB41's pores selectively exclude gases with larger kinetic diameters, such as N_2 and Ar, while accommodating smaller molecules like CO_2 and H_2O at elevated temperatures. The enthalpies of adsorption for CO_2 at a loading 0.01 mmol g^{-1} and H_2O at a loading of 0.7 mmol g^{-1} are −41 and −38 kJ mol^{-1}, respectively, reflecting their strongly attractive interactions with TUB41 under different conditions. Molecular dynamics simulations reveal that CO_2 molecules adopt ordered arrangements in the central hydrophobic regions of the pores, guided by strong nonbonding interactions, while H_2O molecules preferentially bind to the hydrophilic secondary building units. Mean-squared displacement analyses confirm that both gases remain spatially constrained within the pores. These findings highlight TUB41 as a chemically robust and highly selective MOF, with potential for applications in gas separation, photocatalytic water splitting, and CO_2 reduction under challenging conditions.

Introduction

Metal–organic frameworks (MOFs) have evolved as one of the most studied material classes with a wide range of potential industrial applications in medicine, food chemistry, catalysis, energy storage, and many others.[1–4] For each application, MOFs must possess unique chemical and thermal stabilities suitable for the desired application. For example, biodegradability is an essential requirement for MOFs to be used for applications such as drug delivery,[5–9] while MOFs intended for use in batteries, supercapacitors, electrocatalysis (including hydrogen evolution and oxygen evolution reactions), CO_2 capture, and water harvesting must demonstrate sufficient stability to survive in the presence of electrolytes, water, and acidic or basic environments.[10] Despite the rich structural diversity of MOFs and their vast potential applications,[2] there still is only a handful of MOFs in the literature, which are considered to be stable in the presence of water, acids, bases, and electrolytes.[11,12] Notably, UiO-66, which is known for its exceptional stability, has a shelf lifetime of ca. 2 months at room temperature and ambient humidity.[13,14] Therefore, the development of highly stable MOFs would finally open the way towards the wide-spread industrial use of MOFs. The secondary building units (SBUs) of conventional carboxylate MOFs are usually composed of water-labile metal carboxylate clusters, including Zr(IV) carboxylate clusters (as in UiO-66), which limit conventional MOF applications in aqueous media.[14] Furthermore, the CO_2 adsorption process also generates an acidic environment, which is challenging for conventional MOFs to survive for a

[*] R. Oestreich[+], M. N. A. Fetzer[+], C. Janiak, G. Yücesan
Institute for Inorganic and Structural Chemistry, Heinrich Heine University Düsseldorf, Universitätsstr. 1, D-40225 Düsseldorf, Germany
E-mail: janiak@hhu.de
guendog.yuecesan@hhu.de

M. Suta
Inorganic Photoactive Materials, Institute for Inorganic and Structural Chemistry, Heinrich Heine University Düsseldorf, Universitätsstr. 1, 40225 Düsseldorf, Germany

A. Schreiber
Microtrac Retsch GmbH, Retsch-Allee 1–5, D-42781 Haan, Germany

A. Knebel
Otto Schott Institute of Materials Research, Center for Energy and Environmental Chemistry II, Friedrich Schiller University Jena, Lessingstraße 12–14, D-07743 Jena, Germany

A. Knebel
Center for Energy and Environmental Chemistry, Friedrich Schiller University Jena, Philosophenweg 7a, D-07743 Jena, Germany

Y. Zhang, G. Hanna
Department of Chemistry, University of Alberta, Edmonton, Alberta, Canada
E-mail: gabriel.hanna@ualberta.ca

[+] Both authors contributed equally to this work.

Additional supporting information can be found online in the Supporting Information section

long period of time.[15] Phosphonic acid-based MOFs provide a promising route to achieving stability in acidic media.[16] Compared to conventional metal-binding functional groups, phosphonic acids are very robust organic linkers that survive in the presence of concentrated acids, and the P–C bond is known to be stable in the presence of UV-light and at high temperatures.[17,18] The formation of insoluble metal phosphonate SBUs is advantageous because it enhances the structural stability of the MOF in aqueous environments, unlike metal acetate SBUs, which are typically water-soluble and prone to degradation.[17,19,20]

While significant progress has been made in developing amine-functionalized MOFs for CO_2 capture via chemisorption (where CO_2 forms covalent bonds with amine groups), physisorptive capture remains a greater challenge.[15] This is largely due to the intrinsic hydrophilicity of many MOFs, which are often constructed from organic linkers bearing polar functional groups and SBUs that interact favorably with water vapor.[21] Although physisorption is technically simpler and more energy-efficient than chemisorption, especially when employing pressure swing adsorption, achieving selective CO_2 uptake in the presence of humidity has proven difficult.[22] Only a few MOFs have been reported to exhibit CO_2 selectivity under humid conditions.[15] Among them, CALF-20 shows promising performance at 10% RH but loses selectivity entirely at 40% RH.[15] Moreover, its chemical stability was tested only under gas-phase conditions in the original study. While amine-based systems and frameworks like MOF-74 demonstrate high CO_2 capacities, their chemical instability under humid or acidic/basic aqueous conditions severely limits practical applications.[23–27] Some well-studied MOFs, such as MOF-74 and DEF-2, decompose rapidly in air, and others lack reported stability data altogether.[23,25] Most chemical stability tests for CO_2-adsorbing MOFs rely on repeated adsorption-desorption cycles. As summarized in several review articles, only a few MOFs have demonstrated exceptional long-term stability in various chemical media. Notable examples include MIL-100(Cr), which remains stable in water for up to one year; $Ni(BTP)_2$, which retains its structural integrity for 14 days across a wide pH range (2 to 14); and ZIF-8, which is stable for 7 days in boiling organic solvents and water, and for 24 h in boiling NaOH.[11,28] One approach to overcoming this limitation involves designing chemically stable MOFs with unconventional organic linkers containing phosphonic acid functional groups.[29–31] These groups form strong coordination bonds with metal ions, leading to the formation of water-insoluble metal phosphonate SBUs that are highly resistant to hydrolysis in acidic/basic media.[29,31] Such MOFs offer a promising route towards physisorptive CO_2 capture that remain stable and selective in humid environments.

Our group and others have reported the stability of phosphonate MOFs in harsh environments, including strong acids, bases, and even aqua regia, making them highly promising candidates for diverse applications such as electrocatalysis, energy storage, and sequestration of greenhouse gases.[17,30–32] Additionally, our investigations into hydrogen-bonded organic frameworks (HOFs) and polyphosphonate covalent organic frameworks (COFs) constructed from phosphonic acids have shown exceptional stability in humid environments during and after proton conductivity experiments.[33–36] Although the short-term chemical stability of phosphonate MOFs is well-documented, their long-term stability over extended periods has, to the best of our knowledge, not been reported in the literature. It has been also shown that metal phosphonates might be electrically conductive.[4,37,38] Despite their inherent chemical stability and promising potential for applications in gas storage, energy storage, and catalysis, phosphonate MOFs remain relatively underexplored. Their development is largely hindered by the limited commercial availability of arylphosphonic acid linkers and fundamental phosphonate precursors.[29] Overcoming these challenges is essential for advancing the design of sustainable MOF families capable of operating in harsh chemical environments.

In this work, we focus on naphthalene as a linker core, which is a hydrophobic and polyaromatic moiety to create MOFs that could capture CO_2.[33] Previously, we published a structural report on TUB41, a mixed-linker MOF utilizing 1,4-naphthalenediphosphonic acid (1,4-$NDPAH_4$) and 4,4′-bipyridine (4,4′-bpy) (see Figure 1a).[39] However, due to its very low yield, we were not able to work on its applications previously. In this work, we synthesized TUB41 hydrothermally as a single product phase in high yield, and thus were able to study its chemical/thermal stability. Furthermore, since TUB41 has narrow and largely hydrophobic pores, which are suitable for sequestering molecules with small kinetic diameters (e.g., CO_2 and H_2O), we studied its ability to capture CO_2 and H_2O. Notably, TUB41 was found to have a shelf lifetime of beyond 2 years after repeated gas adsorption experiments and activation at 80 °C under vacuum, which is a major improvement over the 2 months for conventional carboxylate-based MOFs such as UiO-66.

In more detail, as shown in Figure 1b, TUB41 has a rod-shaped SBU composed of typical eight-membered Cu-O-P-O-Cu-O-P-O rings observed in phosphonate MOFs, which are bridged by the square pyramidal Cu(II) atoms. The hydrogen bonding between the Cu(II)-coordinating phosphonate groups defines the final shape of the SBU and provides a hydrophilic character to the SBU. The hydrophilic SBUs with hydrogen bonds are surrounded by hydrophobic naphthalene moieties, hypothetically limiting the noncovalent interactions of the SBU with hydrophilic gases and generating a more preferable environment for gases such as CO_2. Recently, MOF research has focused on frameworks with narrow pores to enhance gas adsorption selectivity.[40] The combination of narrow pores and a pronounced hydrophobicity in TUB41, along with its thermal and chemical stability, makes it highly desirable for the development of industrial MOF applications that can selectively capture or separate gases such as CO_2 in the presence of H_2O.[41,42]

Chemical Stability of TUB41

The crystals of TUB41 were reproduced in Fall 2022. Chemical stability tests on TUB41 were performed by suspending

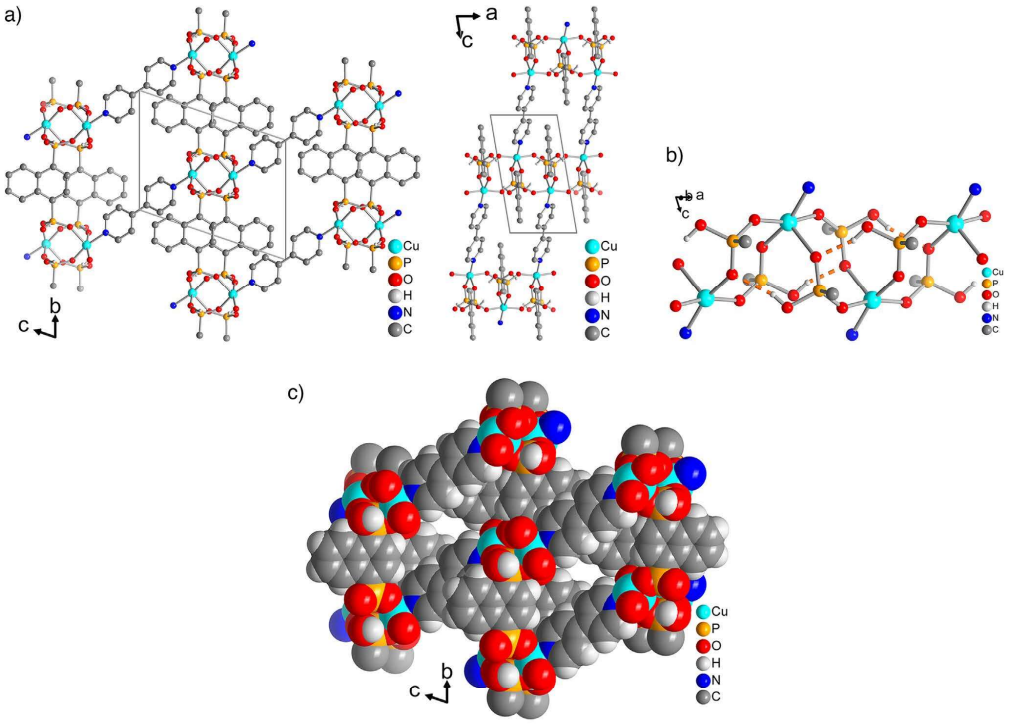

Figure 1. a) Section of the packing in the crystal structure of TUB41 along two different viewing directions (hydrogen atoms on carbon are omitted for clarity). b) SBU of TUB41 running along the *a* direction, showing the hydrogen bonds between the phosphonate groups. c) Space-filling representation to visualize the small ~4 × 2 Å^2 cross section of the slit-shaped channels along the *a* axis (cf. Figure S18 for a grid scale).

TUB41 crystals in aqueous HCl and NaOH solutions ranging in pH between 1 and 13 for 2 h. In addition, TUB41 samples were left in the hydrothermal reaction mixture (an aqueous medium of pH 2.5) for ca. 1 month before the purification of the crystals, pointing to its stability. As depicted in Figure 2a, the powder X-ray diffraction (PXRD) patterns of the acid- and base-treated samples of TUB41 retain their structures between pH 1 and pH 11 after 2 h, highlighting its stability in acidic and basic environments for this period of time. The sample treated at pH 13 starts to decompose, although it retains some of its original PXRD pattern. At this pH, it predominantly converts into CuOH species, indicating relatively slow decomposition. In addition, TUB41 was synthesized in Parr acid digestion reaction vessels in distilled water at pH 1.5 (pH 2.5 after the reaction) and 120 °C for 48 h, which also points to the intrinsic chemical stability of TUB41 in an acidic environment. As shown in Figure 3, the SEM images reveal that the crystals largely retain their morphology after 2 years of repeated adsorption experiments and storage under room temperature and ambient humidity conditions.

Thermal Stability of TUB41

To understand the thermal behavior of TUB41, we initially performed PXRD of samples that were heated up to 300 °C for 1 h periods, and collected the PXRD data after cooling them to room temperature (Figure 2b). Phosphonic acids condense at high temperatures to make P—O—P bonds, potentially leading to a crystalline metal polymeric framework at ca. 300 °C.[36] This is suggested by the MS-TGA results, which show that water evaporation gradually occurs above ca. 250 °C (see Figure 5 and Section 4).

To gain insight into the stability of the material after several years of cycling, we performed in situ variable temperature powder X-ray diffraction (VT-PXRD) on 2 year old crystals, which were repeatedly used in CO_2 and water vapor adsorption experiments (~20 cycles in total) and heated up to 330 °C. As can be seen in Figure 4a, the PXRD pattern remains very similar to the original phase until 330 °C, although some minor phase transformations can be observed. The phase transformation and thermal stability of the compound is better observed in contour plots of

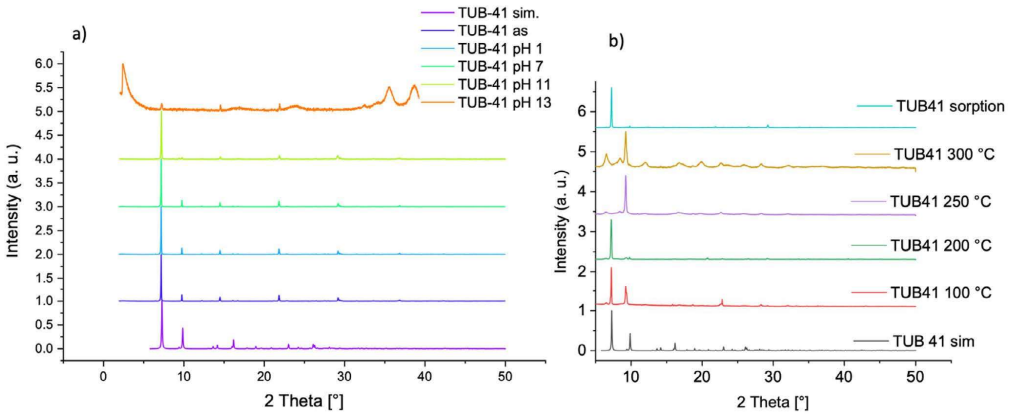

Figure 2. PXRD (Cu K_α radiation) of TUB41 at a) different pH's and b) different temperatures after adsorption experiments.

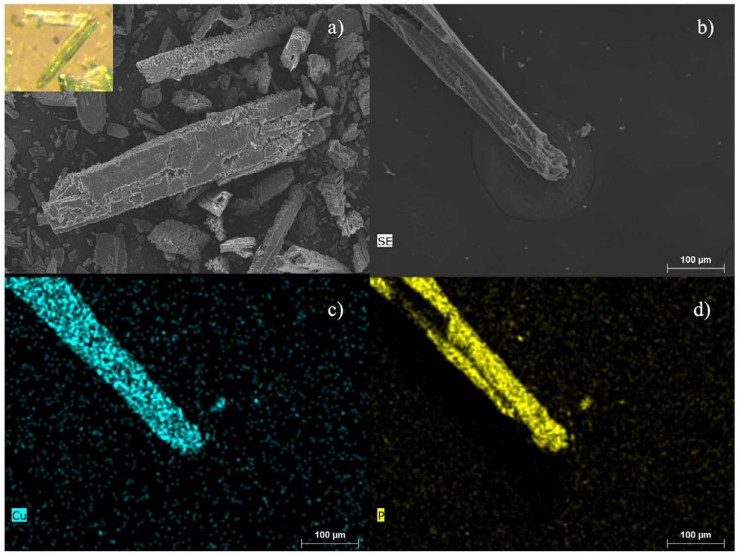

Figure 3. SEM pictures of TUB41 after adsorption experiments. Crystals of TUB41 are shown in panels a) and b), and the corresponding elemental mappings for Cu and P are shown in panels c) and d), respectively.

TUB41 in Figure 4b, with the dark areas showing crystalline, consistent Bragg reflections with varying intensity continuing until 330 °C. The most interesting reflex is observed at $2\theta = 7.2°$, which splits into two peaks above 120 °C and reverts to one peak above 250 °C, demonstrating the strongest phase transformation. Between 14° and 25°, many smaller but observable transformations occur. At $2\theta = 14.4°$, 20.5°, 21.8°, and 22.4°, reflections are sharpening from temperatures above 80 °C, demonstrating higher crystallinity of the sample until 330 °C (see Figure 4b). We previously summarized the conformational changes in flexible rod-shaped SBUs observed in phosphonate MOFs.[16] The observed phase transitions might be a result of the reversible conformational changes in the Cu–O–P–O–Cu–O–P–O rings up to 250 °C. Due to the observed condensation above 250 °C, the crystal data becomes more stable with the formation of new peaks and retains the major patterns observed at low temperatures (see Figures 2, 4 and 5). As depicted in Figure 1b, the

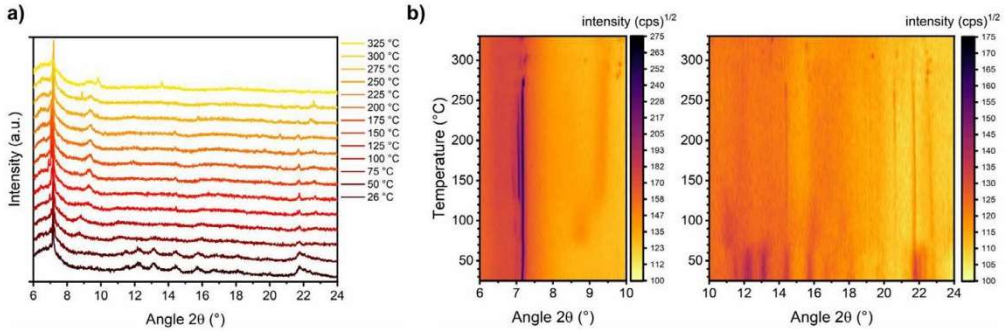

Figure 4. a) In situ VT-PXRD (Cu K_α radiation) in a staggered plot until 330 °C, showing no drastic changes in the patterns over a long 2θ range. b) Contour plots of TUB41 from 25–330 °C using square-root scaling of the intensity, allowing us to better follow changes in crystallinity and phase transformations. The dark areas correlate 2θ values to observed high intensity of reflections.

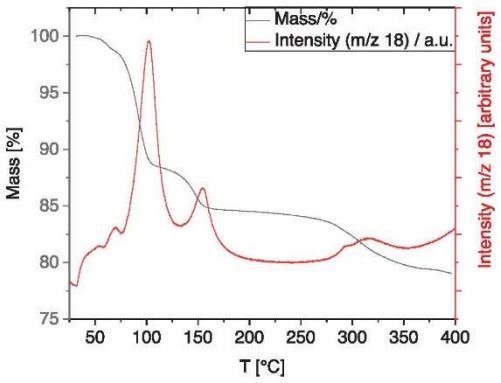

Figure 5. MS-TGA measurements in synthetic air for TUB41.

rod-shaped SBU of TUB41 has repeating hydrogen bonds between the mono-deprotonated phosphonate-based hydrogen atom and Cu(II)-coordinated phosphonate oxygen atoms. The thermal flexibility of TUB41 might be originating from the breaking and reforming of the hydrogen bonds leading to multiple SBU conformations and phase transitions at different temperatures.

MS-Coupled Thermogravimetric Analysis

We performed MS-coupled thermogravimetric analysis (MS-TGA) to understand the thermal behavior of TUB41 (see Supporting Information for instrumental details). As depicted in Figure 5, the MS-TGA results show two distinct steps of mass loss, occurring at around 100 °C (11.5 %) and around 150 °C (3.5%), which is identified as loss of water. After ca. 250 °C, decomposition is observed, which is accompanied by a loss of water, probably due to the condensation of phosphonic acid groups.[36,43] This transition is also confirmed by the in situ temperature variable PXRD showing peaks after 200 °C, and more intensely after keeping the TUB41 crystals at 250 and 300 °C for a longer period of time (see Figure 2b). At 400 °C, still more than 75 mass% of the sample remains, indicating appreciable thermal stability of the organic linker molecules. However, the structure has potentially changed to a less crystalline phase after condensation of the phosphonic acids, according to the PXRD results above 250 °C (see Figures 2b and 4).

Adsorption Studies

To characterize the surface area and porosity of TUB41, nitrogen and argon adsorption isotherms were measured at 77 K. As seen in Figure S4, they show very low adsorption and yield a BET surface area of only ca. 4 $m^2\ g^{-1}$ and a total pore volume of 0.04 $cm^3\ g^{-1}$, consistent with low porosity. In addition, nitrogen adsorption isotherms measured at 298 and 313 K (see Figure S4) also show very low adsorption, indicating that TUB41's pores continue to exclude gases with larger kinetic diameters even at elevated temperatures.

In contrast, the CO_2 adsorption isotherms (Figure 6a) show a higher adsorption and distinct hysteresis over the whole pressure range, indicating an attractive interaction between the adsorbent and adsorbate. The hysteresis looks closest to type H4,[44,45] further strengthening the hypothesis of small, narrow pores with a polar internal surface. BET calculations based on the CO_2 adsorption isotherm at 273 K yield a surface area of 60 $m^2\ g^{-1}$ and a total pore volume of 0.019 $cm^3\ g^{-1}$, consistent with low porosity. At low loadings (0.01 mmol g^{-1} CO_2), the enthalpy of adsorption was estimated to be −41 kJ mol^{-1}, indicative of a strong attractive interaction between CO_2 and the framework. (The details for calculating the enthalpy of adsorption, including model fitting and application of the Clausius–Clapeyron equation, are provided in the Supporting Information). This suggests the presence of high-affinity binding regions within the pores, making

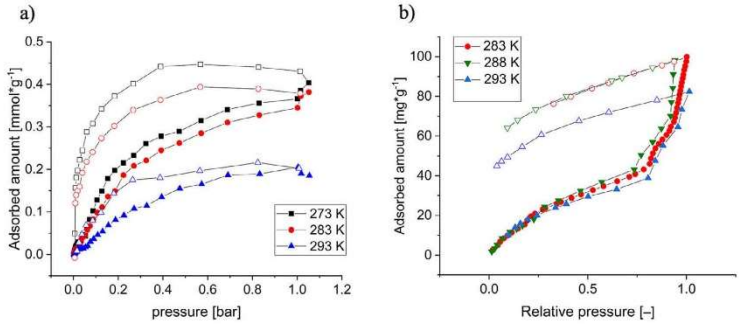

Figure 6. a) CO_2 adsorption isotherms at different temperatures (filled symbols–adsorption, empty symbols–desorption). b) Water vapor adsorption isotherms at different temperatures (filled symbols–adsorption, empty symbols–desorption).

TUB41 suitable for selective CO_2 capture in low-pressure environments. For comparison, TUB41's enthalpy of adsorption is comparable to that of CALF-20, which is −39 kJ mol^{-1}.

Water vapor isotherms measured at 283, 288, and 293 K exhibit a gradual uptake in the low-pressure region, followed by a sharp rise at ~0.8 relative pressure, a step at ~0.9, and another sharp rise at higher relative pressures (Figure 6b). This behavior matches a combination of type IV and type II isotherms at lower (up to ~0.8) and higher relative pressure, respectively. For water vapor sorption, type IV and type II isotherms are indicative of a hydrophilic material.[46] Importantly, the water uptake until ~0.8 relative pressure of 0.04 g g^{-1} matches very well with the pore volume of 0.04 cm^3 g^{-1} from N_2 gas sorption at 77 K (vide supra), thereby supporting the micropore filling with ("liquid") water (at a density of ~1 g cm^{-3}) until this relative pressure. Subsequently, at relative pressures between 0.7 and 0.8, inter-particle condensation in meso- and macro-pores begins, leading to a strong increase in the amount of adsorbed water in line with the type II branch starting at this relative pressure. The desorption measurements show a pronounced hysteresis, closest to type H2 behavior.[43,45] The incomplete desorption observed at all temperatures is indicative of strong interactions between the water molecules and polar groups within the pores. Since the same sample was used for all measurements, it was found that reactivation at 80 °C under vacuum for 2 h was sufficient to empty the pores. The total water uptake exceeds that of CO_2 and is much higher than that of nitrogen, underscoring the selectivity of the pores for molecules with sufficiently small kinetic diameters at elevated temperatures.

The enthalpy of adsorption of water vapor was estimated using the same procedure as for CO_2, focusing on the low-pressure region prior to the onset of condensation. At a loading of 0.7 mmol g^{-1} (corresponding to a pressure of 2×10^{-3} bar), the calculated enthalpy of adsorption is −38 kJ mol^{-1}. This higher loading, relative to the CO_2 case, was selected due to the lower accuracy in the low-pressure region of the water sorption and the available measurement points (Figure S2). The enthalpy of adsorption increases with increasing pressure (Figure S3), probably due to the formation of hydrogen bonds between adsorbed water molecules.

TUB41 exhibits a higher mass of water vapor adsorption (0.04 g g^{-1}) compared to CO_2 adsorption (0.017 g g^{-1}), which might be due to the smaller kinetic diameter of water molecules (2.65 Å) compared to CO_2 (3.3 Å) in the gaseous phase. Another reason for the higher water adsorption might be due to the condensation of water molecules between the TUB41 crystals, which usually happens at higher relative pressures. It should be noted that other MOFs, such as CALF-20, which capture CO_2 via physisorption, also adsorb a higher amount of H_2O compared to CO_2.[15] As discussed below, our MD simulations suggest that this phenomenon may be due to the formation of hydrogen bonds between water molecules, leading to more densely packed water molecules in the pores. On the other hand, gases like CO_2 interact weakly with each other via noncovalent interactions.

The total number of MOFs that are more selective for CO_2 in the presence of water vapor is very limited in the literature, as MOFs usually have higher affinity for water vapor due to the presence of hydrophilic moieties.[15,22] Although the amount of adsorbed CO_2 is limited in TUB41 due to its small surface area, it still has a unique place among MOFs with its narrow and selective pores limiting competition with gases having larger kinetic diameters, e. g., nitrogen (3.64 Å) under cryogenic conditions and methane (3.8 Å). Moreover, the naphthalene moieties impart a high hydrophobicity to the pores.

Altogether, the adsorption measurements confirm the existence of very small pores, which are not accessible to nitrogen (under both cryogenic and higher measurement temperatures) and argon (under the cryogenic measurement temperatures) due to their larger kinetic diameter (see Figure S4). Argon has a slightly larger kinetic diameter of 3.4 Å compared to CO_2 which has a kinetic diameter of 3.3 Å.[47] Therefore, TUB41 excludes gases with kinetic diameters exceeding approximately 3.3–3.4 Å.

Molecular Dynamics Studies

We performed molecular dynamics (MD) simulations on several TUB41 systems (12 × 4 × 4 supercells) containing varying concentrations of H_2O and CO_2, employing the flexible UFF4MOF force field for TUB41, rigid TIP4P model for water, and TraPPE model for CO_2. Specifically, four systems with different H_2O concentrations (containing 10, 30, 100, and 300 water molecules) and three systems with different CO_2 concentrations (containing 10, 30, and 100 CO_2 molecules) were constructed to investigate the distribution, adsorption, and diffusion properties of H_2O and CO_2 in TUB41. The full simulation details are provided in the Supporting Information.

To visualize the distribution of CO_2 and H_2O molecules within the pores of TUB41, atomic trajectory overlay maps were generated for each system. Specifically, the positions of all atoms in the supercell were saved at every 1000 frames of a trajectory. Then, for each unit cell, the positions of all atoms were re-calculated relative to a common reference point in the unit cell, and these relative positions were projected onto a two-dimensional plane perpendicular to a given axis. Finally, the atomic trajectory overlay map is generated by superimposing the projections for each unit cell in the supercell onto each other. An example of a trajectory overlay map for the system containing 30 H_2O and 30 CO_2 molecules (projected onto a plane perpendicular to the x-axis, i.e., channel direction) is shown in Figure 7. Atomic trajectory overlay maps for the remaining systems and projections are provided in the Supporting Information.

After analyzing the trajectory overlay maps for all systems and projections, several interesting conclusions can be drawn: the orientations and positions of the H_2O and CO_2 molecules are significantly constrained by the narrow channels, resulting in ordered arrangements. The H_2O molecules preferentially localize near the SBUs, whereas the CO_2 molecules predominantly occupy the centers of the channels (as seen in Figure 7). This distribution pattern is observed across all concentrations, suggesting distinct adsorption mechanisms for H_2O and CO_2 in the TUB41 framework.

To further investigate the distribution and interactions of the CO_2 and H_2O molecules with the TUB41 framework, radial distribution functions (RDFs) for select atomic pairs were calculated. The RDF for a pair of atoms a and b, $g_{ab}(r)$, is defined as[40,41]

$$g_{ab}(r) = (N_a N_b)^{-1} \sum_{i=1}^{N_a} \sum_{i=1}^{N_b} \langle \delta (|\boldsymbol{r}_i - \boldsymbol{r}_j| - r) \rangle \quad (1)$$

where r is the distance from atom a, N_a and N_b are the number of a and b atoms, respectively, $\boldsymbol{r}_i$ and $\boldsymbol{r}_j$ are the position vectors of particles i and j, respectively, and δ is the Dirac delta function.

Figure 8 presents RDFs between atoms in CO_2/H_2O and atoms in the TUB41 framework for all systems studied. The O (H_2O)–O (framework) RDF possesses a distinct peak at around 2.5 Å, indicating the presence of strong hydrogen bonding (see Figure 8a). In contrast, no significant peaks below 3.5 Å were observed between O (H_2O) atoms and other framework atoms (see Figure S29). The H (H_2O)–O (framework) RDF possesses two distinct peaks at around 1.5 and 2.7 Å, further supporting the presence of hydrogen bonding (see Figure 8b). Figure 8c shows two close peaks between 2.5–3.5 Å due to significant nonbonding interactions between the two O (CO_2) atoms and multiple H (framework) atoms; similarly, Figure 8d shows a single peak around 3 Å due to significant nonbonding interactions between the C (CO_2) atom and multiple H (framework) atoms. This explains the ordered arrangement of CO_2 molecules in the channel centers observed in Figure 7b. (For more RDF plots, the reader is referred to Figure S29 of the Supplementary Information.)

We next quantified the average number of hydrogen bonds between a H_2O molecule and the MOF framework for the water-containing systems.[42] Hydrogen bonds were assigned according to the following criteria: (1) donor–acceptor distance less than 3.0 Å, and (2) donor–hydrogen–acceptor angle greater than 150°. The results are shown in Figure 9. Across all investigated systems, each water molecule forms, on average, about one hydrogen bond with the MOF framework, consistent with the experimental hydration results. Based on the RDF results, this bond is a strong hydrogen bond. Additionally, no hydrogen bonds were identified between CO_2 molecules and the MOF framework (result not shown). We also analyzed the average number of hydrogen bonds between H_2O molecules for the water-containing systems. For the 30- and 100-water systems, this number is essentially zero; however, for the 300-water system, there are ~0.065 bonds, a small but significant number (see Figure S30). This is because, at higher concentrations, the binding sites of the framework become saturated, causing the additional water molecules to reside in the center of the channel where they have more opportunity to hydrogen bond with each other. This phenomenon is further supported by the atomic trajectory overlay map of the 300-water system (see Figure S28).

The mean-squared displacements (MSDs) of H_2O and CO_2 were computed according to:[43,44]

$$MSD(t) = \frac{1}{N} \sum_{i=1}^{N} |r_i - r_i(t)|^2 \quad (2)$$

where N is the number of particles averaged over and r_i is the position of particle i. They were calculated based on 5 ns NVT trajectories, started from the final frames of the previous production runs. The MSD results for the systems containing 30 H_2O and 30 CO_2 molecules are shown in Figure 10. Both the H_2O and CO_2 MSDs exhibit similar trends. Initially, the MSDs increase steadily up to about 0.3 ns. Beyond 0.3 ns, both MSDs cease to grow further and instead fluctuate around equilibrium values. The equilibrium MSD value is approximately 2.0 Å^2 for H_2O and 3.2 Å^2 for CO_2. These values are exceptionally small, indicating that both H_2O and CO_2 molecules are tightly confined in all three spatial dimensions near their equilibrium positions within the pores. This confinement arises from a combination of strong guest–host interactions and the ultramicroporous character

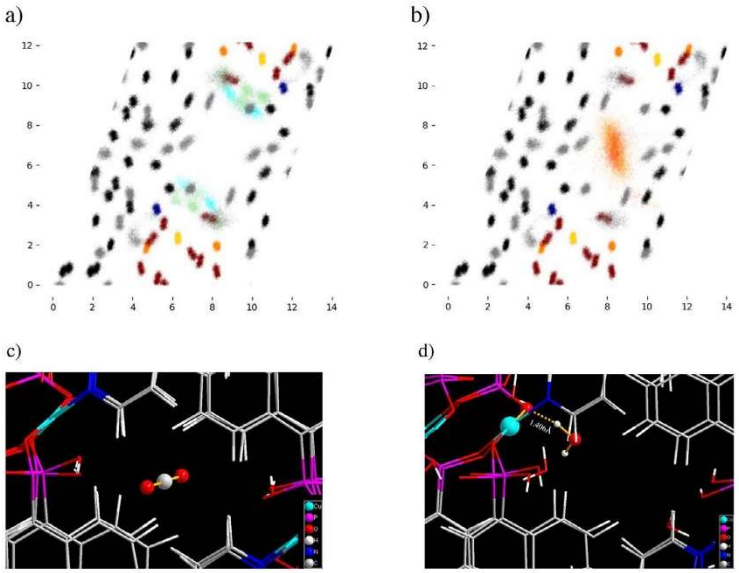

Figure 7. Atomic trajectory overlay maps of a TUB41 unit cell containing a) 30 H_2O molecules and b) 30 CO_2 molecules. The maps are projections onto a plane that is perpendicular to the channel direction. Cyan and green represent the oxygen and hydrogen atoms of H_2O, respectively; red and orange represent the carbon and oxygen atoms of CO_2, respectively; gold, dark blue, dark orange, dark red, black, and gray represent copper, nitrogen, phosphorus, oxygen, carbon, and hydrogen atoms, respectively, in the MOF framework. The *x* and *y* axes of the maps represent position, expressed in Ångströms (Å). A representative snapshot from the MD trajectory showing c) a typical position of a CO_2 molecule within a pore, and d) a typical hydrogen bond at the edge of a pore, formed between a H_2O molecule and an oxygen atom in the MOF's SBU.

of TUB41. For comparison, in another MOF currently under investigation, the MSDs of H_2O and CO_2 reach up to 1000 $Å^2$ within 5 ns. Given both the low MSD values observed in TUB41 and the small difference between them, it is not possible to draw meaningful conclusions about any preferential kinetic behavior between the two gases in this system.

In addition to MD simulations, we employed the random insertion algorithm in LAMMPS to estimate the maximum adsorption capacities of CO_2 and H_2O in the TUB41 supercell. For each gas, 1000 insertion attempts were made, with up to 10 000 placement attempts per molecule. If a suitable position is not found after 10 000 attempts, the algorithm proceeds to the next molecule. A minimum initial distance of 1.6 Å between all atoms was enforced to ensure stability, as values below this threshold resulted in unstable simulations. Parallel simulations were conducted using three different random number seeds. The number of CO_2 molecules successfully inserted into the TUB41 supercell was 254, 244, and 242, with an average of 247, while for H_2O, the counts were 762, 766, and 766, averaging 765. Thus, the calculated maximum adsorption capacities are 0.084 g g^{-1} for H_2O and 0.066 g g^{-1} for CO_2, which are consistent with the experimental observation that TUB41 possesses a higher mass of water vapor adsorption (0.04 g g^{-1}) compared to CO_2 adsorption (0.017 g g^{-1}).

Overall, the MD simulation results suggest that the pores of TUB41, which are lined predominantly with hydrophobic groups and only at select sites with hydrophilic phosphonate oxygen atoms from the SBUs, promote spatial separation between H_2O and CO_2, potentially enabling coadsorption while minimizing competitive interactions.

Optical Properties

Copper phosphonate MOFs, such as TUB1, TUB40, and TUB75 (sister compounds of TUB41), and other phosphonate MOFs are known for their semiconducting properties.[33,37,38,48] Thus, we measured the diffuse reflectance spectrum of TUB41 to estimate its optical band gap. Based on the Tauc plots generated from the diffuse reflectance spectra (see Figures S21a and S21b), we extracted an indirect band gap of 2.7 eV and direct band gap of 3.0 eV (see Supporting Information for experimental details).[49,50] The band centered at around 1.7 eV is likely due to a localized $3d^9 \leftarrow 3d^9$ transition of the Cu(II) centers ($^2E \leftarrow ^2T_2$ in an approximately tetrahedral field). TUB41 has a very similar SBU compared to our previously reported MOF TUB1. The SBUs in both TUB1 and TUB41 have the same order of vertex-connected [Cu–O–P–O–Cu–O–P–O] eight-membered rings resulting in a rod-shaped SBU (see Figure 1b).[48] The

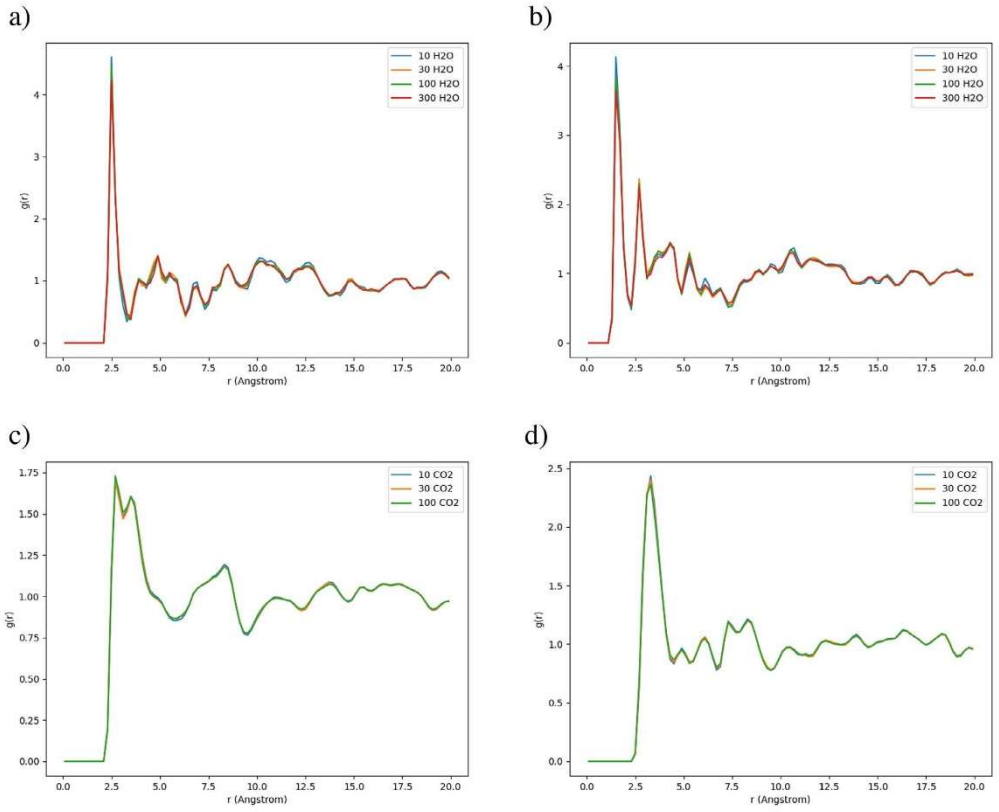

Figure 8. RDFs between atoms in CO_2/ H_2O and atoms in the TUB41 framework for all systems. a) O (H_2O)–O (framework). b) H (H_2O)–O (framework). c) O (CO_2)–H (framework). d) C (CO_2)–H (framework).

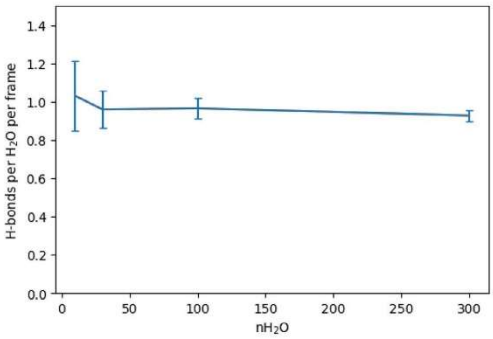

Figure 9. Average number of hydrogen bonds between a H_2O molecule and the MOF framework for the water-containing systems, normalized by both the number of trajectory frames and the number of H_2O molecules.

major difference between the SBUs of TUB41 and TUB1 is the first copper atom (Cu1) in TUB1, which is coordinated in a square-planar fashion, while the second copper atom (Cu2) is coordinated in a square-pyramidal fashion. In TUB41, all copper atoms show a square–pyramidal coordination sphere. Similar to TUB41, our previously published MOF TUB1 possesses an indirect band gap of 2.4 eV and a direct band gap of 2.7 eV, which was also confirmed by DOS calculations.[48] The slightly narrower band gap observed in TUB1 might be due to the presence of square planar coordinated Cu(II) ions as indicated by the calculations in the previous work. The indirect and direct band gaps of TUB41 are within the visible range, highlighting the potential of TUB41 in photocatalysis applications.

Conclusions

TUB41 stands out among MOFs for its narrow, selective pores, which effectively exclude gases with kinetic diameters

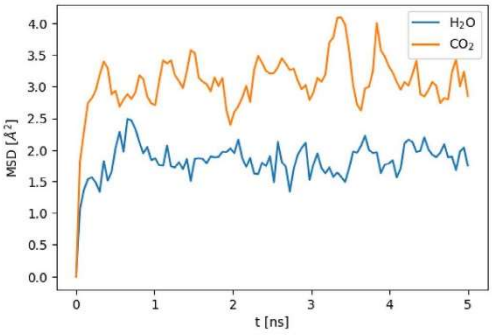

Figure 10. MSDs of H_2O and CO_2 in the TUB41 systems containing 30 H_2O and 30 CO_2 molecules, respectively.

larger than 3.3 Å, and for its remarkable stability, maintaining structural integrity over a two-year period. It remains stable for over a month at pH 2.5 and for at least 2 h across a broad pH range from 1 to 11. The crystals also retain their stability after repeated adsorption experiments and activation at 80 °C under vacuum. Compared to conventional MOFs, which are often hydrolyzed by water vapor, TUB41 shows superior chemical stability, particularly in acidic and basic environments within the pH 1–11 range. This exceptional stability enhances its suitability for industrial applications, especially in membrane-based coseparation of CO_2 and H_2O from other gases. In contrast, typical MOFs with metal-carboxylate SBUs, such as UiO-66, have relatively short shelf lives of approximately 2 months under ambient conditions.

A major challenge in CO_2 capture under humid conditions is the typically stronger affinity of MOFs for water, largely due to the presence of hydrophilic metal-binding groups. In TUB41, the presence of naphthalene moieties lining the pores imparts a predominantly hydrophobic character to the pores, creating a more favorable environment for CO_2 adsorption. The hydrophilic oxygen atoms of the phosphonate groups cover only a small fraction of the inner surface area (Figure 1a,c), which is sufficient to enable water adsorption while preserving the overall hydrophobic character of the pores. The slit-shaped channels along the *a* axis, with a cross-section of approximately 4 × 2 Å^2, provide a confined space well-suited for the selective adsorption of gases with small kinetic diameters. Additionally, the rod-shaped SBU imparts TUB41 with reversible phase transitions observable at different temperatures. In situ temperature-variable PXRD combined with MS-TGA points to the condensation of phosphonate groups, leading to the release of additional water molecules at elevated temperatures.

The MD simulations reveal distinct adsorption mechanisms for H_2O and CO_2 within TUB41. H_2O preferentially localizes near the SBUs through strong hydrogen-bonding interactions, while CO_2 predominantly occupies the central regions of the channels, driven by Coulombic and van der Waals forces. The RDFs and hydrogen-bond analysis confirm the specificity and strength of these interactions. The MSD results further demonstrate that both H_2O and CO_2 are spatially constrained within the pores, highlighting their strong affinity for the MOF framework. Despite the higher loading capacity of H_2O and its strong hydrogen-bonding interactions, which may impact CO_2 uptake, the largely hydrophobic nature of TUB41's pores and the spatial separation between CO_2 (in the center of the channels) and H_2O (near the SBUs) suggest that competitive adsorption could be partially mitigated. These characteristics enable the selective adsorption of CO_2 in humid environments, highlighting TUB41's potential for gas separation applications.

In summary, TUB41 represents a significant step forward in the design of robust MOFs, combining exceptional long-term thermal and chemical stability with selective gas adsorption and a visible-range band gap. Its unique combination of properties–including over 2 years of structural stability, resistance to harsh chemical environments, and molecular-level selectivity for CO_2 and water vapor–positions it as a promising candidate for applications such as photocatalytic water splitting, CO_2 reduction, and industrial gas separation. The development of phosphonate-based MOFs like TUB41, featuring insoluble SBUs and resilience in concentrated acids and bases, paves the way for the next generation of MOFs capable of operating in demanding aqueous and chemical environments.

Supporting Information

The Supporting Information contains details of the synthesis, gas and water adsorption, MD simulations, and optical spectroscopy.

Author Contributions

R.O. performed the gas sorption studies and optical measurements, and wrote the corresponding sections. M.F. resynthesized TUB41, developed a new method for the linker synthesis, and performed the stability experiments and took SEM pictures. Y.Z. set up and performed the MD simulations, generated the corresponding figures, and wrote the initial drafts of the computational parts of the manuscript. A.S. performed the N_2 and Ar adsorption measurements, A.K. performed the in situ temperature variable PXRD measurements and wrote the corresponding section, M.S. supervised the optical measurements, wrote the corresponding section, and edited the manuscript. C.J. supervised and interpreted the gas adsorption work, created the crystallographic figures, and edited the manuscript. G.H. supervised the work of Y.Z., provided critical feedback on several experimental sections of the manuscript, revised the computational parts of the manuscript, and edited the entire manuscript. G.Y. created the hypothesis, supervised the work of M.F. and R.O., and wrote the majority of the abstract, introduction, conclusion sections, and contributed experimental sections of the manuscript.

Acknowledgements

G.Y. would like to thank DFG for fundings DFG YU 267/2–1 and DFG YU 267/9–1. M.S. acknowledges funding from a materials cost allowance of the Fonds der Chemischen Industrie e.V. and a scholarship of the "Young College" of the North-Rhine Westphalian Academy of Sciences, Humanities, and the Arts. The authors would like to thank Microtrac Retsch GmbH to perform the N_2 and Ar adsorption work. G.H. acknowledges funding from the Natural Sciences and Engineering Research Council of Canada (NSERC). The MD simulations were enabled in part by support by the Digital Research Alliance of Canada (alliancecan.ca).

Open access funding enabled and organized by Projekt DEAL.

Conflict of Interests

The authors declare no conflict of interest.

Data Availability Statement

The data that support the findings of this study are available in the Supporting Information of this article.

Keywords: Chemically & thermally stable MOFs · CO_2 capture · Gas separation

[1] H. Furukawa, K. E. Cordova, M. O'Keeffe, O. M. Yaghi, *Science* **2013**, *341*, 1230444.
[2] O. M. Yaghi, M. J. Kalmutzki, C. S. Diercks, *Introduction to* Reticular Chemistry: Metal-Organic Frameworks and Covalent Organic Frameworks, Wiley, Hoboken, NJ **2019**.
[3] T. H. Y. Beglau, M. N. A. Fetzer, I. Boldog, T. Heinen, M. Suta, C. Janiak, G. Yücesan, *Chem. Eur. J.* **2024**, *30*, e202302765.
[4] P. Tholen, L. Wagner, J. G. A. Ruthes, K. Siemensmeyer, T. H. Y. Beglau, D. Muth, Y. Zorlu, M. Okutan, J. C. Goldschmidt, C. Janiak, V. Presser, Ö. Yavuzçetin, G. Yücesan, *Small* **2023**, *19*, 2304057.
[5] P. Horcajada, R. Gref, T. Baati, P. K. Allan, G. Maurin, P. Couvreur, G. Ferey, R. E. Morris, C. Serre, *Chem. Rev.* **2012**, *112*, 1232–1268.
[6] S. Rojas, A. Arenas-Vivo, P. Horcajada, *Coord. Chem. Rev.* **2019**, *388*, 202–226.
[7] M. W. Ambrogio, C. R. Thomas, Y. L. Zhao, J. I. Zink, J. F. Stoddart, *Acc. Chem. Res.* **2011**, *44*, 903–913.
[8] K. J. Hartlieb, D. P. Ferris, J. M. Holcroft, I. Kandela, C. L. Stern, M. S. Nassar, Y. Y. Botros, J. F. Stoddart, *Mol. Pharmaceutics* **2017**, *14*, 1831.
[9] R. A. Smaldone, R. S. Forgan, H. Furukawa, J. J. Gassensmith, A. M. Z. Slawin, O. M. Yaghi, J. F. Stoddart, *Angew. Chem. Int. Ed.* **2010**, *49*, 8630–8634.
[10] A. J. Howarth, Y. Liu, P. Li, Z. Li, T. C. Wang, J. T. Hupp, O. K. Farha, *Nat. Rev. Mater.* **2016**, *1*, 15018.
[11] M. Ding, X. Cai, H.-L. Jiang, *Chem. Sci.* **2019**, *10*, 10209–10230.
[12] C. Healy, K. M. Patil, B. H. Wilson, L. Hermanspahn, N. C. Harvey-Reid, B. I. Howard, C. Kleinjan, J. Kolien, F. Payet, S. G. Telfer, P. E. Kruger, T. D. Bennett, *Coord. Chem. Rev.* **2020**, *419*, 213388.
[13] M. Ding, X. Cai, H. L. Jiang, *Chem. Sci.* **2019**, *10*, 10209.
[14] D. Bu˙žek, S. Adamec, K. Lang, J. Demel, *Inorg. Chem. Front.* **2021**, *8*, 720.
[15] J.-B. Lin, T. T. Nguyen Tai, R. Vaidhyanathan, J. Burner, M. Taylor Jared, H. Durekova, F. Akhtar, K. Mah Roger, O. Ghaffari-Nik, S. Marx, N. Fylstra, S. Iremonger Simon, W. Dawson Karl, P. Sarkar, P. Hovington, A. Rajendran, K. Woo Tom, K. H. Shimizu George, *Science* **2021**, *374*, 1464–1469.
[16] P. Tholen, Y. Zorlu, J. Beckmann, G. Yücesan, *Eur. J. Inorg. Chem.* **2020**, *2020*, 1542–1554.
[17] K. J. Gagnon, H. P. Perry, A. Clearfield, *Chem. Rev.* **2012**, *112*, 1034–1054.
[18] C. M. Sevrain, M. Berchel, H. Couthon, P.-A. Jaffrès, *Beilstein J. Org. Chem.* **2017**, *13*, 2186–2213.
[19] R. J. Motekaitis, I. Murase, A. E. Martell, *Inorg. Chem.* **1976**, *15*, 2303–2306.
[20] K. D. Demadis, N. Stavgianoudaki, *Metal Phosphonate Chemistry: From Synthesis to Applications*, RSC Publishing, Cambridge, UK **2012**.
[21] H. Deng, C. J. Doonan, H. Furukawa, R. B. Ferreira, J. Towne, C. B. Knobler, B. Wang, O. M. Yaghi, *Science* **2010**, *327*, 846–850.
[22] P. G. Boyd, A. Chidambaram, E. García-Díez, C. P. Ireland, T. D. Daff, R. Bounds, A. Gładysiak, P. Schouwink, S. M. Moosavi, M. M. Maroto-Valer, J. A. Reimer, J. A. R. Navarro, T. K. Woo, S. Garcia, K. C. Stylianou, B. Smit, *Nature* **2019**, *576*, 253–256.
[23] T. M. McDonald, W. R. Lee, J. A. Mason, B. M. Wiers, C. S. Hong, J. R. Long, *J. Am. Chem. Soc.* **2012**, *134*, 7056–7065.
[24] J. H. Choe, H. Kim, H. Yun, M. Kang, S. Park, S. Yu, C. S. Hong, *J. Am. Chem. Soc.* **2024**, *146*, 646–659.
[25] J. H. Choe, H. Kim, H. Yun, J. F. Kurisingal, N. Kim, D. Lee, Y. H. Lee, C. S. Hong, *J. Am. Chem. Soc.* **2024**, *146*, 19337–19349.
[26] O. I.-F. Chen, C.-H. Liu, K. Wang, E. Borrego-Marin, H. Li, A. H. Alawadhi, J. A. R. Navarro, O. M. Yaghi, *J. Am. Chem. Soc.* **2024**, *146*, 2835–2844.
[27] J. F. Kurisingal, J. H. Choe, H. Kim, J. Youn, G. Cheon, C. S. Hong, *Bull. Korean Chem. Soc.* **2024**, *45*, 675–688.
[28] Z. Chen, K. O. Kirlikovali, L. Shi, O. K. Farha, *Mater. Horiz.* **2023**, *10*, 3257–3268.
[29] G. Yücesan, Y. Zorlu, M. Stricker, J. Beckmann, *Coord. Chem. Rev.* **2018**, *369*, 105–122.
[30] R. K. Mah, M. W. Lui, G. K. H. Shimizu, *Inorg. Chem.* **2013**, *52*, 7311–7313.
[31] S.-S. Bao, G. K. H. Shimizu, L.-M. Zheng, *Coord. Chem. Rev.* **2019**, *378*, 577–594.
[32] P. Salcedo-Abraira, S. M. F. Vilela, A. A. Babaryk, M. Cabrero-Antonino, P. Gregorio, F. Salles, S. Navalón, H. García, P. Horcajada, *Nano Res.* **2021**, *14*, 450–457.
[33] C. A. Peeples, D. Kober, F.-J. Schmitt, P. Tholen, K. Siemensmeyer, Q. Halldorson, B. Çoşut, A. Gurlo, A. O. Yazaydin, G. Hanna, G. Yücesan, *Adv. Funct. Mater.* **2021**, *31*, 2007294.
[34] P. Tholen, C. A. Peeples, R. Schaper, C. Bayraktar, T. S. Erkal, M. M. Ayhan, B. Cosut, J. Beckmann, A. O. Yazaydin, M. Wark, G. Hanna, Y. Zorlu, G. Yucesan, *Nat. Commun.* **2020**, *11*, 3180.
[35] P. Tholen, C. A. Peeples, M. M. Ayhan, L. Wagner, H. Thomas, P. Imbrasas, Y. Zorlu, C. Baretzky, S. Reineke, G. Hanna, G. Yücesan, *Small* **2022**, *18*, 2204578.
[36] K. Xu, R. Oestreich, T. Haj Hassani Sohi, M. Lounasvuori, J. G. A. Ruthes, Y. Zorlu, J. Michalski, P. Seiffert, T. Strothmann, P. Tholen, A. Ozgur Yazaydin, M. Suta, V. Presser, T. Petit, C. Janiak, J. Beckmann, J. Schmedt auf der Günne, G. Yücesan, *Nat. Commun.* **2024**, *15*, 7862.
[37] C. Ribeiro, B. Tan, F. Figueira, R. F. Mendes, J. Calbo, G. Valente, P. Escamilla, F. A. A. Paz, J. Rocha, M. Dincă, M. Souto, *J. Am. Chem. Soc.* **2025**, *147*, 63–68.

[38] K. Siemensmeyer, C. A. Peeples, P. Tholen, F. Schmitt, B. Çoşut, G. Hanna, G. Yücesan, *Adv. Mater.* **2020**, *32*, 2000474.
[39] A. Bulut, Y. Zorlu, M. Wörle, A. Çetinkaya, H. Kurt, B. Tam, A. Ö. Yazaydın, J. Beckmann, G. Yücesan, *ChemistrySelect* **2017**, *2*, 7050–7053.
[40] S. Mukherjee, N. Sikdar, D. O'Nolan, D. M. Franz, V. Gascón, A. Kumar, N. Kumar, H. S. Scott, D. G. Madden, P. E. Kruger, B. Space, M. J. Zaworotko, *Sci. Adv.* **2019**, *5*, eaax9171.
[41] D.-X. Xue, Y. Belmabkhout, O. Shekhah, H. Jiang, K. Adil, A. J. Cairns, M. Eddaoudi, *J. Am. Chem. Soc.* **2015**, *137*, 5034–5040.
[42] O. Smirnova, S. Hwang, R. Sajzew, L. Ge, A. Reupert, V. Nozari, S. Savani, C. Chmelik, M. R. Reithofer, L. Wondraczek, J. Kärger, A. Knebel, *Nat. Mater.* **2024**, *23*, 262–270.
[43] L.-R. Guo, S.-S. Bao, Y.-Z. Li, L.-M. Zheng, *Chem. Commun.* **2009**, 2893.
[44] K. S. W. Sing, D. H. Everett, R. A. W. Haul, L. Moscou, R. A. Pierotti, J. Rouquerol, T. Siemieniewska, *Pure Appl. Chem.* **1985**, *57*, 603–619.
[45] M. Thommes, K. Kaneko, A. V. Neimark, J. P. Olivier, F. Rodriguez-Reinoso, J. Rouquerol, K. S. W. Sing, *Pure Appl. Chem.* **2015**, *87*, 1051–1069.
[46] E.-P. Ng, S. Mintova, *Microporous Mesoporous Mater.* **2008**, *114*, 1–26.
[47] S. Matteucci, Y. Yampolskii, B. D. Freeman, I. Pinnau, in *Materials Science of Membranes for Gas and Vapor Separation*, Wiley, Hoboken, NJ **2006**, pp. 1–47.
[48] C. A. Peeples, A. Çetinkaya, P. Tholen, F.-J. Schmitt, Y. Zorlu, K. Bin Yu, O. Yazaydin, J. Beckmann, G. Hanna, G. Yücesan, *Chem. Eur. J.* **2022**, *28*, e202104041.
[49] J. Tauc, *Mater. Res. Bull.* **1968**, *3*, 37.
[50] J. Tauc, R. Grigorovici, A. Vancu, *Phys. Status Solidi B* **1966**, *15*, 627–637.

Manuscript received: June 24, 2025
Revised manuscript received: July 17, 2025
Accepted manuscript online: July 21, 2025
Version of record online: August 23, 2025

Stable Ultramicroporous Metal-Organic Framework with Hydrophilic and Hydrophobic Domains for Selective Gas Adsorption

Robert Oestreich,[1#] Marcus N. A. Fetzer,[1#] Yifei Zhang[6], Andreas Schreiber,[3] Alexander Knebel,[4,5] Markus Suta,[2] Christoph Janiak[1]*, Gabriel Hanna[6]*, and Gündoğ Yücesan[1]*

1. Institute for Inorganic and Structural Chemistry, Heinrich Heine Universität Düsseldorf, Universitätsstr. 1, D-40225 Düsseldorf, Germany.
2. Inorganic Photoactive Materials, Institute for Inorganic and Structural Chemistry, Heinrich Heine University Düsseldorf, Universitätsstr. 1, 40225 Düsseldorf, Germany
3. Microtrac Retsch GmbH, Retsch-Allee 1-5, D-42781 Haan, Germany
4. Otto Schott Institute of Materials Research, Center for Energy and Environmental Chemistry II, Friedrich Schiller University Jena, Lessingstraße 12-14, D-07743 Jena, Germany.
5. Center for Energy and Environmental Chemistry, Friedrich Schiller University Jena, Philosophenweg 7a, D-07743 Jena, Germany
6. Department of Chemistry, University of Alberta, Edmonton, Alberta, Canada

# These authors contributed equally to this work.

Table of Contents

1. General information

Unless otherwise noted, all commercially available compounds were used as provided without further purification. Chemicals used in this study were purchased from Sigma Aldrich, Alfa Aesar, BLDpharm and Carl Roth. Solvents for chromatography were technical grade and distilled prior to use. Analytical thin-layer chromatography (TLC) was performed on Macherey-Nagel silica gel aluminium plates with F-254 indicator, visualized by irradiation with UV light. Column chromatography was performed using silica gel Merck 60 (particle size 0.063 – 0.2 mm). ^{1}H-NMR, ^{13}C-NMR and ^{31}P-NMR were recorded on a Bruker Avance III 300 MHz NMR spectrometer in $CDCl_3$ or DMSO-d_6. Data are reported in the following order: chemical shift (δ) in ppm; multiplicities are indicated brs (broadened singlet), s (singlet), d (doublet), t (triplet), q (quartet), m (multiplet); coupling constants (J) are in Hertz (Hz). Powder X-ray diffraction (PXRD) was performed on a Rigaku Miniflex powder diffractometer in θ/2θ geometry with Cu-Kα radiation (1.54184 Å) and equipped with a rotating low-background silicon sample holder. For thermogravimetric analysis (TGA) of the pure MOF a Netzsch TG 209 F3 Tarsus was used and operated with synthetic air atmosphere and a heating rate of 10 K min^{-1} . TGA curves were baseline corrected with a blank run. Gaseous products were analyzed with a GAM 200 mass spectrometer from InProcess Instruments. Gas and vapor sorption measurements were done on the BELSorp-max II by MicrotracBEL Corporation. The sample was heated to 80°C under vacuum for two hours for activation before every measurement to clear pores of residue gas. Diffuse reflectance and emission spectra were measured on an Edinburgh FLS1000 luminescence spectrometer with 450 W Xe arc lamp, double grating monochromators (Czerny-Turner configuration, blazed at 400 nm in excitation and 500 nm in emission) and a thermoelectrically cooled (-20 °C) PMT980 (Hamamatsu) photomultiplier tube as detection unit. All spectra were acquired at room temperature. Diffuse reflectance was measured using an integrating sphere (diameter 120 mm) setup with the inner surface coated with BenFlect (reflectance >99 % between 350 nm and 2500 nm). All spectra were corrected for the grating efficiency, the lamp intensity, and the wavelength-dispersive sensitivity of the detection unit.

2. Synthesis

Synthesis of tetraethyl naphthalene-1,4-diylbis(phosphonate)

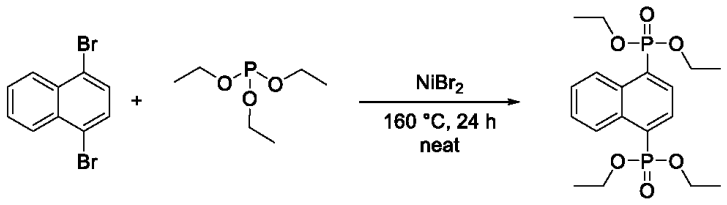

Under a nitrogen flow, 1,4-dibromonaphthalene (5,1 g, 17.8 mmol) was placed in a three-neck round-bottom flask equipped with a stirring bar. The flask was heated to 160 °C to melt the 1,4-dibromonaphthalene. To the melted 1,4-dibromonaphthalene, $NiBr_2$ (0.5 g, 2.2 mmol) was added. Finally, triethyl phosphite (7.8 g, 46.9 mmol) was added dropwise over a period of 7 h. The reaction was stirred at the same temperature for 24 h. The crude product, a dark brown to orange oil, was purified by column chromatography using a mixture of EtOAc and EtOH (9:1 v:v). The product was isolated as a colorless oil with a yield of 3.8 g (9.5 mmol, 53.3 %).

^{1}H NMR (300 MHz, $CDCl_3$) δ 8.63-8.59 (m, 2H), 8.29-8.22 (m, 2H), 7.68-7.64 (m, 2H), 4.27-4.07 (m, 8H), 1.32 (t, *J* = 7.1 Hz, 12H); $^{31}P\{^{1}H\}$ NMR (121 MHz, $CDCl_3$) δ 17.4 (s); $^{13}C\{^{1}H\}$ NMR (75 MHz, $CDCl_3$) δ 132.9-132.4, 131.6 (d, *J* = 3.6 Hz), 129.2 (d, *J* = 3.5 Hz), 127.6, 127.3, 62.5 (d, *J* = 3.0 Hz), 16.3.

Synthesis of naphthalene-1,4-diphosphonic acid (1,4-NDPA-H_4)

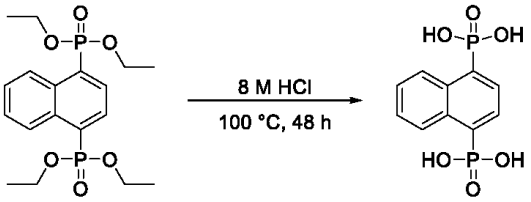

Tetraethyl naphthalene-1,4-diylbis(phosphonate) (3.8 g, 9.5 mmol) was mixed with 100 mL of 8 M hydrochloric acid and refluxed for 24 h. The white precipitate was filtered off and dried at 60 °C under reduced pressure to obtain 2.5 g (yield: 95 %) of pure acid.

^{1}H NMR (300 MHz, DMSO-d_6) δ 8.69-8.65 (m, 2H), 8.08-8.01 (m, 2H), 7.64 (dd, *J*=6.5, 3.4 Hz, 2H); $^{31}P\{^{1}H\}$ NMR (121 MHz, DMSO-d_6) δ 11.0 (s);

$^{13}C\{^{1}H\}$ NMR (75 MHz, DMSO-d_6) δ 135.6 (d), 132.4 (d), 130.3-129.9 (m), 127.8 (s), 126.4 (s).

3. NMR spectra

Tetraethyl naphthalene-1,4-diylbis(phosphonate)

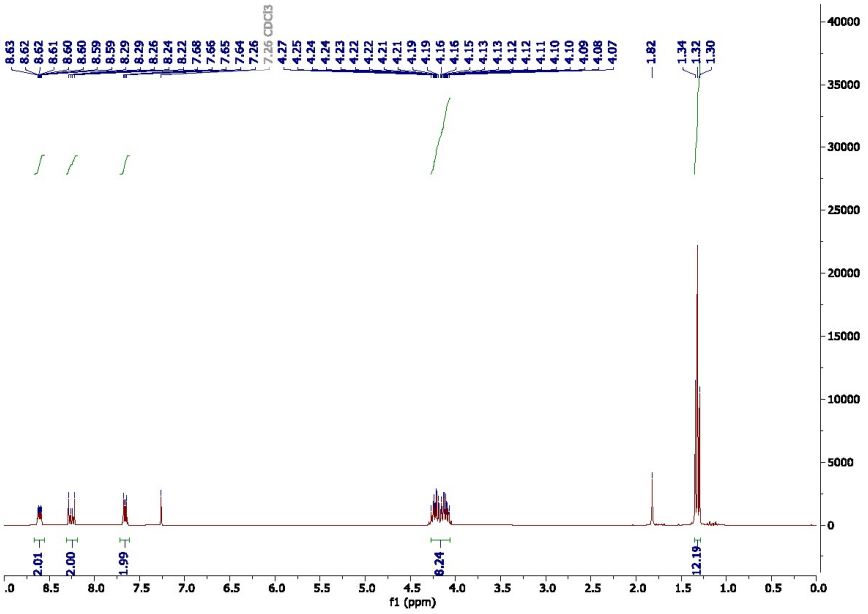

^{1}H NMR (300 MHz, $CDCl_3$)

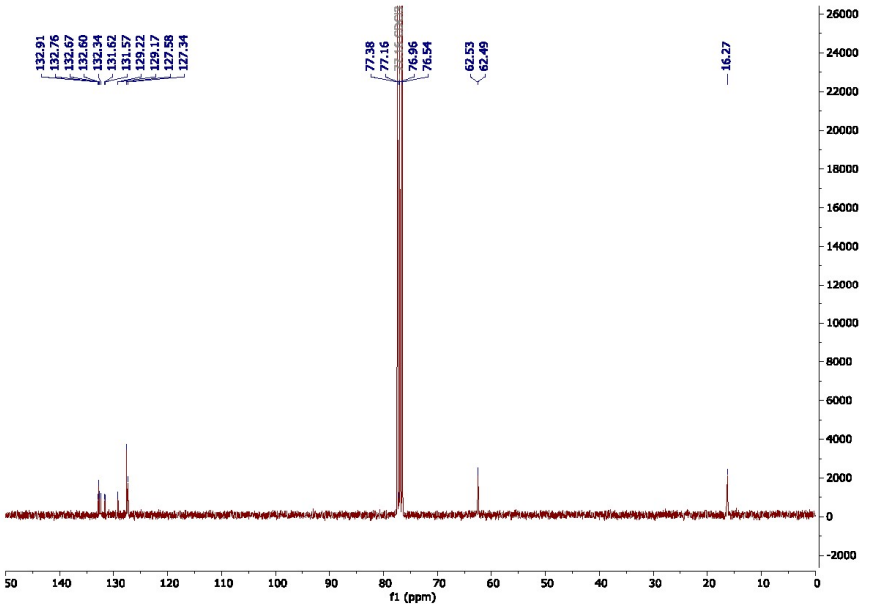

$^{13}C\{^{1}H\}$ NMR (75 MHz, $CDCl_3$)

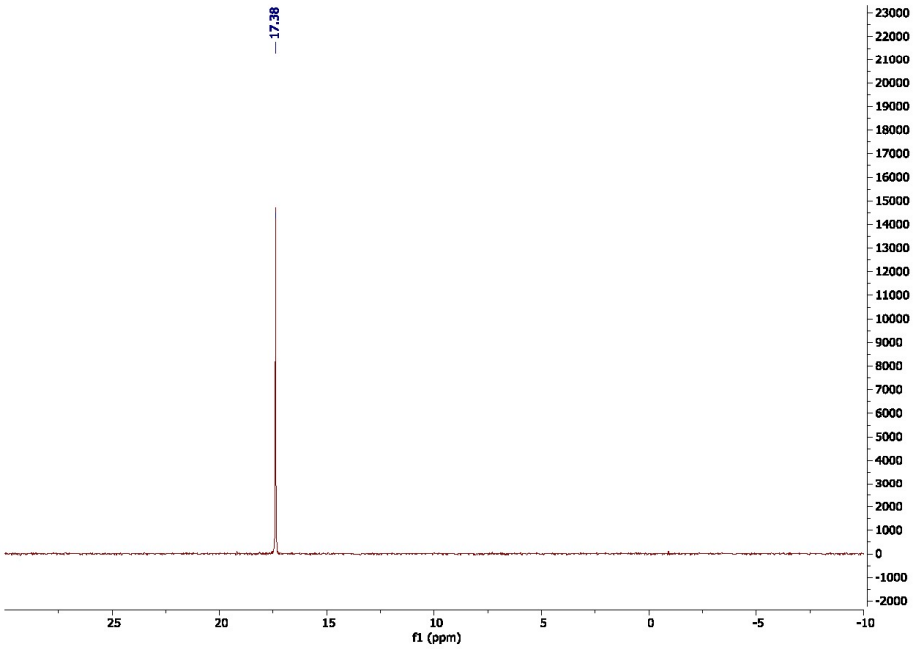

$^{31}P\{^{1}H\}$ NMR (121 MHz, $CDCl_3$)

Naphthalene-1,4-diphosphonic acid (1,4-NDPA-H_4)

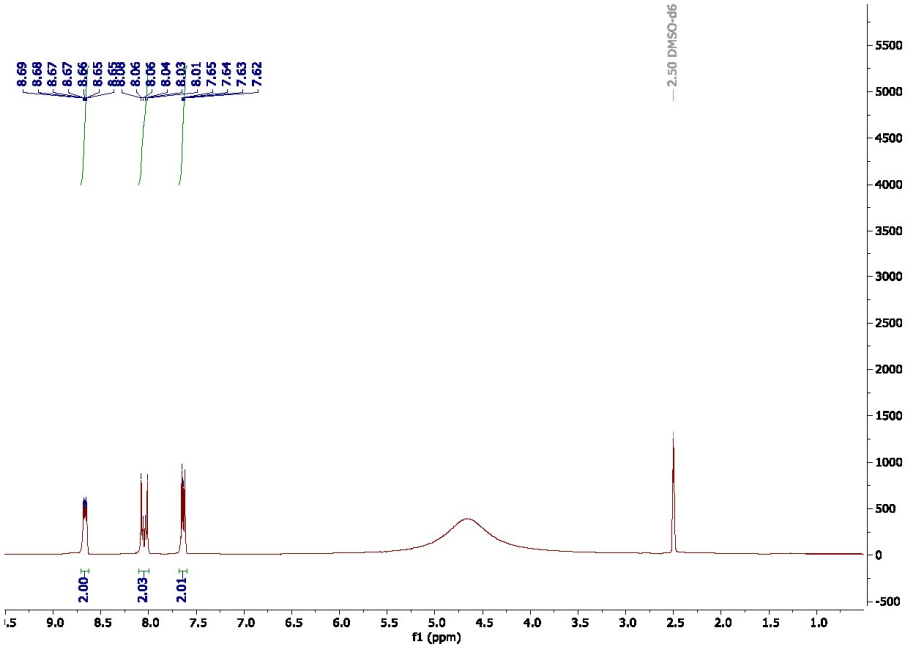

^{1}H NMR (300 MHz, DMSO-d_6)

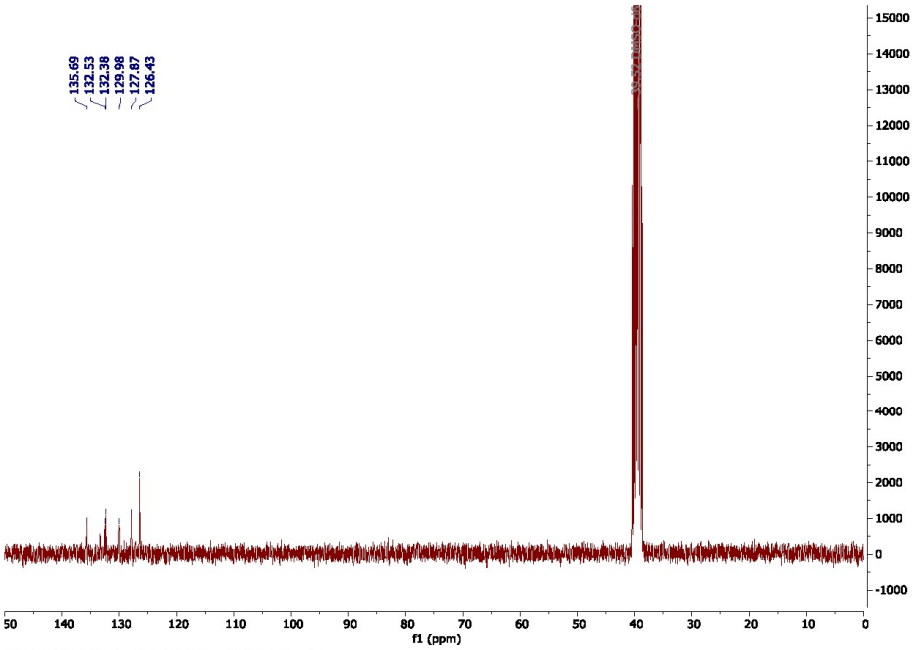

^{13}C{^{1}H} NMR (75 MHz, DMSO-d_6)

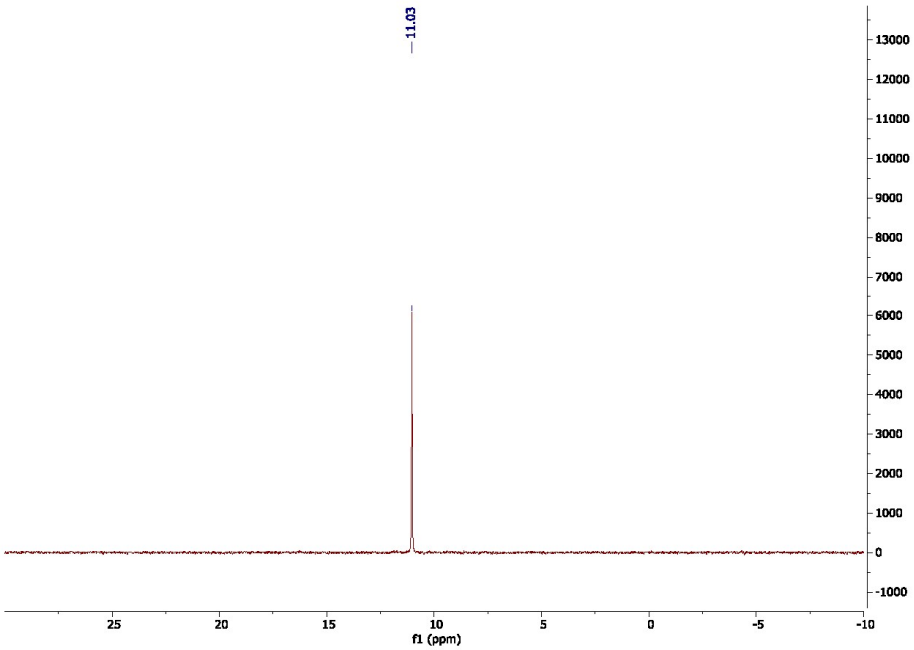

$^{31}P\{^{1}H\}$ NMR (121 MHz, DMSO-d_6)

4. Gas and water sorption

Enthalpy of adsorption was estimated by measuring adsorption isotherms at three temperatures (273, 283, and 293 K), fitting the data to a Freundlich-Langmuir model (Figures S1 and S2), and applying the Clausius-Clapeyron equation:[39]

$$\Delta H_{\text{ads}} = R \ln\left(\frac{p_2}{p_1}\right) \frac{T_1 T_2}{(T_2 - T_1)} \qquad (1)$$

where R = 8.314 J · K^{-1} · mol^{-1} is the gas constant, p_1 and p_2 are two reference pressures, and T_1 and T_2 are the respective reference temperatures.

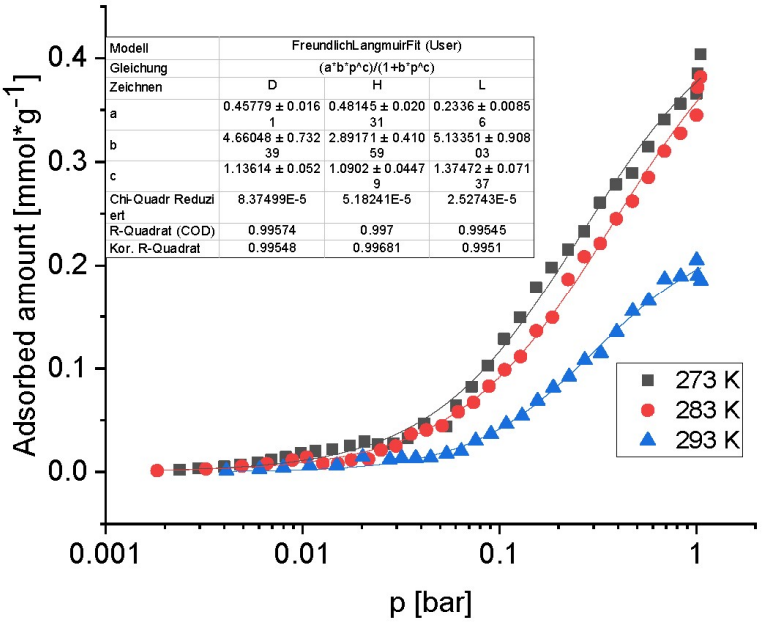

Figure S1: CO_2 adsorption isotherms at different temperatures (on a semi-logarithmic scale), fitted to a Freundlich-Langmuir model.

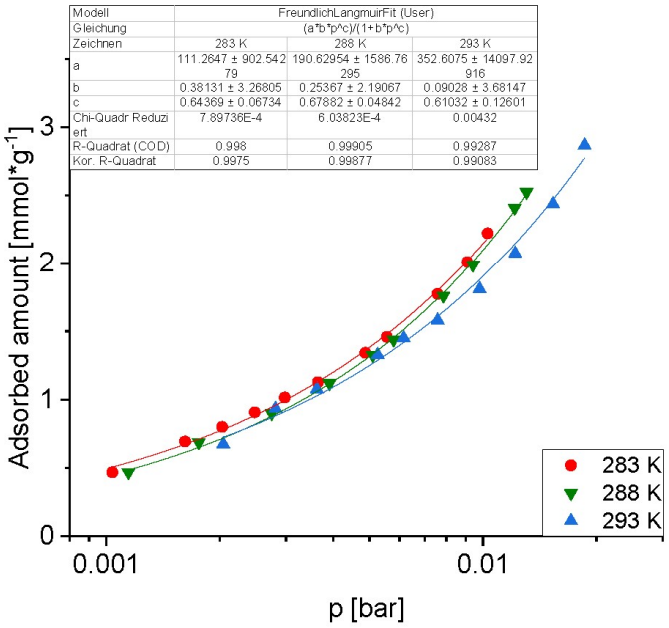

Figure S2: Water adsorption isotherms at different temperatures (on a semi-logarithmic scale), fitted to a Freundlich-Langmuir model.

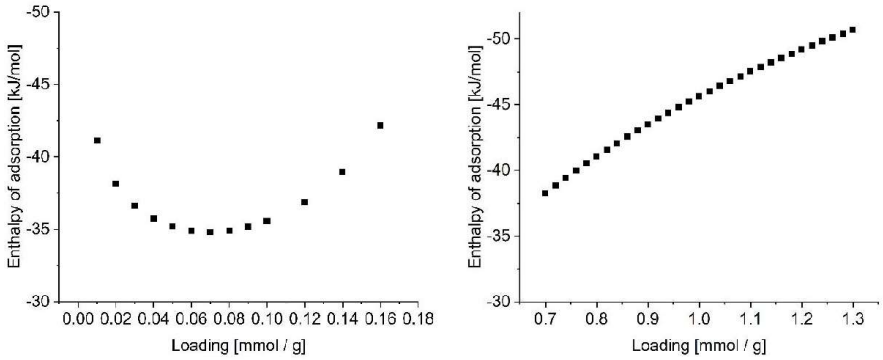

Figure S3: Enthalpy of adsorption against loading of CO_2 (left) and H_2O (right)

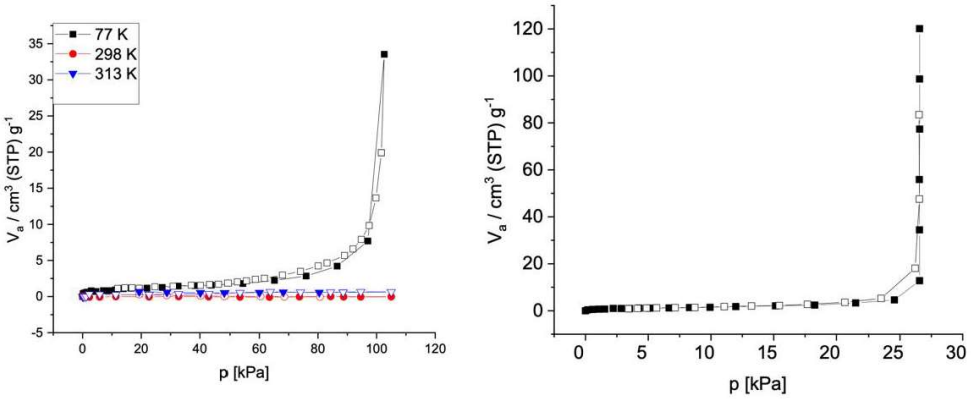

Figure S4: Nitrogen (left) and argon (right) adsorption isotherms for TUB41 (filled symbols – adsorption, empty symbols – desorption).

Below, we present the additional water and CO_2 adsorption isotherms collected over a two-year period.

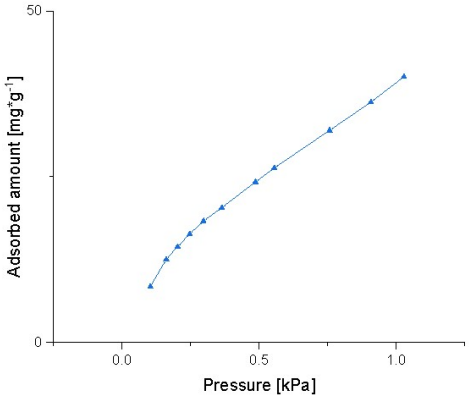

Figure S5: Water adsorption isotherm 1 at 283 K, before condensation

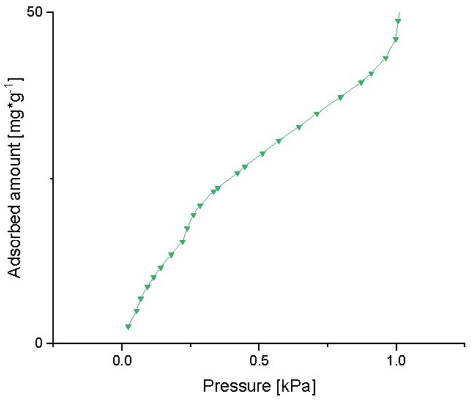

Figure S6: Water adsorption isotherm 2 at 283 K, before condensation

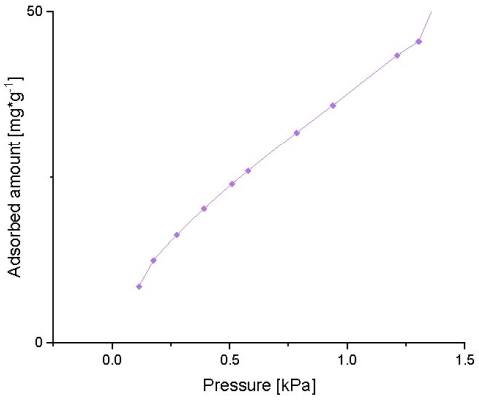

Figure S7: Water adsorption isotherm 1 at 288 K, before condensation

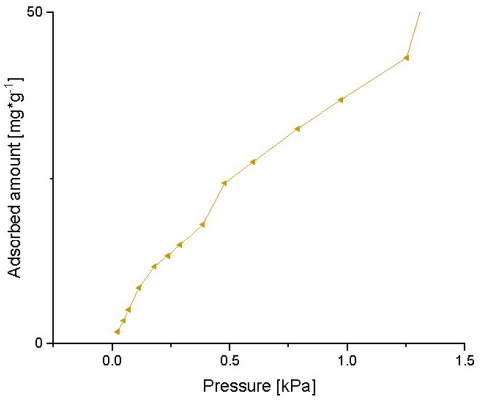

Figure S8: Water adsorption isotherm 2 at 288 K, before condensation

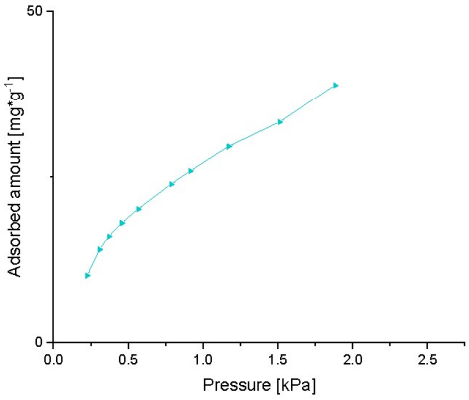

Figure S9: Water adsorption isotherm 1 at 293 K, before condensation

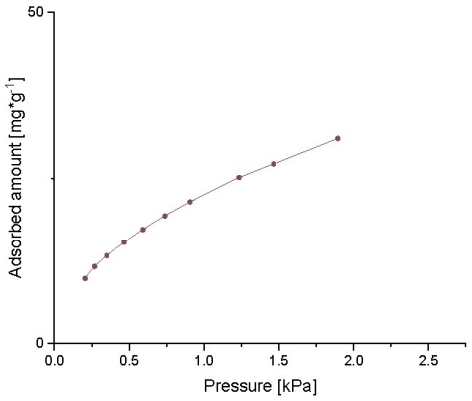

Figure S10: Water adsorption isotherm 2 at 293 K, before condensation

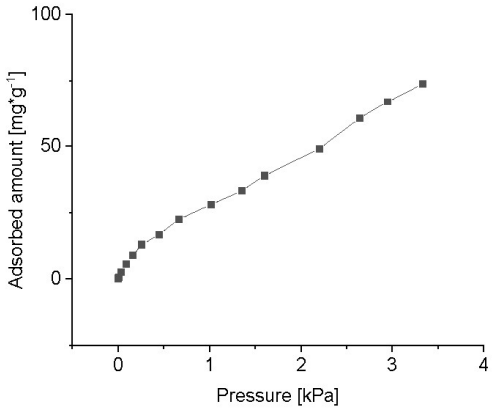

Figure S11: Water adsorption isotherm 1 at 298 K, before condensation

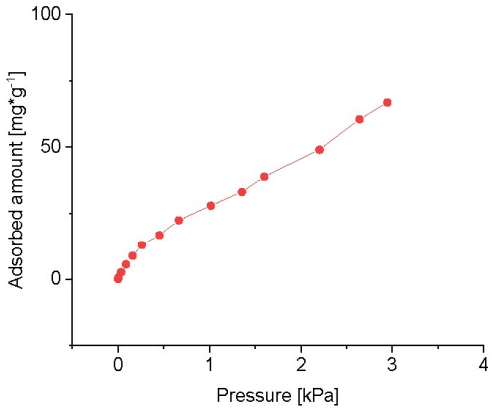

Figure S12: Water adsorption isotherm 2 at 298 K, before condensation

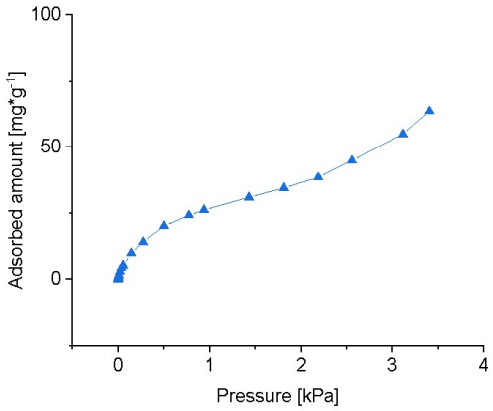

Figure S13: Water adsorption isotherm 1 at 303 K, before condensation

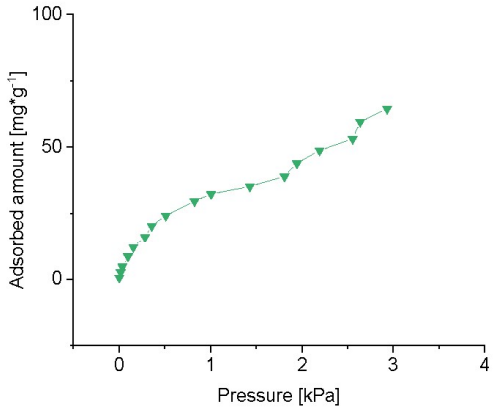

Figure S14: Water adsorption isotherm 2 at 303 K, before condensation

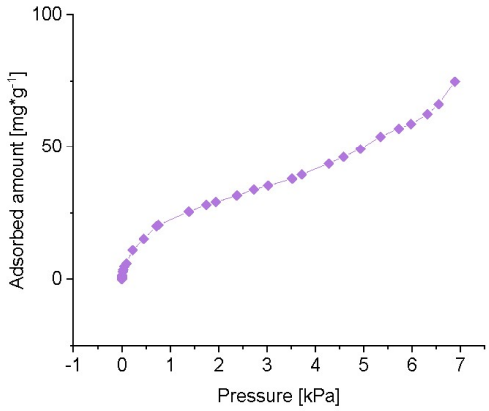

Figure S15: Water adsorption isotherm at 313 K, before condensation

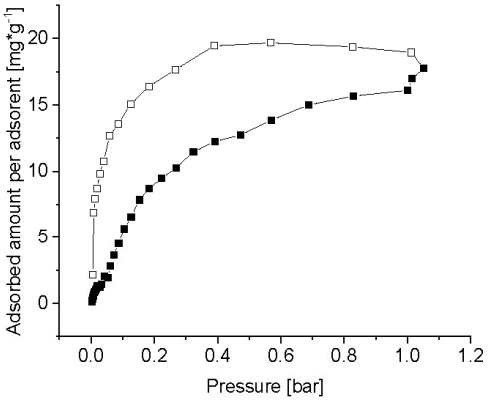

Figure S16: Carbon dioxide adsorption isotherm at 313 K

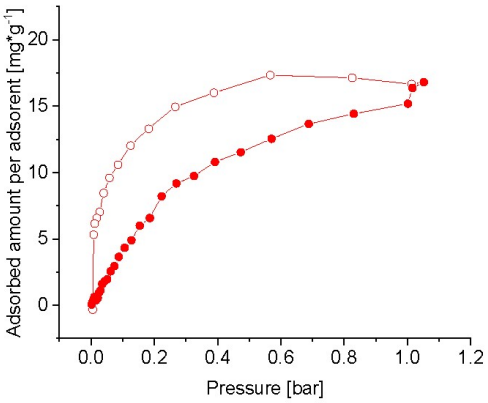

Figure S17: Carbon dioxide adsorption isotherm at 313 K

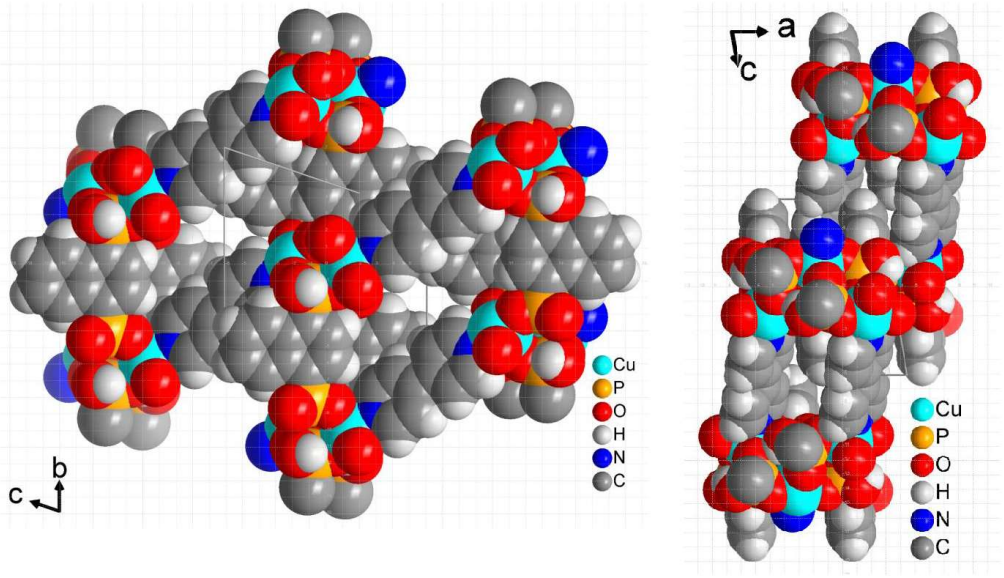

Figure S18: Section of the packing diagram in space-filling mode in two viewing directions to show the pore structure in the 3D network of $[Cu(4,4'\text{-bpy})_{0.5}(1,4\text{-NDPAH}_2)]$. The edges of the grid-squares are 1 Å in length.

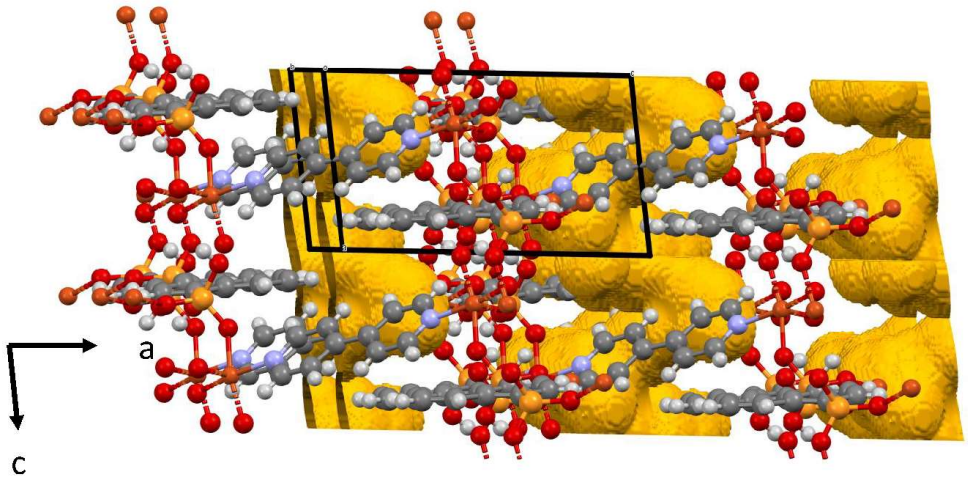

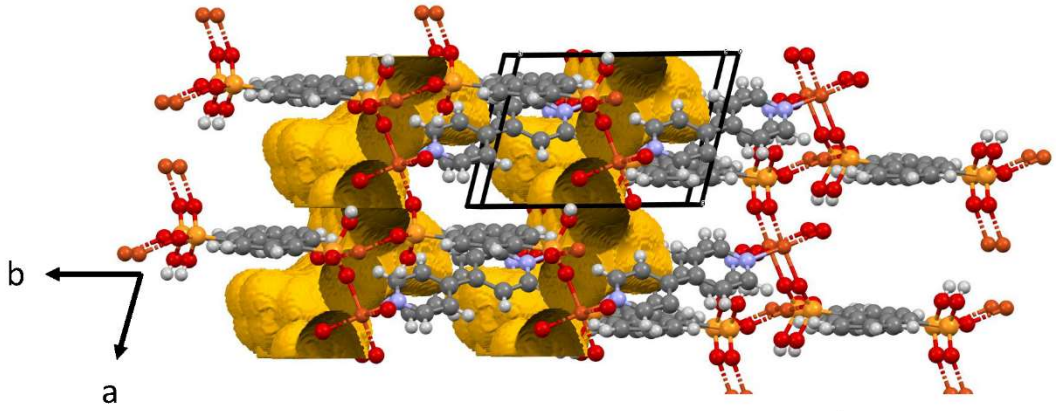

Figure S19: Voids in the MOF [Cu(4,4'-bpy)$_{0.5}$(1,4-NDPAH$_2$)], diameter 2.6 Å, suitable for water adsorption.

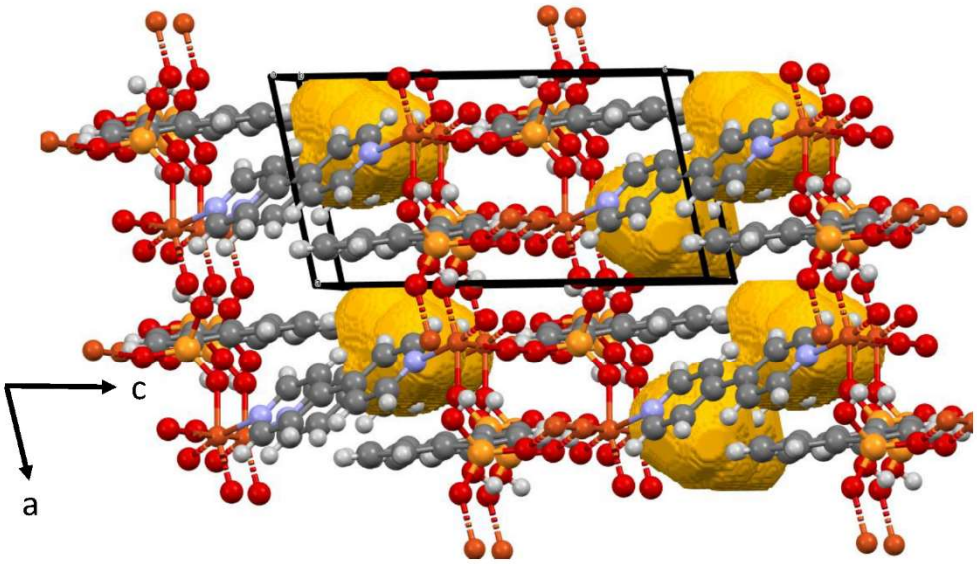

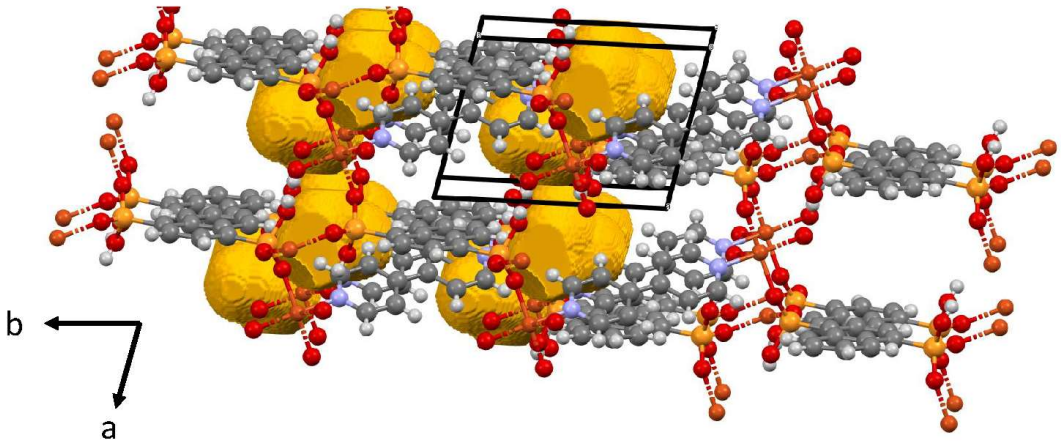

Figure S20: Voids in the MOF [Cu(4,4'-bpy)$_{0.5}$(1,4-NDPAH$_2$)], diameter 3.2 Å, suitable for CO_2 adsorption.

5. Optical spectroscopy

We measured diffuse reflectance spectra of TUB41 in an integrating sphere (diameter of 120 mm, internally coated with BenFlect® with a reflectance > 99% between 350 nm and 2500 nm) setup on a FLS1000 luminescence spectrometer equipped with a 450 W Xe arc lamp, double grating Czerny-Turner monochromators in both excitation and emission compartment and a thermoelectrically cooled (–20 °C) PMT-980 detector from Hamamatsu. All spectra were corrected for wavelength-dependent grating efficiency, detector sensitivity, and fluctuating lamp intensity. The diffuse reflectance, R_∞, was converted to the Kubelka-Munk function, K/S, given by equation (1), which is proportional to the effective absorbance, A, of the powdered sample,

$$\frac{K}{S} = f(R_\infty) = \frac{(1-R_\infty)^2}{2R_\infty} \propto A \qquad (1)$$

if the thickness of the powder slab is sufficiently high such that transmittance along the layer is negligible. Tauc plots were generated by plotting $(f(R_\infty) \cdot E)^{1/2}$ vs. incident photon energy $E = h\nu$ (with $h = 6.626 \cdot 10^{-34}$ Js as Planck's constant and ν as the frequency) for an indirect band gap and $(f(R_\infty) \cdot E)^2$ vs. incident energy E for a direct band gap.

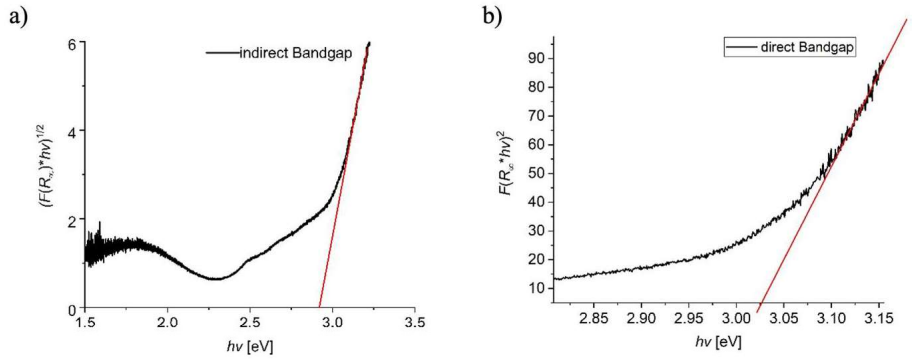

Figure S21: Tauc plots reflecting the a) indirect and b) direct band gap of TUB41.

6. SEM images

Scanning electron microscopy (SEM) images and element mapping analysis were recorded on a Jeol JSM-6510LV QSEM electron microscope equipped with a LaB6 filament and a Bruker XFlash 410-M EDX detector at an acceleration voltage of 20 kV. Prior to the measurement, samples were coated with gold using a Jeol JFC 1200 sputter coater.

7. In-situ variable temperature powder x-ray diffraction (VT-PXRD)

VT-XRD and isothermal XRD experiments were done using Rigaku Smartlab X-ray Diffractometer equipped with Cu K_α x-ray source (λ = 1.54059 Å) with a Hypix-3000 detector, measuring in 1D scanning mode with Bragg–Brentano geometry in horizontal position. The powder sample was prepared on a corundum sample holder and was mounted into a HTK1200N heating stage from Anton Paar. All measurements were performed under normal atmospheric conditions, no vacuum or inert gas was applied. Measurements were performed with an incident slit of 1 mm, 10 mm limiting slit combined with an incident soller slit of 5° and receiving slits #1 of 20 mm and #2 "open". A K_β filter was installed before the detector. Diffraction patterns were collected between 25°C to 350 °C heating rate of 2 K/min resulting

in 2 measurements within 5K. For isothermal XRD the target temperature was held for 3.5 min every 5K. Diffraction was measured from 6-24 °2θ with a step size of 0,01 ° and a speed of 10 °/min, resulting in a 3 min 1 s measurement.

8. Molecular dynamics (MD) simulation

Simulation details:

We adopted the experimentally determined unit cell dimensions and coordinates of the heavy atoms for TUB41, adding hydrogen atoms at appropriate positions. A DFT geometry optimization was subsequently performed in CP2K, employing the PBE functional along with GTH-PBE pseudopotentials, DZVP-MOLOPT-SR-GTH basis set, and DFT-D3(BJ) dispersion corrections. The optimized structure was then used to construct a 12 × 4 × 4 supercell as the initial structure for the MD simulations. Using the this supercell, we built several systems containing varying concentrations of H_2O and CO_2. Specifically, four systems with different H_2O concentrations (containing 10, 30, 100, and 300 H_2O molecules) and three systems with different CO_2 concentrations (containing 10, 30, and 100 CO_2 molecules) were constructed to investigate the distribution, adsorption, and diffusion properties of H_2O and CO_2 within the MOF.

The flexible UFF4MOF force field was employed for TUB41, with the atomic charges fitted using the restrained electrostatic potential–repeating electrostatic potential extracted atomic (RESP-REPEAT) method. The rigid TIP4P model was used for the water molecules, and the TraPPE model was selected for the CO_2 molecules. Interactions between different atom types were determined using the Lorentz–Berthelot mixing rules. A cutoff radius of 12.5 Å was applied for the van der Waals interactions, and the conversion radius between long-range and short-range Coulomb interactions was set to 12 Å. The particle–particle particle–mesh (PPPM) algorithm with a force accuracy set to $1e^{-5}$ was utilized to calculate the long-range electrostatic interactions. Long-range tail corrections were also applied to enhance the accuracy of pressure and energy calculations.

All systems were simulated using LAMMPS (version lammps-omp/20230802). An energy minimization was first performed, followed by a 100 ps NVT equilibration run during which the temperature was gradually increased from 10 K to 300 K. Subsequently, a 50 ns NVT

production run was conducted, with a time step of 0.5 fs. Temperature control was achieved using a Nosé–Hoover thermostat. During the production run, the trajectory data was recorded every 1 ps for further analysis. MDAnalysis (version 2.8.0) was used to calculate radial distribution functions (RDFs) and hydrogen bond numbers. In-house Python scripts were used to generate atomic trajectory overlay maps, and LAMMPS was used to compute mean-squared displacements.

Atomic trajectory overlay maps:

In all the figures shown below, cyan and green represent the oxygen and hydrogen atoms of H_2O, respectively; red and orange represent the carbon and oxygen atoms of CO_2, respectively; gold, dark blue, dark orange, dark red, black, and gray represent copper, nitrogen, phosphorus, oxygen, carbon, and hydrogen atoms, respectively, in the MOF framework. The *x* and *y* axes of the figures correspond to position, expressed in Ångstroms (Å).

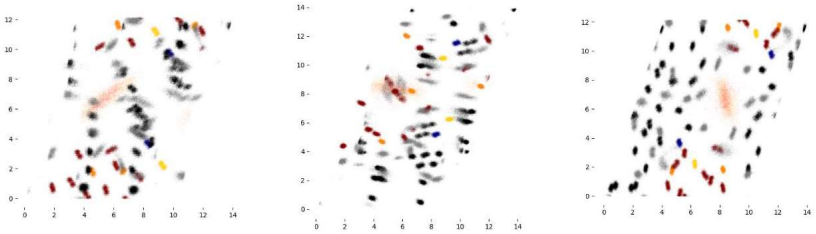

Figure S22: Atomic trajectory overlay maps for TUB41 with 10 CO_2 molecules. From left to right: Projections onto a plane perpendicular to the z, y, and x directions.

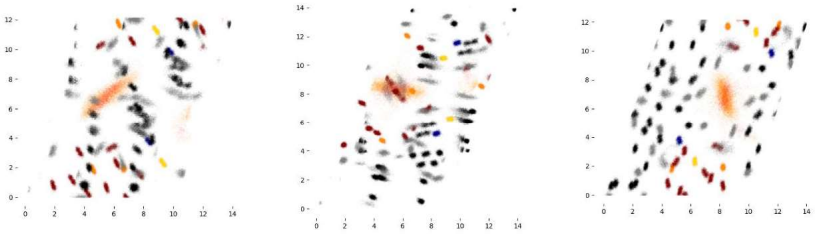

Figure S23: Atomic trajectory overlay maps for TUB41 with 30 CO_2 molecules. From left to right: Projections onto a plane perpendicular to the z, y, and x directions.

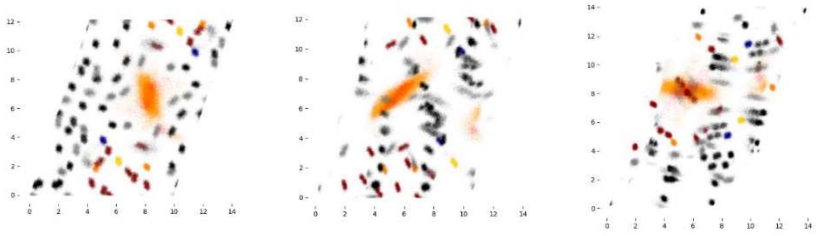

Figure S24: Atomic trajectory overlay maps for TUB41 with 100 CO_2 molecules. From left to right: Projections onto a plane perpendicular to the z, y, and x directions.

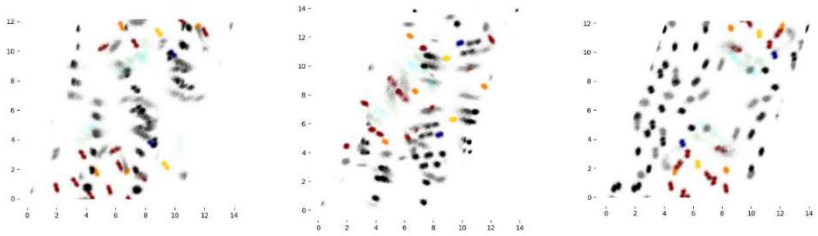

Figure S25: Atomic trajectory overlay maps for TUB41 with 10 H_2O molecules. From left to right: Projections onto a plane perpendicular to the z, y, and x directions.

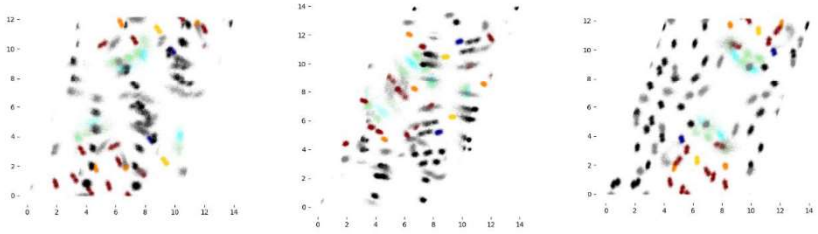

Figure S26: Atomic trajectory overlay maps for TUB41 with 30 H_2O molecules. From left to right: Projections onto a plane perpendicular to the z, y, and x directions.

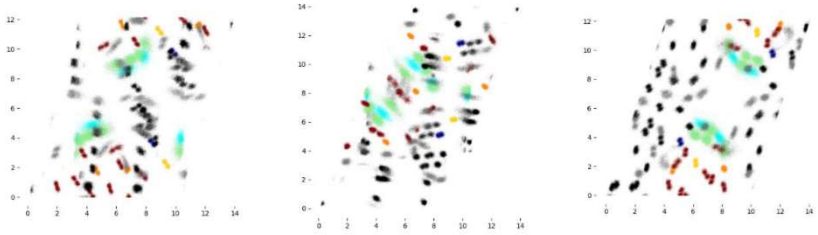

Figure S27: Atomic trajectory overlay maps for TUB41 with 100 H_2O molecules. From left to right: Projections onto a plane perpendicular to the z, y, and x directions.

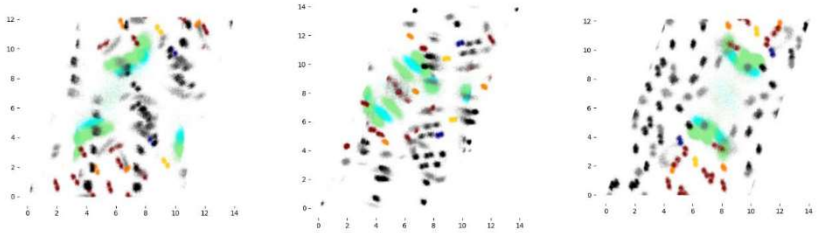

Figure S28: Atomic trajectory overlay maps for TUB41 with 300 H_2O molecules. From left to right: Projections onto a plane perpendicular to the z, y, and x directions.

RDF plots:

a) b)

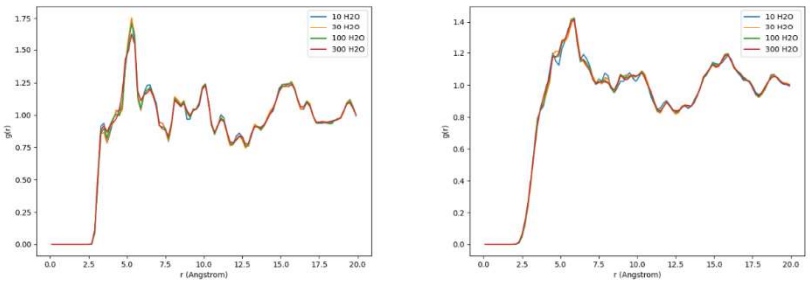

c) d)

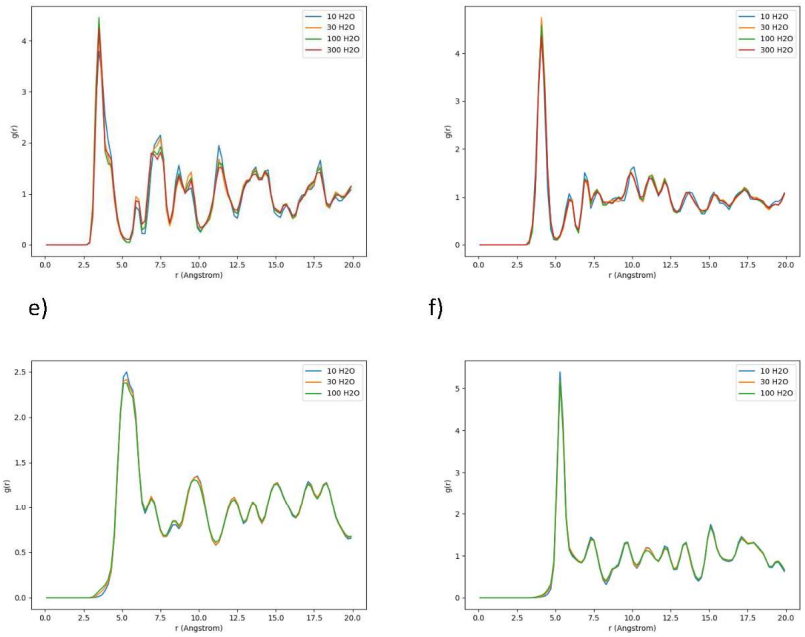

Figure S29: RDFs between atoms in CO_2/H_2O and atoms in the TUB41 framework for all systems. a) O (H_2O) – C (framework) b) H (H_2O) – C (framework) c) O (H_2O) – (framework) d) O (H_2O) – P (framework) e) O (CO_2) – C (framework) f) C (CO_2) – C (framework).

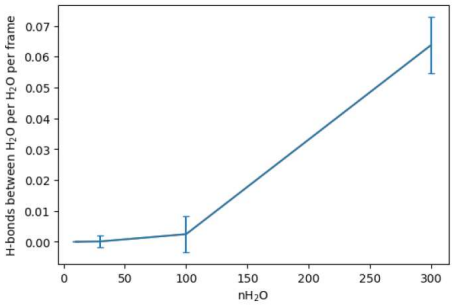

Figure S30: Average number of hydrogen bonds between H_2O molecules for the water-containing systems, normalized by both the number of trajectory frames and the number of H_2O molecules.

3.3 Publications as Co-Author

In addition to the two publications as shared first author I participated in several publications as a shared author with varying degrees of involvement. Publications, relevant excerpts and my contributions are listed in the following part, sorted by publication date.

3.3.1 Metal-Organic Framework MIL-68(In)-NH_2 on the Membrane Test Bench for Dye Removal and Carbon Capture

Monjezi, B. H.; Sapotta, B.; Moulai, S.; Zhang, J.; **Oestreich, R**.; Ladewig, B. P.; Müller-Buschbaum, K.; Janiak, C.; Hashem, T. & Knebel, A.

Chemie Ingenieur Technik, Wiley, **2022***, 94*, 135-144. DOI: 10.1002/cite.202100117

Contributions to this publication:

- Proofreading of the manuscript

The metal-organic framework (MOF) MIL-68(In)-NH_2 was tested for dye removal from wastewater and carbon capture gas separation. MIL-68(In)-NH_2 was synthesized as a neat, supported MOF thin film membrane and as spherical particles using pyridine as a modulator to shape the morphology. The neat MIL-68(In)-NH_2 membranes were employed for dye removal in cross-flow geometry, demonstrating strong molecular sieving. MIL-68(In)-NH_2 particles were used for electro- spinning of poylethersulfone mixed-matrix membranes, applied in dead-end filtration with unprecedented adsorption values. Additionally, the neat MOF membranes were used for H_2/CO_2 and CO_2/CH_4 separation.

3.3.2 Observation of Rare Tri^6Di^9 Imine Cages Using Highly Fluorinated Building Blocks

Fleck-Kunde, T.; Wolpert, E. H.; Horst , L. z.; **Oestreich, R.**; Janiak, C.; Jelfs, K. E. & Schmidt, B. M.

Ligand Following the Principles of the Supramolecular Building Layer Approach

Molecules, MDPI AG, **2022***, 27*, 5374. DOI: 10.1039/D2CE01170K

Contributions to this publication:

- Performance and analysis of gas sorption measurements
- Proofreading of the manuscript

Two structurally distinct Tri6Di9 cages were synthesized by combining a highly fluorinated aldehyde with two ditopic amines. Although the pure compounds could not be isolated despite many attempts, the information obtained is critical for the future design of large supramolecular structures. Computational and experimental methods indicate that the addition of perfluorinated aromatic linkers

in the assembly of porous organic cages opens up new possibilities for influencing the reaction pathway towards rare and unknown structures.

All samples were degassed at 80 °C under vacuum for 18 h. Nitrogen, hydrogen, carbon dioxide and methane adsorption measurements were performed for characterization. A micropore volume of 0.18 cm3 g-1 and a total pore volume of 0.30 cm3 g-1 were determined from the nitrogen isotherm measured at 77 K. The CO2 measurements at 273 K in contrast showed only a much smaller micropore volume of 0.011 cm3 g-1, showing only a few ultramicropores suitable for carbon dioxide adsorption.

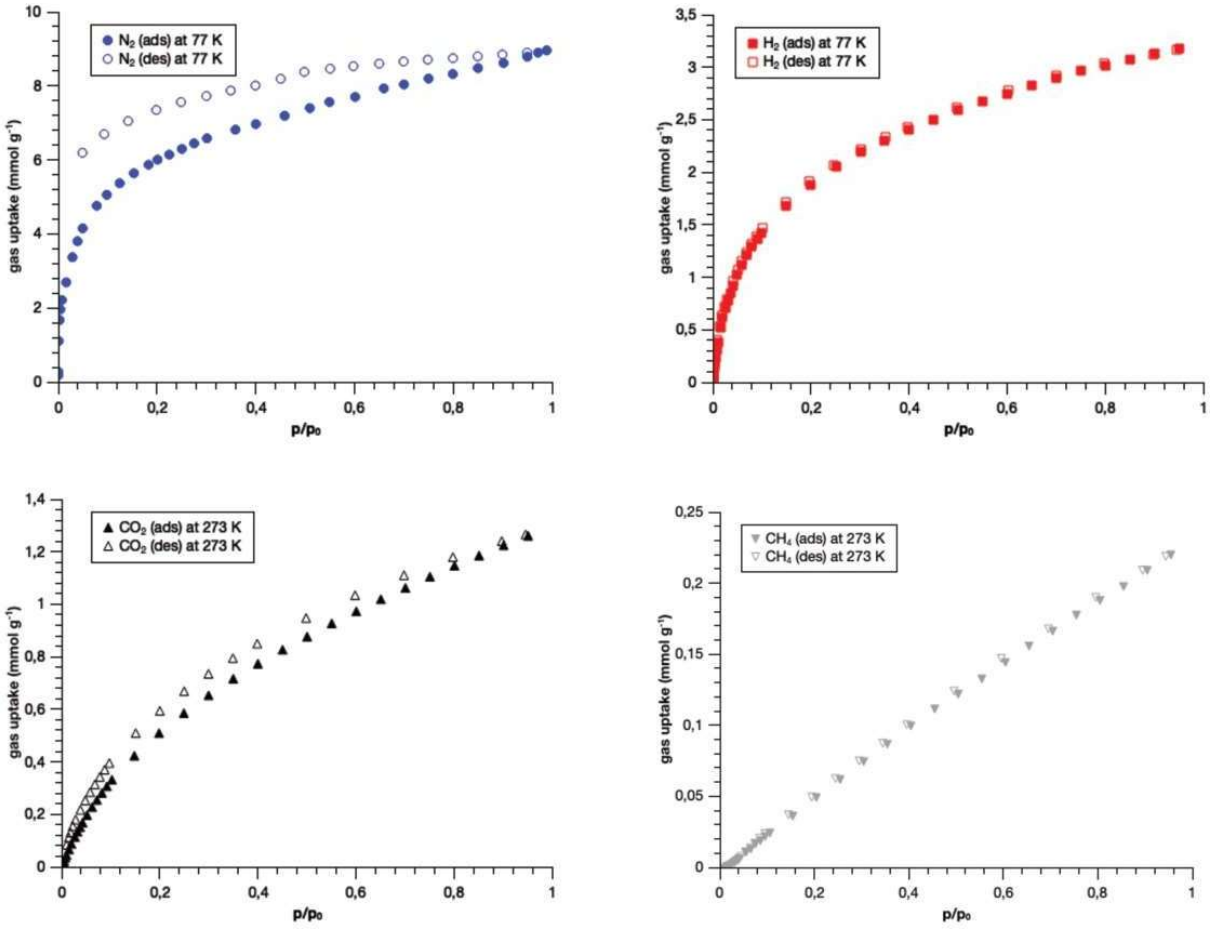

Figure 5: Gas adsorption measurements of the amorphous cage mixture Tri4Di6 + Tri6Di9 isolated via precipitation from n-hexane. Adsorption and desorption curves for N2 (top left), H2 (top right), CO2 (bottom left) and CH4 (bottom right).

NLDFT calculations (using the adsorption branch of the nitrogen isotherm and assuming slit/cylindrical pores) showed a narrow pore size distribution centered at a half-pore width of 6.8 Å with some larger mesopores with a half-pore width between 17 and 40 Å (Figure 6).

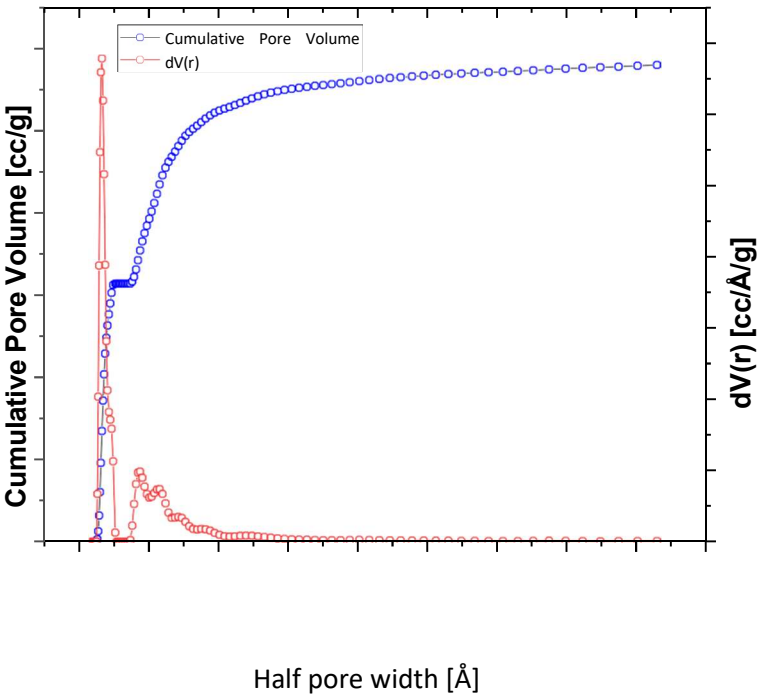

Figure 6: Pore size distribution of the imine cage mixture Tri^4Di^6 + Tri^6Di^9

3.3.3 Synthesis of a Chiral 3,6T22-Zn-MOF with a T-Shaped Bifunctional Pyrazole-Isophthalate Ligand Following the Principles of the Supramolecular Building Layer Approach

Woschko, D.; Millan, S.; Ceyran, M.-A.; **Oestreich, R.** & Janiak, C.

Molecules, *MDPI AG*, **2022**, *27*, 537

Reprinted according to Creative Commons 4.0

Contributions to this publication:

- Performance and analysis of gas sorption measurements
- Proofreading of the manuscript

A new metal–organic framework (MOF) [Zn(Isa-az-tmpz)] · ~1–1.5 DMF with the novel T- shaped bifunctional linker 5-(2-(1,3,5-trimethyl-1H-pyrazol-4-yl)azo)isophthalate (Isa-az-tmpz) was synthesized. Both enantiomers, with the chiral tetragonal space groups $P4_32_12$ or $P4_12_12$, were produced in different ratios. Topological analysis of the product showed the rare **3,6T22**-topology, in contrast to the expected **rtl**-topology, in which pyrazolate-isophthalate-functionalized MOFs, also synthesized by using the supramolecular building layer (SBL) approach, crystallize. **3,6T22**-[Zn(Isa-az-tmpz)] · ~1–1.5 DMF is a potentially porous, three-dimensional structure and DMF molecules are incorporated into the corrugated channels along the *a* and *b*-axis of the as synthesized material. Due to the small trigonal cross-section of about 6 × 4 Å (assuming van der

Waals surface) N_2 and Ar can't enter the ultramicropores under cryogenic conditions. Only the smaller H_2 (at 87 K) and CO_2 (at 195 K) molecules are able to infiltrate the structure, with gas uptakes of 2 mmol g^{-1} and 5.4 mmol g^{-1}, respectively. A BET surface area of 496 $m^2 \cdot g^{-1}$ was calculated from CO_2 adsorption. Thermogravimetric analysis of the compound shows a thermal stability of up to 400 °C.

Before gas sorption measurements the product was dried with supercritical carbon dioxide. After activation for 3 h at 120 °C under vacuum nitrogen and argon isotherms were recorded at cryogenic temperatures (77 and 87 K, respectively), but no significant gas uptake could be detected due to kinetic limitations at these low temperatures. To test for the expected ultramicropores, a hydrogen (87 K) isotherms was recorded (Figure 7, left), showing an uptake of 2 mmol g^{-1}. The carbon dioxide isotherm measured at 195 K displayed type I(b) behaviour according to the IUPAC classification, characteristic for microporous materials (Figure 7, right). From this, a Langmuir surface area of 588 $m^2 \cdot g^{-1}$ and a BET surface area of 496 $m^2\, g^{-1}$ were calculated. Following the Gurvich rule, and by dividing the amount of CO_2 adsorbed at 1 bar, 120 $cm^3\, g^{-1}$, through the density of the adsorbed carbon dioxide, assumed as $\rho_{CO2}(195\ K) = 1.08\ g\ cm^{-3}$, gave a total accessible pore volume of 0.22 $cm^3\, g^{-1}$. These differences in uptake can be explained by the different kinetic diameters of N_2, Ar, H_2 and CO_2 (3.64, 3.4, 2.89 and 3.30 Å respectively) and the kinetic hindrances for nitrogen and argon at the cryogenic measurement temperatures, while the kinetic inhibition was much reduced for hydrogen and carbon dioxide.

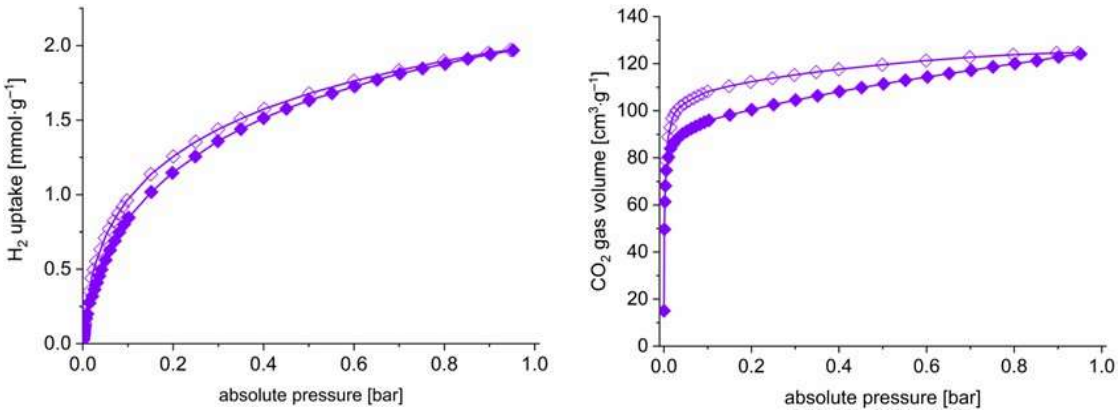

Figure 7: Isotherms of H_2 at 87 K (left) and CO_2 at 195 K (right)

3.3.4 A diamantane-4,9-dicarboxylate based UiO-66 analogue: challenging larger hydrocarbon cage platforms

Gvilava, V.; Vieten, M.; **Oestreich, R**.; Woschko, D.; Steinert, M.; Boldog, I.; Bulánek, R.; Fokina, N. A.; Schreiner, P. R. & Janiak, C.

CrystEngComm, Royal Society of Chemistry (RSC), **2022**, *24*, 7530-7534. DOI: 10.1039/D2DT03719J

Contributions to this publication:

- Performance and analysis of gas sorption measurements
- Proofreading of the manuscript

A bulky barrel-shaped diamantine based ligand was used for the first time in HHUD-3, an analogue to UiO-66, in which access to the pores is only possible due to defect structure. A defect rate of 35 % missing linker was determined from crystal structure and sorption measurements, leading to higher methane, but reduced carbon dioxide and hydrogen uptake compared to UiO-66.

After activation at 140 °C under vacuum, nitrogen and argon sorption measurements were performed under cryogenic temperatures (

). Both gases showed a similar BET surface area of 869 $m^2 g^{-1}$ and 811 $m^2 g^{-1}$, respectively. The micropore volume was determined as 0.244 $cm^3 g^{-1}$ and 0.211 $cm^3 g^{-1}$. These values were compared with the calculations of a theoretical surface area based on different defect rates and lay roughly in the middle between a defect-free compound and one with the theoretical maximum of effects, indicating a defect rate of 50 %. The type I(b) behaviour shown by both isotherms suggests micropores, while the minimal hysteresis most closely resembles type H3, showing a textural effect of aggregated crystals.

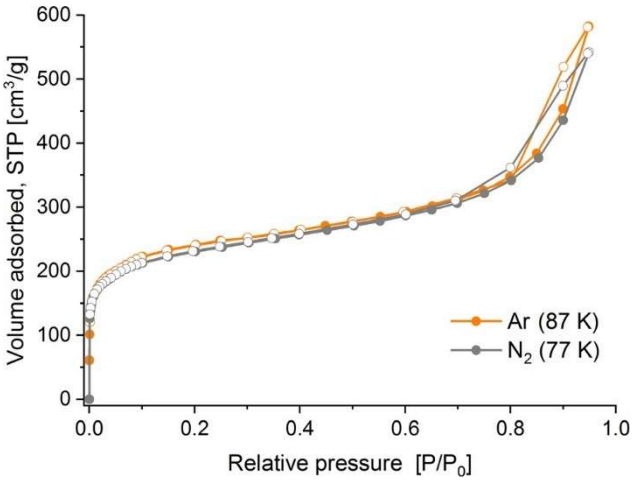

Figure 9: N_2 and Ar adsorption isotherms for HHUD-3 (the adsorption branches are represented

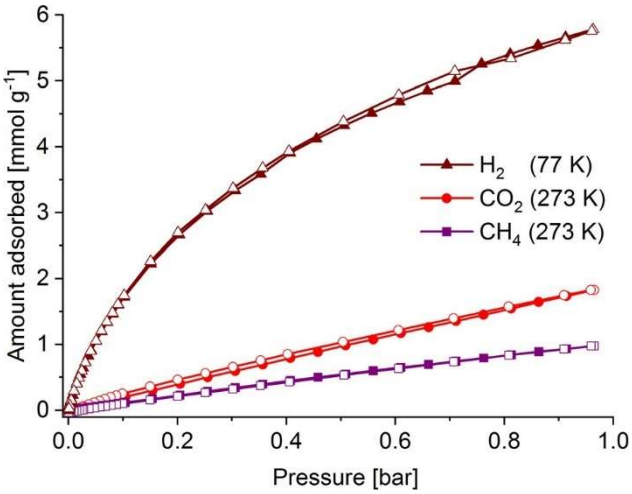

Figure 8: H_2, CH_4, and CO_2 sorption isotherms for HHUD-3 (the adsorption branches are represented by filled symbols and the desorption branches by empty symbols).

Figure 8 shows the adsorption isotherms for hydrogen, carbon dioxide and methane. Compared to UiO-66 uptake of CO_2 at 273 K is reduced from 3.14 mmol g^{-1} to 1.90 mmol g^{-1}, of H_2 at 77 K from 6.95 mmol g^{-1} to 5.88 mmol g^{-1} and increased for CH_4 from 0.84 mmol g^{-1} to 1.01 mmol g^{-1}. Lowered uptake of CO2 and H2 is in accordance with the decreased surface area, while the increased amount of adsorbed CH4 can tentatively be explained by suitably-shaped diamantane-lined pockets in HHUD-3 in the structure, which can form multiple CH···HC London dispersion contacts with significant cumulative strength.

3.3.5 Enhanced sorption in an indium-acetylenedicarboxylate metal–organic framework with unexpected chains of *cis*-μ-OH-connected {InO_6}octahedra

Woschko, D.; Yilmaz, S.; Jansen, C.; Spieß, A.; **Oestreich, R.**; Ntep, T. J. M. M. & Janiak, C. Dalton Transactions, Royal Society of Chemistry (RSC), **2023**, *52*, 977-989. DOI: 10.1039/D2DT03719J

Reprinted according to Creative Commons 3.0

Contributions to this publication:

- Performance and analysis of gas sorption measurements
- Proofreading of the manuscript

Single crystals of the new metal–organic framework (MOF) In-adc (HHUD-4) were obtained through the reaction of linear acetylenedicarboxylic acid (H_2adc) with $In(NO_3)_3 \cdot xH_2O$. Gas sorption measurements showed micropores and good uptake of both hydrogen and carbon dioxide.

Measurements were also performed for the related MOF In-fum to provide a comparison between the triple and double bonds in the . Following vapor sorption measurements revealed high uptake of volatile organic compounds (VOC) at low pressures and good selectivity between benzene and n-hexane.

Nitrogen sorption measurements (Figure 10) at cryogenic temperatures showed type I isotherms, characteristic for micropores, with a minimal type H4 hysteresis, possibly from inter-particle voids. BET surface areas between 660 $m^2\ g^{-1}$ and 940 $m^2\ g^{-1}$ were found, with the lower values similar to the ones measured for In-fum. On these low-surface samples and In-fum CO_2, CH_4 and H_2 measurements were performed (Figure 11) at varying temperatures to determine selectivities and heats of adsorption.

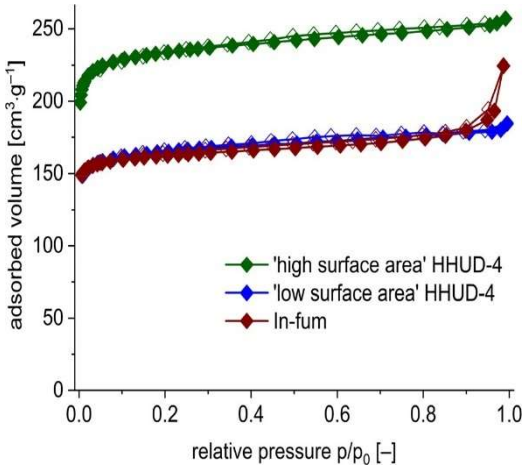

Figure 10: Volumetric N_2 sorption experiments of high and low surface area HHUD-4 and In-fum at 77 K (filled symbols for adsorption, empty symbols for desorption).

The results showed a CO_2 uptake increased by 56% for the new HHUD-4 in comparison to In-fum, showcasing the advantage of the C-C triple bond. From isotherms obtained at 273 and 293 K the isosteric heat of adsorption was calculated, giving a zero-coverage heat of adsorption Q_{ST}^0 of circa 29 kJ mol^{-1}. Methane capacity was also increased by about 29 % compared to In-fum, while Q_{ST}^0 was 26 respectively 29 kJ mol^{-1}, showing only minor differences in the affinity. Hydrogen uptake was only slightly increased from 5.78 mmol g^{-1} to 6.36 mmol g^{-1}, but Q_{ST}^0 was ca. 40 % higher (11.4 kJ mol^{-1} compared to 8.2 kJ mol^{-1}.

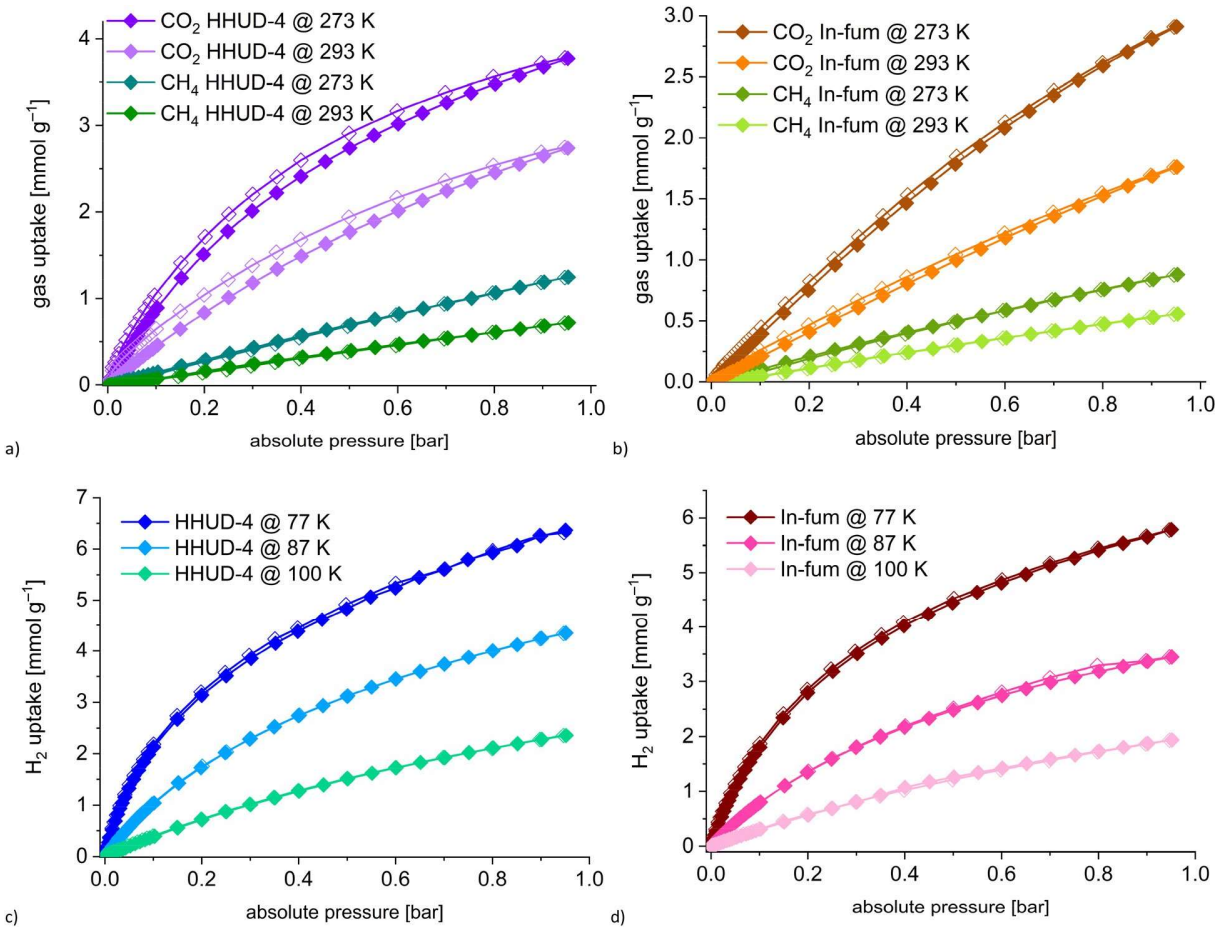

Figure 11: CH_4 and CO_2 sorption isotherms at 273 and 293 K and H_2 sorption isotherms at 77, 87 and 100 K for HHUD-4 (a and c) and In-fum (b and d), respectively (filled symbols for adsorption, empty symbols for desorption).

3.3.6 A facile spray-pressing synthesis approach for reusable photothermal masks

Lu, Y.; Liu, Y.-X.; Wang, Y.; Oestreich, R.; Xu, Z.-Y.; Zhang, W.; Hügenell, P.; Janiak, C. & Yang, X.-Y. iScience, Elsevier BV, 2023, 26, 107286. DOI: 10.1016/j.isci.2023.107286

Reprinted according to Creative Commons 4.0

Contributions to this publication:

- Proofreading of the manuscript

A facile spray-pressing technique for the production of face masks by adding a graphene layer on one side of meltblown fabric and a functional MOF-layer on the other side was developed. The possibility for upscaling was tested in a model plant. Antibacterial properties and stability were researched.

3.3.7 $[Zr_6(\mu_3\text{-}O)_4(\mu_3\text{-}OH)_4](1\text{-adamantanecarboxylate})_{12}]$: a model for extrinsic "defect-engineerable" porosity

Gvilava, V.; Vieten, M.; Heinen, T.; **Oestreich, R**.; Boldog, I. & Janiak, C. Zeitschrift für anorganische und allgemeine Chemie, Wiley, **2023**, 649. DOI: 10.1002/zaac.202300106

Contributions to this publication:

- Proofreading of the manuscript
- Gas sorption measurements and evaluation

The molecular zirconium-oxo cluster with 1-adamantecarboxylate, with theideal formula [Zr6O4(OH)4(AdCA)12] (AdCA = 1-adamantanecarboxylate),is near spherical in shape with a hydrophobic "shell" of bulky rigid adamantyl groups. Both formic acid, used as a modulator, and a large excess of the HAdCA were found to be essential for its reproducible synthesis and the formation of well-formed rhombohedral single crystals of 100-150 μm. Crystallization in the presence of formic acid however leads to ligand-substitution defects (1-2 out of 12), which were quantified by thermogravimetry and NMR. A defect-engineering with a higher defect ratio in such oxo clusters is a promising approach aiming at extrinsic porosity.

First measurements of surface via nitrogen sorption isotherms at 77 K, after activation at elevated temperatures and vacuum, showed no accessible surface area. A repeated measurement after supercritical CO_2 drying, followed by further activation at 190 °C under vacuum, yielded a BET surface area of ca 146 $m^2\ g^{-1}$. A minimal H2-type hysteresis indicated a mesoporous solid with 'ink-bottle' type pores.

A carbon dioxide isotherm recorded at 273 K gave an uptake of 0.55 mmol g-1, while hydrogen uptake was measured to be 1.2 mmol g-1 at 77 K and 1 bar. Both these values agreed with the expected values from the calculated structure.

3.3.8 Synthesis of Ketjenblack Decorated Pillared Ni(Fe) Metal-Organic Frameworks as Precursor Electrocatalysts for Enhancing the Oxygen Evolution Reaction

Beglau, T. H. Y.; Rademacher, L.; Oestreich, R. & Janiak, C.

Molecules, MDPI AG, **2023**, 28, 4464. DOI: 10.3390/molecules28114464

Reprinted according to Creative Commons 4.0

Contributions to this publication:

- Proofreading of the manuscript
- Gas sorption measurements and evaluation

Through a facile one-step solvothermal method, the Ni-based pillared metal-organic framework [Ni2(BDC)2DABCO] (BDC = 1,4-benzenedicarboxylate, DABCO = 1,4-diazabicyclo[2.2.2]octane), its bimetallic nickel-iron form [Ni(Fe)(BDC)2DABCO], and their modified Ketjenblack (mKB) composites were synthesized and tested toward OER in an alkaline medium (KOH 1 mol L−1) and showed promising properties as a catalyst for that reaction. Furthermore, insight into the in situ transformation of Ni(Fe)DMOF into OER-active α/β-$Ni(OH)_2$, β/γ-NiOOH, and FeOOH was gained. Residual porosity, characterized by powder X-ray diffractometry and N_2 sorption analysis, inherited from the MOF structure, contributed to the favourable properties. Benefitting from the porosity structure of the MOF precursor, the nickel-iron catalysts outperformed the solely Ni-based catalysts due to their synergistic effects and exhibited superior catalytic activity and long-term stability in OER.

Since the electrochemical performance of the electrode materials is strongly correlated to surface area and properties, nitrogen isotherms were measured (Figure 12, left). Type I isotherms, characteristic for microporous materials, were found for NiDMOF and Ni(Fe)DMOF (. BET calculations gave a surface area of 2104 $m^2 g^{-1}$ and a total pore volume of 0.82 $cm^3 g^{-1}$ for NiDMOF, and 1942 $m^2 g^{-1}$ and 0.80 $cm^3 g^{-1}$ for Ni(Fe)DMOF. The modified Ketjenblack carbon (mKB) showed a BET surface area of 1234 $m^2 g^{-1}$ and a total pore volume of 1.5 $cm^3 g^{-1}$, identical to the unmodified Ketjenblack.

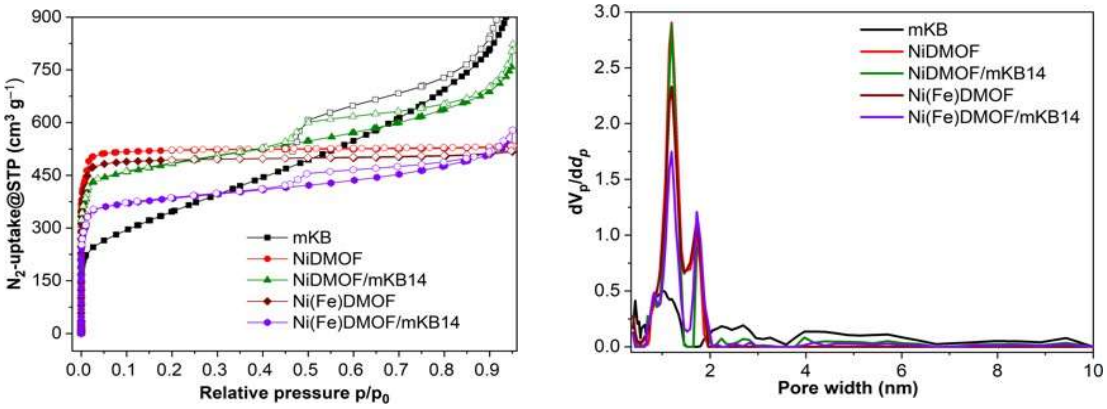

Figure 12: Nitrogen sorption isotherms at 77 K (filled symbols adsorption; empty symbols desorption), left, and pore size distribution of NiDMOF, NiDMOF/mKB14, Ni(Fe)DMOF, Ni(Fe)DMOF/mKB14 and mKB, right

For the composites of NiDMOF and mKBx (x = 7, 14, 22, 34 wt. %) and Ni(Fe)DMOF/mKB14 the calculated surface areas were lower than the estimates based on a simple mass weighted combination of both materials, indicating the occurrence of mutual pore blocking effects. This might be caused by the growth of NiDMOF into the mKB pores or on top of the mKB surface, thus limiting access to the pores. This was confirmed by SEM pictures.

In contrast to the other samples, NiDMOF/mKB14 showed higher total pore volume than expected from just assuming a combination (1.18 $cm^3\ g^{-1}$ instead of 0.92 $cm^3\ g^{-1}$), also giving the highest pore volume of all samples.

By NLDFT calculations, assuming cylindrical channels, the pore size distributions were determined (Figure 12, right), showing micropores with a diameter between 1.2 and 1.7 nm. For the composites NiDMOF/mKBx and Ni(Fe)DMOF/mKB14 small mesopores just above 2 nm diameter were also found. The increased pore volume of NiDMOF/mKB14 was traced to interparticle pores with a diameter around 5 nm.

These open cylindrical channels offer active sites for the OER and mesoporous channels enhance electrolyte diffusion.

3.3.9 Nano-Sized Channels Resulting from the Packing of Discrete 3d–4f Metal Complexes in Crystals

Apostol, A. A.; **Oestreich, R.**; Maxim, C.; Romanitan, C.; Badea, M.; Janiak, C. & Andruh, M. Crystal Growth & Design, American Chemical Society (ACS), **2023**, 23, 3740-3746. DOI: 10.3390/molecules28062716

Contributions to this publication:

- Proofreading of the manuscript
- Gas and vapor sorption measurements and evaluations
- Discussion and input to further measurement methods

The heterobinuclear complexes $[M^{II}Dy^{III}(valpn)(hfac)_2(pb)]\cdot 0.67H_2O\cdot$ (solvent) were synthesized and analyzed (M = Zn 1a, Cu 2, Ni 3; $hfac^-$ = hexafluoroacetylacetonate; $valpn^{2-}$ is the dianion of the Schiff base that resulted from the condensation reaction between *o*- vanillin and 1,3-diaminopropane; and pb^- = 1-pyrenebutyrate). These complexes from large and small channels, with the large channels being padded by CF_3 groups arising from the $hfac^-$ ligands. Considering the van der Waals surface, the diameter of the almost circular cross-section of the large channels is about 1.2 nm. Five different crystals were won, 1b being 1a with removed solvent molecules and 1c was formed by incorporating iodine molecules in the small channels of 1b. In compounds 1a, 1b, 1c, and 2, the 3d metal ions (Zn^{II} and Cu^{II}) show a square-pyramidal geometry. If the 3d metal ion is nickel(II), with an octahedral geometry, the packing of the molecules, $[Ni^{II}Tb^{III}(MeOH)(valpn)$- $(hfac)_2(pb)]\cdot$ 3, is different, without formation of channels. In all these compounds, the segregation of the trifluoromethyl groups was observed.

In order to characterize the porosity of the complex $[Zn^{II}Dy^{III}(valpn)(hfac)_2(pb)]\cdot 0.67H_2O\cdot$ (solvent) , nitrogen and carbon dioxide isotherms, at 77 and 273 K respectively, were recorded after activation at 120 °C for 3 h under vacuum.

For both gases only a minimal adsorption was found, corresponding to a BET-surface area of 3 $m^2\ g^{-1}$ for nitrogen and 10 $m^2\ g^{-1}$ for carbon dioxide. Since the theoretical structure included large channels, an argon isotherm was measured at 87 K, but the adsorption was very low again.

Following that, vapor sorption measurements were undertaken, both with water and hexafluorobenzene, C_6F_6, at 293 K. For both vapors sizeable adsorption could be detected, especially

for C_6F_6: Water uptake reached 14 mg g^{-1} at the isotherm end point (relative pressure 0.92, absolute pressure 0.0228 bar), while hexafluorobenzene uptake was 201 mg g^{-1} at a relative pressure of 0.90 (0.07985 bar).

The explanation for this phenomenon is the existence of only small pores, which are also lined with perfluorinated groups, excluding most molecules, which cannot positively interact with the pore walls.

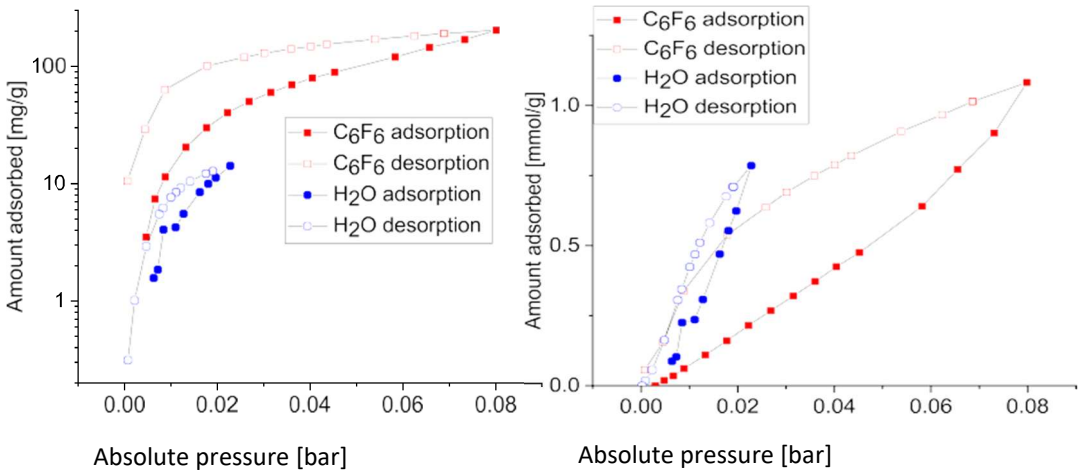

Figure 13: Vapor sorption isotherms of C_6F_6 (red) and water (blue) with uptake in mg/g (logarithmic scale of y-axis (left) and in mmol/g (right)

3.3.10 Formation of Gold Nanoclusters from Goldcarbonyl Chloride inside the Metal-Organic Framework HKUST-1

Hassan, Z. M.; Guo, W.; Welle, A.; **Oestreich, R.**; Janiak, C. & Redel, E. Formation of Gold Nanoclusters from Goldcarbonyl Chloride inside the Metal-Organic Framework HKUST-1

Molecules, MDPI AG, **2023***, 28*, 2716. DOI: 10.1039/D3DT03695B

Reprinted according to Creative Commons 4.0

Contributions to this publication:

- Proofreading of the manuscript

To form gold clusters within the pores of HKUST 1 ($[Cu_3(BTC)_2(H_2O)_2]$, Cu-BTC) SURMOFs (surface-mounted metal-organic frameworks; BTC = benzene-1,3,5-tricarboxylate), the gaseous precursor, carbonylchloridogold(I), Au(CO)Cl, decomposed within the pores of HKUST-1 through hydrolysis with the aqua ligands on Cu. In the medium-sized pores of the HKUST-1 matrix small Au_x clusters with an average atom number of $x \approx 5$ are formed, distributed homogenously and crystallographically ordered. This was supported by simulations of the powder X-ray diffractometric

characterization. Further characterization of Au_x@HKUST-1 was performed by nfrared reflection absorption (IRRA) as well as Raman spectroscopy, by scanning electron microscopy (SEM), inductively coupled plasma optical emission spectroscopy (ICP-OES), time-of-flight secondary ion mass spectrometry (ToF-SIMS) and X-ray photoelectron spectroscopy (XPS).

3.3.11 Bimetallic CPM-37(Ni,Fe) metal–organic framework: enhanced porosity, stability and tunable composition

Abdpour, S.; Fetzer, M. N. A.; **Oestreich, R**.; Beglau, T. H. Y.; Boldog, I. & Janiak, C. Dalton Transactions, Royal Society of Chemistry (RSC), **2024**, 53, 4937-4951. DOI: 10.1039/D3DT03695B

Contributions to this publication:

- Proofreading of the manuscript
- Gas and vapor sorption measurements and evaluations
- Discussion and input to further measurement methods

A new series of bimetallic CPM-37(Ni,Fe) metal-organic frameworks with differing iron to nickel ratio (Ni/Fe ca 2, 1, 0.5, designated as CPM-37(Ni_2Fe), CPM-37(NiFe) and CPM-37($NiFe_2$)) was synthesized. Nitrogen isotherms were recorded at 77 K, showing very high BET surface areas of 2039, 1955 and 2378 $m^2\ g^{-1}$ for CPM-37(Ni_2Fe), CPM-37(NiFe) and CPM-37($NiFe_2$), largely increased compared to the monometallic CPM-37(Ni) and CPM-37(Fe) with 87 and 368 $m^2\ g^{-1}$ only. The reason for this lies in an increased structural robustness of the mixed-metal MOFs through better charge balance at the coordination bonded cluster. This opens interesting options for applications of mixed-metal CPM-37 and other less-stable MOFs. Derivatives of the CPM-37, α,β-$Ni(OH)_2$, γ-NiO(OH), and, plausibly, γ-FeO(OH), obtained by the MOF`s decomposition in the alkaline medium demonstrated potent electrocatalytic properties for the oxygen evolution reaction (OER), with the best OER activity being achieved by CPM-37(Ni_2Fe). This material boasted a small overpotential of 290 mV at 50 mA cm^{-2}, a low Tafel slope of 39 mV dec^{-1}, and a higher stability regarding OER than RuO_2 after 20 h chronopotentiometry at 50 mA cm^{-2}.

Porosity of the samples was studied by nitrogen sorption isotherms measured at 77 K (Figure 14a). All samples showed a type Ib isotherm, characteristic for microporous materials, although with very different porosities. The monometallic samples CPM-37(Ni) and CPM-37(Fe), which are most likely less stable than their bimetallic counterparts, show much lower porosities (87 and 368 $m^2\ g^{-1}$). The

bimetallic MOFs compare very favourable to this with their high surface areas of 2039 $m^2\ g^{-1}$ (CPM-37(Ni_2Fe)), 1955 $m^2\ g^{-1}$ (CPM-37 (NiFe)) and 2378 $m^2\ g^{-1}$ (CPM-37($NiFe_2$)).

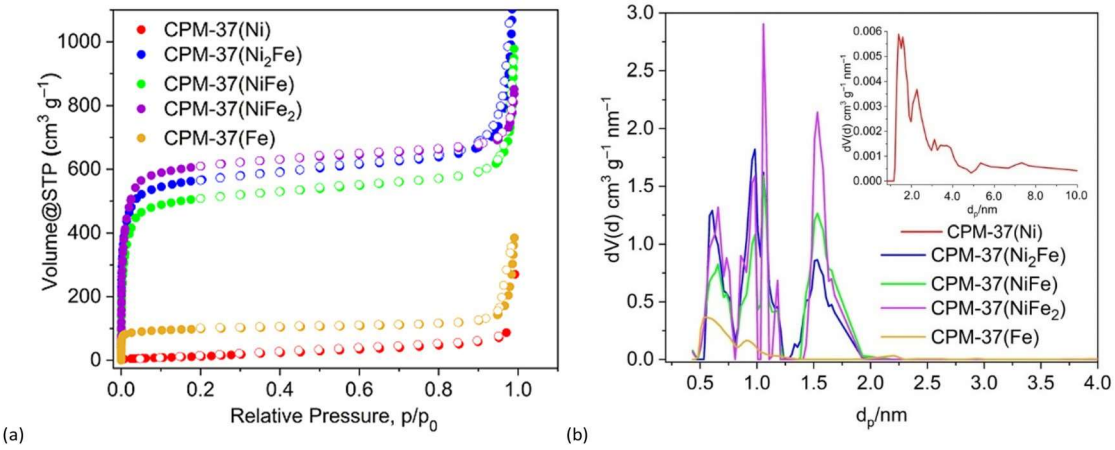

Figure 14: (a) Nitrogen adsorption isotherms of the CPM-37 samples at 77 K (adsorption: filled circles; desorption: empty circles), (b) NLDFT-based pore size distributions for the CPM-37 samples.

NLDFT calculations were undertaken to determine the pore size distributions and showed a trimodal distribution in the microporous range (Figure 14 b, 0.5-2.0 nm pore diameter). This contrasts with the expected unimodal distribution, possibly because the lack of proper DFT kernels for MOFs or because of defect formation. The one exception is CPM-37(Ni), which had a broad pore size distribution over the micro- and mesoporous range up to a diameter of 10 nm, attributed to a partial structural collapse during the activation process.

As expected from their surface areas, all bimetallic MOFs showed a much higher pore volume than the monometallic materials: 2.25, 1.50 and 1.30 $cm^3\ g^{-1}$ for CPM-37(Ni_2Fe), CPM-37(NiFe) and CPM-37($NiFe_2$) respectively, and only 0.11 and 0.58 $cm^3\ g^{-1}$ for CPM-37(Ni) and CPM-37(Fe).

3.3.12 Fluorinated vs. non-fluorinated tetrahedral Tri^4Tri^4 porous organic cages for H_2, CO_2, and CH_4 adsorption

David, T.; **Oestreich, R**.; Pausch, T.; Wada, Y.; Fleck-Kunde, T.; Kawano, M.; Janiak, C. & Schmidt, B. M. Fluorinated vs. non-fluorinated tetrahedral Tri^4Tri^4 porous organic cages for H_2, CO_2, and CH_4 adsorption

Chemical Communications, Royal Society of Chemistry (RSC), **2024**, 60, 14762-14765. DOI: 10.1039/D4CC05277C

Reprinted according to Creative Commons 3.0

Contributions to this publication:

- Proofreading of the manuscript
- Gas sorption measurements and evaluations
- PXRD measurements
- Discussion and input to further measurement methods

Two porous complementary tetrahedral Tri^4Tri^4 imine cages, one fluorinated, one non-fluorinated, were synthesized, with high Brunauer-Emmett- Teller (BET) surface areas of 591 $m^2 g^{-1}$ and 753 $m^2 g^{-1}$. They proved to be suitable for the adsorption of H_2, CO_2, and CH_4. The cages were compared regarding thermal stability, crystallinity, selectivity and porosity, and the results highlight the promising properties of fluorinated and non-fluorinated porous organic cages as functional materials.

Several gas isotherms were recorded for the characterization of both materials and especially to evaluate the differences between the fluorinated and non-fluorinated form. Before measurements the cages were activated under vacuum at 80 °C for Et^4F^4 and at 140 °C for Et^4H^4 overnight. After each measurements the samples were again heated to 80 °C under vacuum.
Nitrogen isotherms measured at 77 K (Figure 15) for both cages showed a type I behaviour in the low pressure region, characteristic for a microporous material, followed by the slow increase of nitrogen adsorption for higher pressures, typical of type II isotherms with multilayer condensation in macropores, presumably between particles. The large H4 hysteresis, with a distinct step at a relative pressure p/p_0 of 0.5, more pronounced in Et^4F^4, is most likely caused by two different ink bottle type pores. The BET surface areas were calculated to be 591 $m^2 g^{-1}$ for Et^4F^4 and 753 $m^2 g^{-1}$ for Et^4H^4, respectively. This was the highest surface area measured for tetrahedral Tri^4Tri^4 cages up to date. Total nitrogen uptake, measured at p/p_0 0.95, to avoid effects of condensation, was 14.5 mmol g^{-1} (28.9 wt. %) for Et^4H^4 and 10.1 mmol g^{-1} for Et^4F^4.

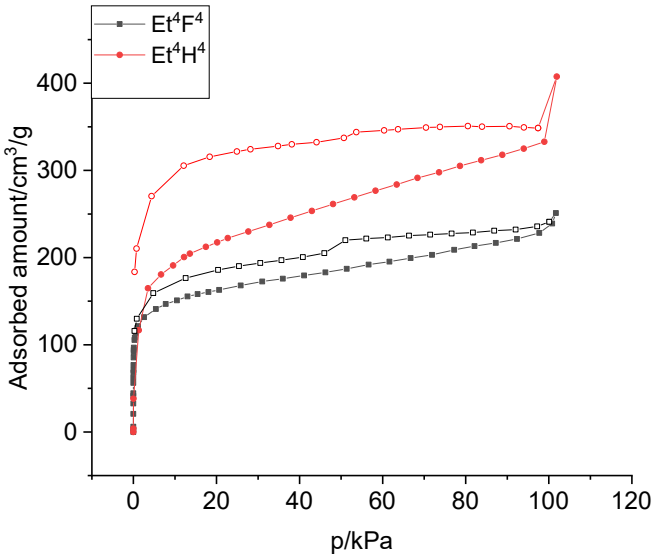

Figure 15: Nitrogen isotherms at 77 K for

Theoretical calculations by GCMC as well as by NLDFT were undertaken to determine the pore volumes, with GCMC, assuming cylindrical pore shape, giving the closest fit to the actual isotherms . Et^4F^4 was determined to have a total pore volume of 0.39 $cm^3\ g^{-1}$ and a micropore volume of 0.21 $cm^3\ g^{-1}$, while Et^4H^4 showed a total pore volume of 0.59 $cm^3\ g^{-1}$ and 0.24 $cm^3\ g^{-1}$. The pore size distribution of Et^4F^4 shows a narrow peak around 5.8 Å, in agreement with expectations from SC-XRD data (Figure 16). For Et^4H^4 a broader pore size distribution showed micropores centered on 14 Å and some larger mesopores between 20 and 80 Å, which would be larger than the cages themselves, indicating cracks in the material (Figure 17).

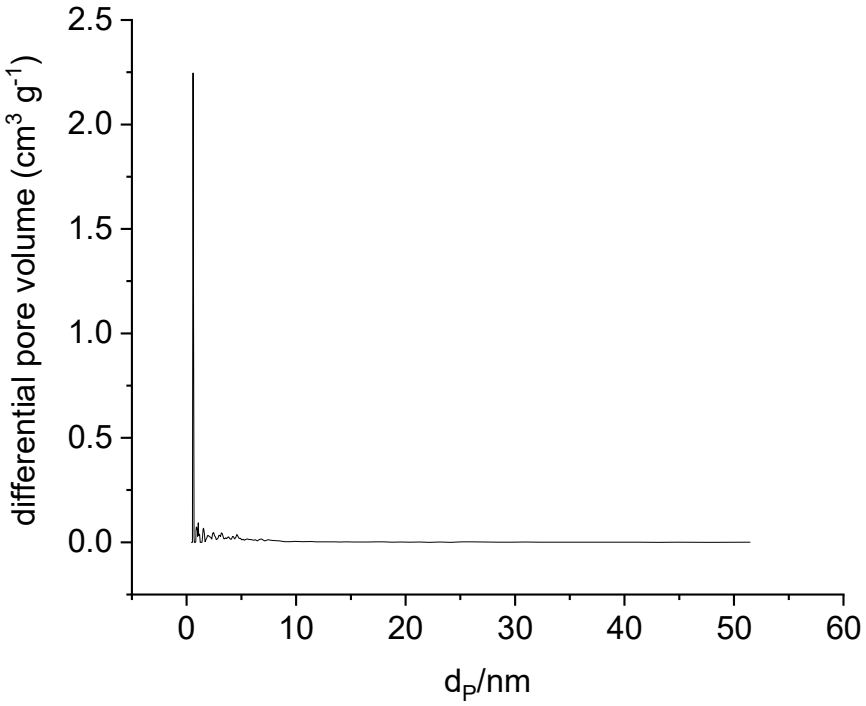

Figure 16: Grand canonical Monte Carlo (GCMC, cylindrical pore shape) pore size distribution of Et^4F^4

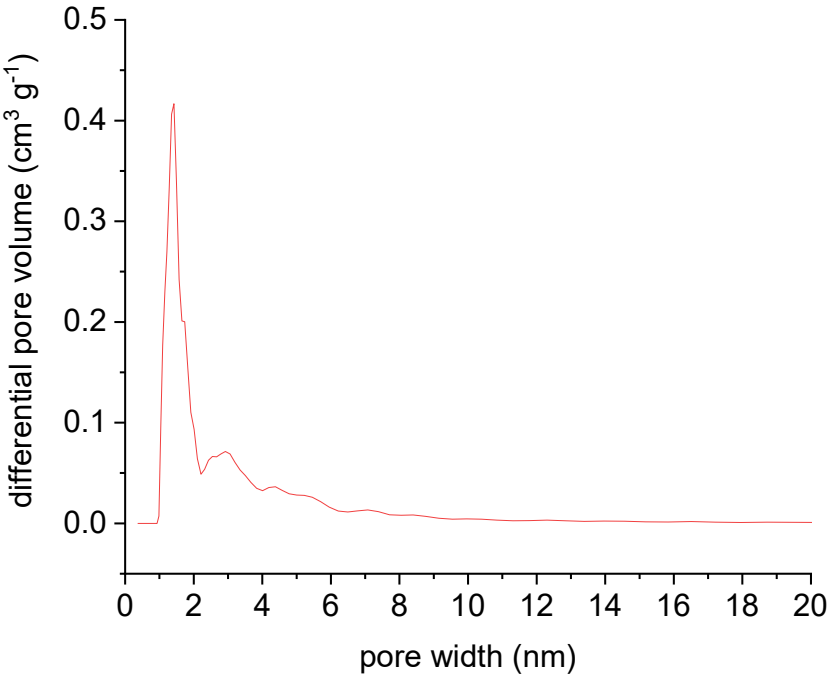

Figure 17: Grand canonical Monte Carlo (GCMC, cylindrical pore shape) pore size distribution of Et^4H^4

Since the small pores should make the cages suitable for separation processes, especially regarding gases with small molecules, hydrogen sorption isotherms were recorded at 77 K (Figure 18). Both cages show a good hydrogen adsorption of 6.1 mmol g^{-1} for Et^4H^4 and 3.9 mmol g^{-1} for Et^4F^4.

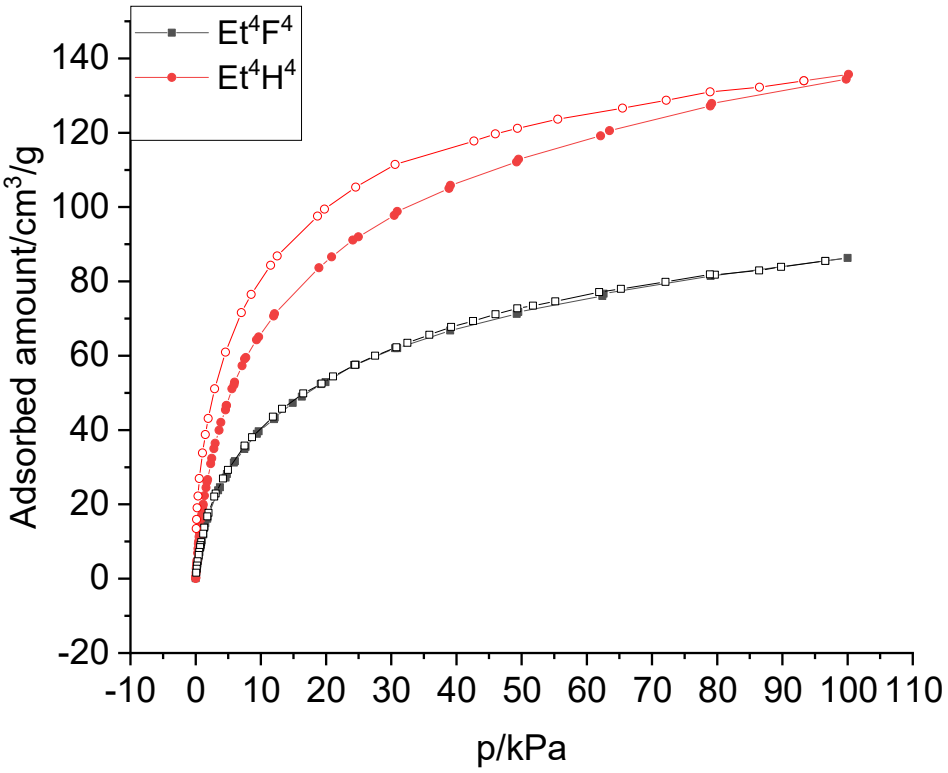

Figure 18: Hydrogen sorption isotherms measured at 77 K for Et^4H^4 and Et^4F^4

Both CO_2 and CH_4 adsorption isotherms were also measured for both cages at 273 K. The uptake for Et^4H^4 at 1 bar was 3.0 mmol g^{-1} for CO_2 and only 0.8 mmol g^{-1} for CH_4, higher than the amount adsorbed for Et^4F^4, 1.5 mmol g^{-1} (CO_2) and 0.4 mmol g^{-1} (CH_4) (Figure 19 and Figure 20). This is simply due to the higher pore volume available in Et^4H^4.

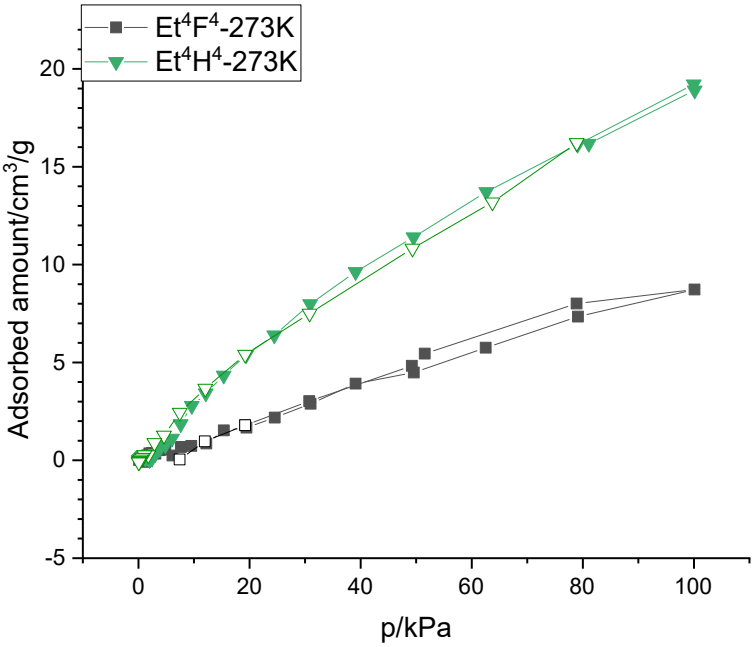

Figure 19: Methane isotherms measured at 273 K for Et^4H^4 (green) and Et^4F^4(black)

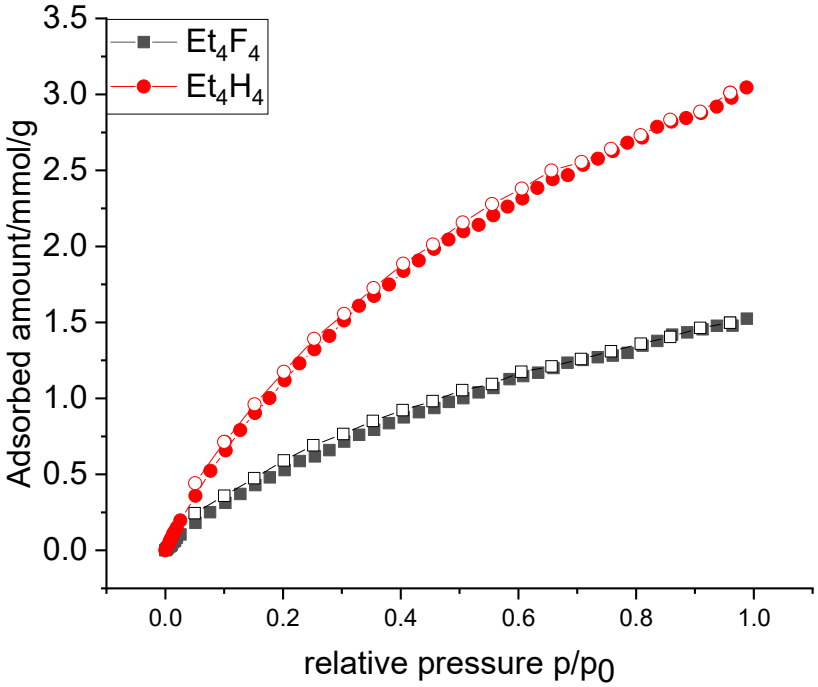

Figure 20: Carbon dioxide isotherms measured at 273 K for Et^4F^4 (black) *and* Et^4H^4 (red)

By setting the molar amount adsorbed in relation to the molar amounts of cage, derived from their mass, we could also estimate the gas molecules adsorbed per cage, which is also an interesting property to compare between materials. All values are recorded in Table 1, again with Et^4H^4 showing superior gas adsorption per cage unit. But both cages show a high loading compared to other cage materials.

*Table 1: Overview of the gas absorption properties at 1 bar of the non-fluorinated cage **Et^4H^4** and the fluorinated cage **Et^4F^4**.*

Gas	Et^4H^4			Et^4F^4		
	mmol/g	wt%	mol/mol	mmol/g	wt%	mol/mol
N_2[a]	14.50	28.89	33.98	10.05	21.96	32.23
N_2	18.18	33.75	42.61	11.20	23.88	35.92
H_2	6.05	1.21	14.19	3.85	0.77	12.35
CO_2 (273K)	3.05	11.82	7.14	1.52	6.28	4.89
CO_2 (293K)	1.84	7.49	4.31	0.79	3.37	2.54
CH_4 (273K)	0.84	1.34	1.98	0.39	0.62	1.25
CH_4 (293K)	0.43	0.69	1.02	0.13	0.21	0.42

[a] Values at 0.95 p/p_0 before macropore condensation starts.

Even more important than pure adsorption is the selectivity between gases for many applications. Therefore we calculated the selectivites for CO_2 over CH_4 using Ideal adsorbed solution theory (IAST), based on the sorption isotherms measured at 273 K (Figure 1Figure 21). At an equimolar mixture at 1 bar, both cages exhibit near identical selectivity for CO_2 over CH_4, 8.8 and 8.71 for Et^4H^4 and Et^4F^4, respectively. With decreasing carbon dioxide content the selectivity of Et^4H^4 decreases to 6.6 to a value of 6.6 at 95 % CH_4. In contrast, the selectivity of the fluorinated cages increases with the methane content, reaching 9.7 at the same point. Since flue gases usually contain a surplus of methane, higher selectivity for low carbon dioxide concentrations is preferable for many applications.

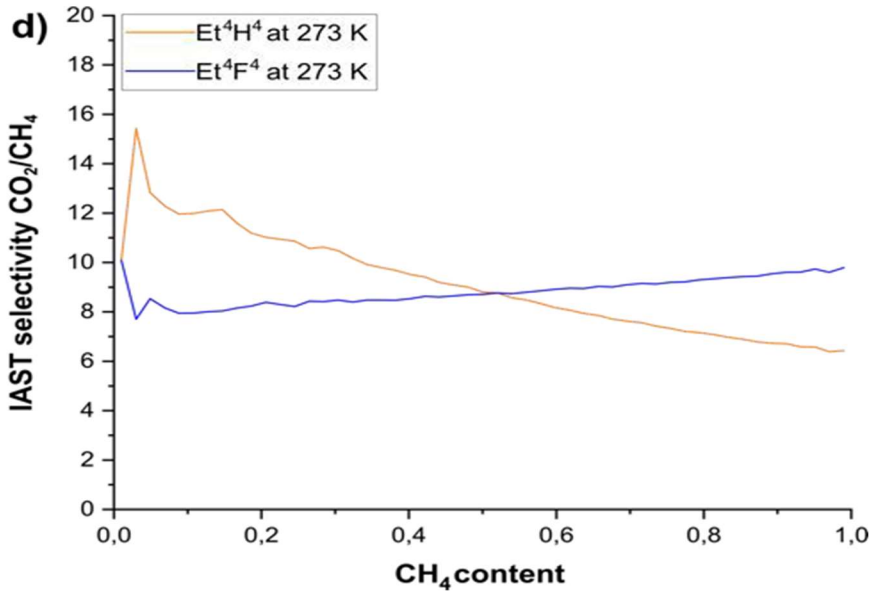

Figure 21: Selectivities of both cages for a CO_2/CH_4 mixture according to IAST at 1 bar and 273 K (orange Et^4H^4, blue Et^4F^4)

Via PXRD measurements the stability of both cages were tested before and after sorption measurements. Et^4F^4 showed higher crystallinity, which was retained after the sorption experiments, whereas Et^4H^4 showed only very broad peaks, characteristic of a largely amorphous material (Figure 22).

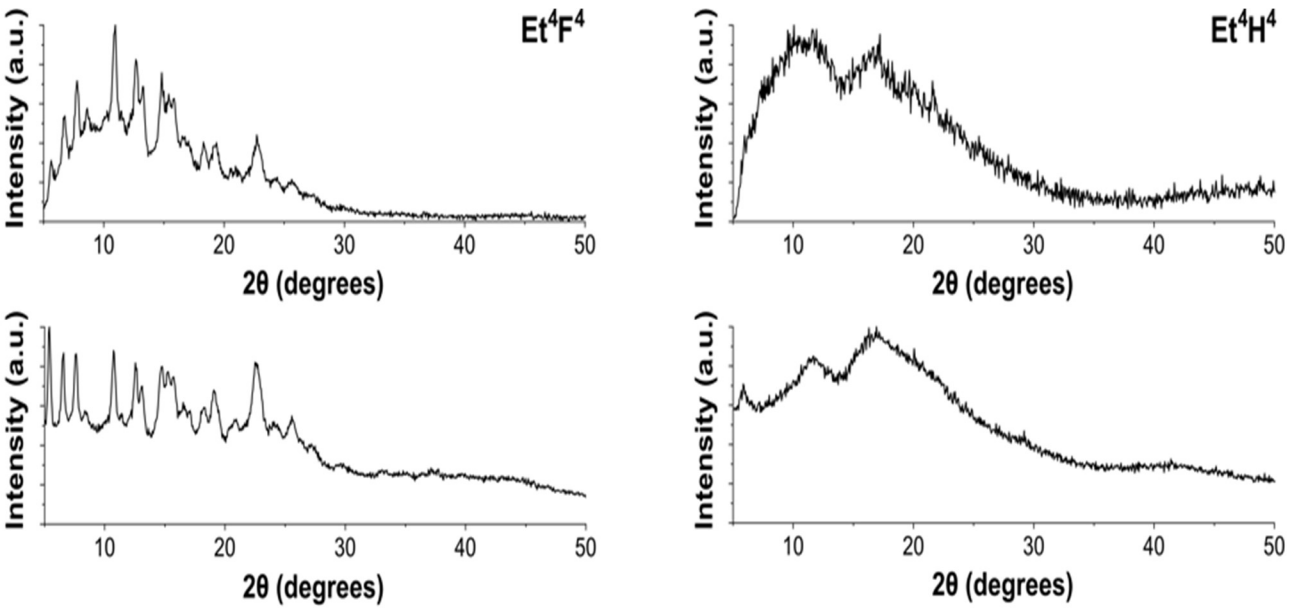

Figure 22: Powder patterns of Et^4F^4 and Et^4H^4before (top) and after (bottom) measurements

3.3.13 Metal–Organic Azolate Frameworks with an Acetylene-bis-pyrazolate Linker: Assessing the Role of the Triple-Bond Spacer in Gas and Vapor Sorption

Jordan, D. N.; Müller, T.; **Oestreich, R**.; Strothmann, T.; Boldog, I. & Janiak, C. Crystal Growth & Design, American Chemical Society (ACS), 2024, 24, 3837-3854. DOI: 10.1021/acs.cgd.4c00165

Contributions to this publication:

- Proofreading of the manuscript
- Gas sorption measurements and evaluations

The diprotonated linker precursor in the form of the salt [H4bpe2+](TFA−)2 (H2bpe = 1,2-bis(1H-pyrazol-4-yl)ethyne; HTFA = trifluoroacetic acid) with Zn(NO3)2· 4H2O in DMF reacted at 75 °C for 9 days to single crystals of the metal−organic framework (MOF) [Zn(bpe)]·1.8DMF (ortho-1· 1.8DMF) (HHUD-5). The crystals contain rhombic channels and show the orthorhombic space group. This is a polymorph of the previously reported structure of [Zn(bpe)]·1.2DMF (tetra-1·1.2DMF) which crystallizes in the tetragonal space group P42/mmc and forms square channels as shown in powder X-ray diffraction (PXRD) data. Microporous ortho-1 and tetra-1 have similar porosities and surface areas (pore

volumes) of 2135 m2/g (0.77 cm3/g at p/p0 = 0.95) and 1904 m2/g (0.73 cm3/g at p/p0 = 0.95) when an optimized activation is employed (only 1380 m2/g was reported previously for tetra-1).

Crystals of the MOF [Ni8(OH)4(H2O)2(bpe)6]·nSolv (2·nSolv, HHUD-6) in the cubic space group Fm3m were produced by the reaction of the boc-protected linker precursor Boc2bpe with Ni(OAc)2· 4H2O in DMF/water under reflux. Compound 2 is the newest member of the isoreticular series of [Ni8(OH)4(H2O)2L6] (L = bis-pyrazolate or carboxylate-pyrazolate) and exhibits a surface area of 1415 m2/g and a pore volume of 0.78 cm3/g at p/p0 = 0.80. The CO2 uptake at 273 K and 1 bar was 3.99 mmol/g for ortho-1 and 5.84 mmol/g for 2; the CH4 uptake was 1.11 mmol/g for ortho-1 and 1.64 mmol/g for 2, all in line with the higher heat of adsorption of the gases in 2, where open metal sites are possible after activation. Above 2 bar for CO2, and above 6 bar for CH4, the uptake in ortho-1 surpasses that in 2 due to the higher surface area of ortho-1. Both MOFs show high H2 uptakes of 11.6 mmol/g for ortho-1 and 8.7 mmol/g for 2 at 77 K and 1 bar. Comparison to the CO2, CH4, and H2 uptake in the analogous MOFs with the slightly longer 4,4′-(1,4- phenylene)bis(pyrazolate) linker (having phenylene instead of acetylene spacer) suggests an advantage of the −CΞC− triple bond. Vapor adsorption experiments with volatile organic compounds at 293 K for ortho-1 yielded uptakes of 8.2

mmol/g for benzene, 6.6 mmol/g for cyclohexane, and 5.7 mmol/g for n-hexane with type I isotherms. Compound 2 gave uptakes of 10.4 mmol/g for benzene, 10.7 mmol/g for cyclohexane, and 8.8 mmol/g for n-hexane with type II isotherms. Both MOFs are water stable as indicated by water vapor sorption and stability tests which also show a hydrophobicity of the bpe2− linker.

For both compounds, ortho-1 and 2, nitrogen isotherms were recorded at 77 K (Figure 23Figure 1). ortho-1 showed clear type I isotherm behaviour, while 2 began as a type I(a) isotherm and changed into type IV(a), indicating a mixture of micro- and mesopores. High BET surface areas (2135 and 1415 m2g-1) and pore volumes (0.77 and 0.78 cm3g-1) were calculated for ortho-1 and 2. No hysteresis was visible for ortho-1, but 2 had a small hysteresis in the high-pressure region, caused by the mesoporous part. Remarkable are the two steps in the isotherm of (ortho-1), which become clearly visible on a logarithmic of pressure and demonstrate the existence of two very discrete kinds of micropores and excellent crystallinity. Neither non-local density functional theory (NLDFT) nor grand canonical Monte Carlo simulations could give a good fit for the measured isotherms and were thus not usable to gather informations about the pore size distribution.

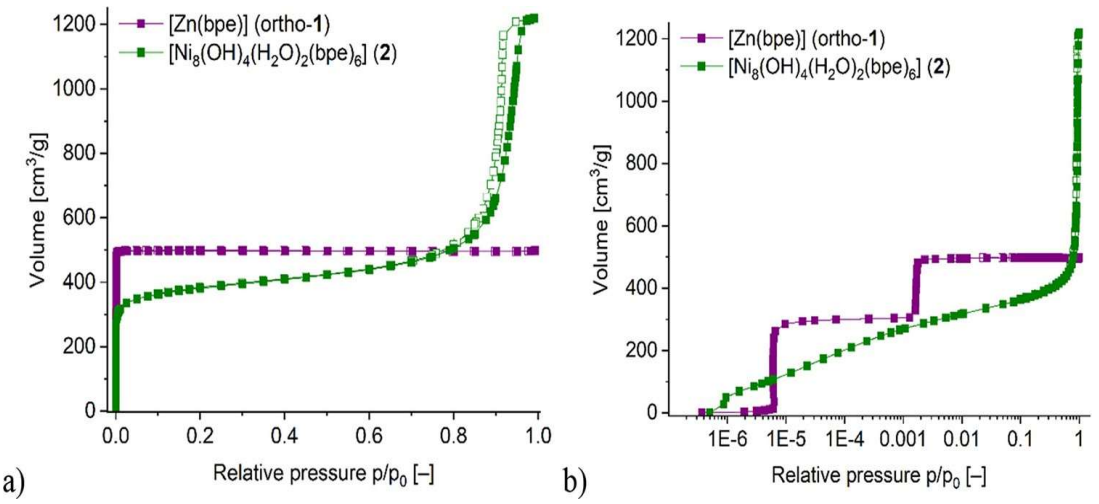

Figure 23: Nitrogen adsorption isotherms at 77 K of [Zn(bpe)] (ortho-1) and [Ni8(OH)4(H2O)2(bpe)6] (2) (a) using a linear pressure scale and (b) using a logarithmic pressure scale (filled symbols for adsorption, empty symbols for desorption)

Carbon dioxide (273 and 293 K), methane (273 and 293 K) and hydrogen isotherms were also recorded (Figure 24). Ortho-1 showed a CO2 uptake of 3.99 mmol/g at 273 K, compared to

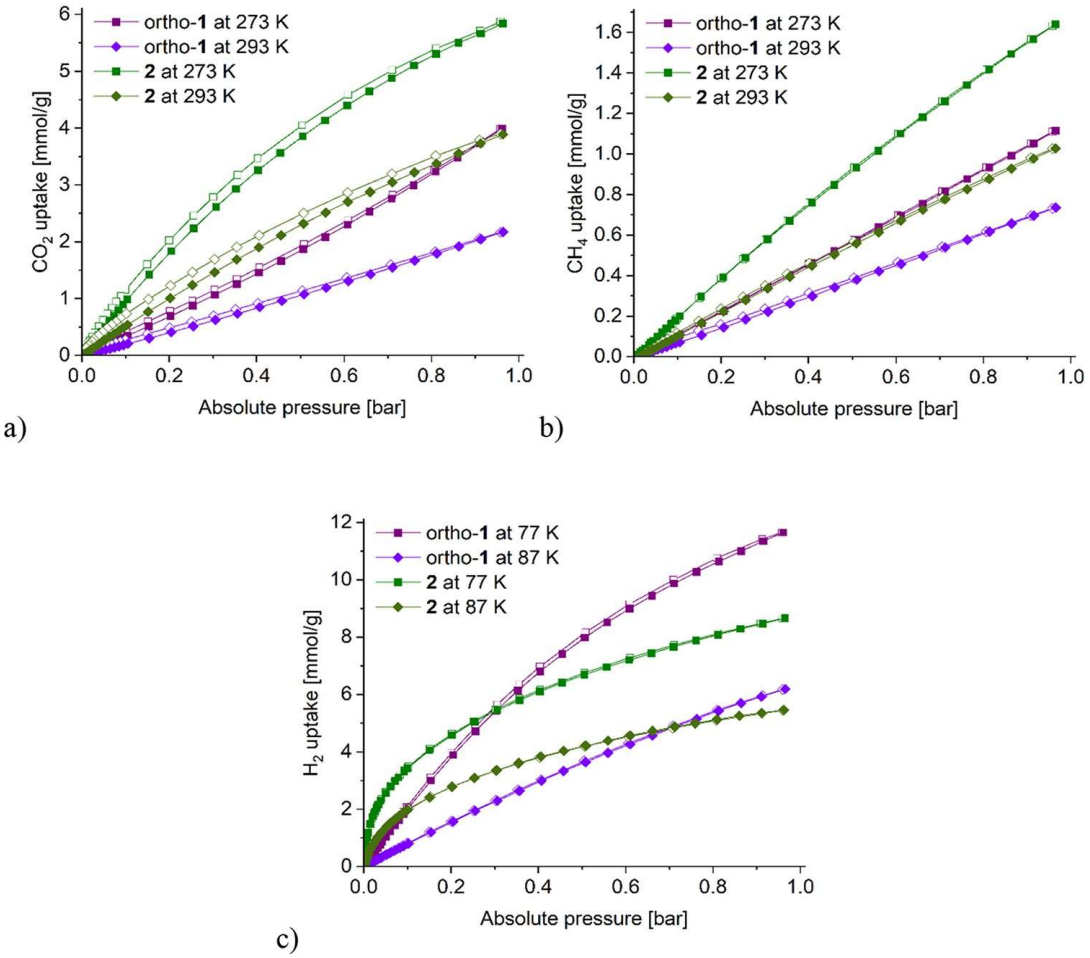

Figure 24: Gas sorption isotherms of [Zn(bpe)] (ortho-1) and $[Ni_8(OH)_4(H_2O)_2(bpe)_6]$ (2) for (a) CO_2 at 273 and 293 K, (b) CH_4 at 273 and 293 K and (c) H_2 at 77 and 87 K (filled symbols for adsorption, empty symbols for desorption)

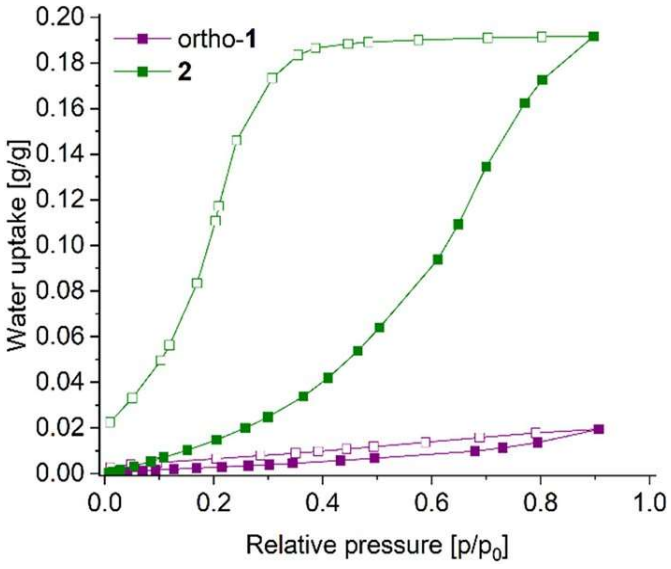

Figure 25: Water vapor sorption isotherm of [Zn(bpe)] (ortho-1) and $[Ni_8(OH)_4(H_2O)_2(bpe)_6]$ (2) at 293

K (filled symbol adsorption, empty symbols desorption)

3.3.14 Calix[4]arene@MIL-101 as host@MOF for cage-in-cage pore space partitioning for enhanced CO_2 separation and catalysis

Navid, S. S.; Hosseinzadeh, R.; Oestreich, R.; Abdpour, S.; Beglau, T. H. Y. & Janiak, C.

Calix[4]arene@MIL-101 as host@MOF for cage-in-cage pore space partitioning for enhanced CO_2 separation and catalysis

Journal of Materials Chemistry A, Royal Society of Chemistry (RSC), 2025, 13, 3894-3902. DOI: 10.1039/D4TA07357F

Contributions to this publication:

- Performance and evaluation of sorption measurements
- Computational evaluation of selectivities
- Revision of manuscript

Highly stable para-sulfonated calix[4]arene (SCA), a bowl-shaped macrocycle with intrinsic porosity, was incorporated by adsorption from solution into the spherical cavities of the micro-mesoporous metal-organic framework MIL-101(Cr). The pore space distribution in the MOF by polar functionalized macrocyclic molecules, which can also act as hosts, resulted in the Host@MOF composite material SCA@MIL-101, which exhibited a high affinity for CO2 without the usage of alkaline amino functionalities. The SCA@MIL-101-w materials with w = 5, 10, and 30 wt% SCA showed high stability (even in aqueous media, under non-basic conditions) and slow leaching kinetics due to the nearly matching size of SCA and the pore entrances of the MOF. Despite the smaller surface area and pore volume for w = 30 wt% SCA in MIL-101 (SBET = 1073 $m^2 g^{-1}$ and V_{pore} = 0.52 $cm^3 g^{-1}$) compared to MIL-101 (2660 $m^2 g^{-1}$ and 1.0 $cm^3 g^{-1}$), the pore-space partitioning approach enables an improvement in CO_2 absorption capacity to 103 $cm^3 g^{-1}$ for SCA@MIL-101-30 compared to MIL-101 with 66 $cm^3 g^{-1}$ (273 K and 1 bar). It also increases the CO_2 /N_2 selectivity, so that SCA@MIL-101-30 has an improved selectivity of 11 over the 4 reached by MIL-101 at 293 K and 1 bar for a 15 : 85 v:v mixture of carbon dioxide and nitrogen.

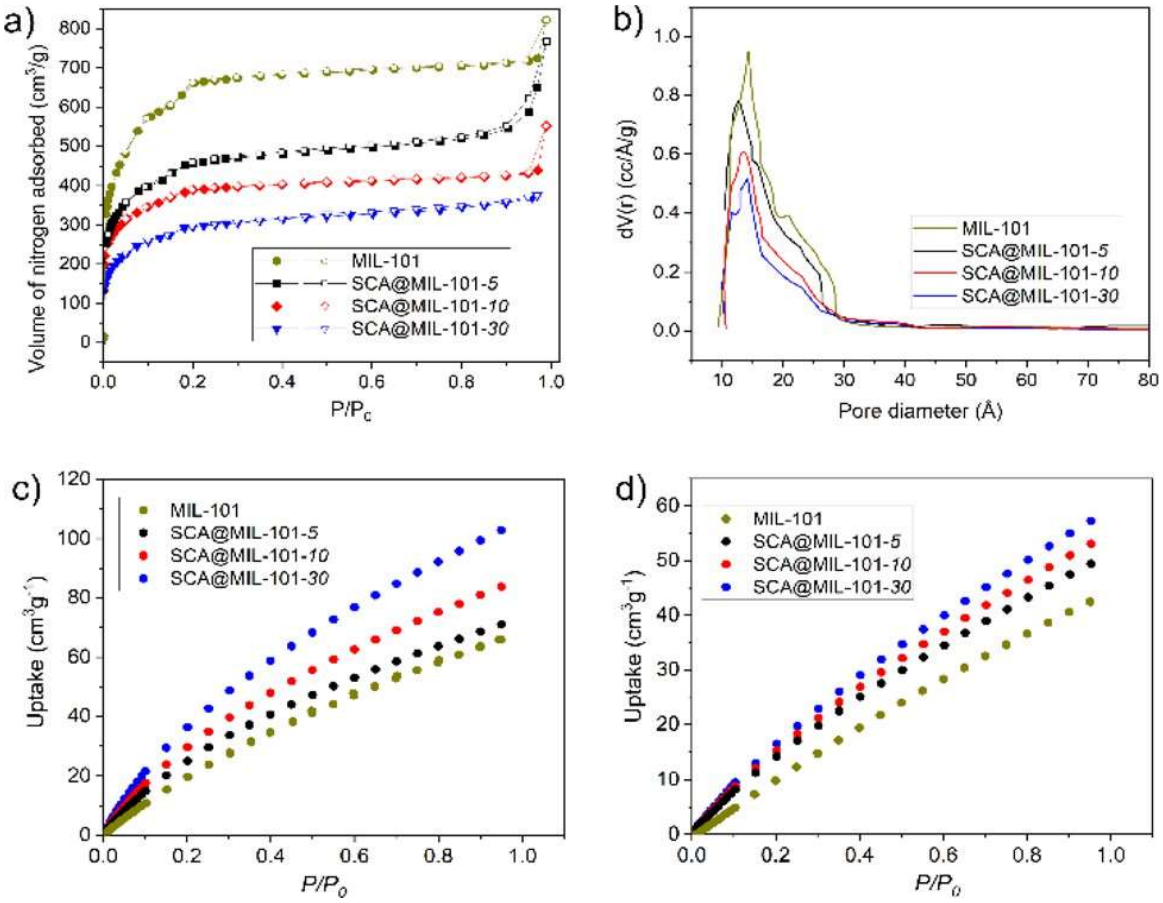

Figure 26: N_2 adsorption isotherms of MIL-101 and the derived SCA@MIL-101 composites at 77 K, (b) pore size distribution of all composites AND MIL-101, (c) and (d) CO_2 adsorption isotherms of SCA@MIL-101-w (($w = 5, 10, 30$), and MIL-101 measured up to 1 bar at 273 K and 293 K

3.3.15 NanoMOF-Based Multilevel Anti-Counterfeiting by a Combination of Visible and Invisible Photoluminescence and Conductivity

Maxeiner, M.; Maile, R.; Cuvalli, M.; Wolf, A.; Komal, A.; **Oestreich, R.**; Janiak, C.; Mandel, K.; Knebel, A. & Müller-Buschbaum, K.

NanoMOF-Based Multilevel Anti-Counterfeiting by a Combination of Visible and Invisible Photoluminescence and Conductivity

Advanced Functional Materials, Wiley, 2025. DOI: 10.1002/adfm.202500794

Reprinted according to Creative Commons 4.0

Contributions to this publication:

- Performance and evaluation of gas sorption measurements
- Revision of manuscript as coauthor

In this work multifunctional mixed matrix membranes (MMMs) and composite powders based on nanoscale metal-organic frameworks (nanoMOFs) were synthesized as highly sensitive reaction materials for multi-stage anti-counterfeiting based on reaction-stimulus. Composite materials based on nanoMOFs offer a wide range of applications as anti-counterfeiting markers due to their physicochemical properties. Nine materials are presented, consisting of nanoMOFs containing trivalent lanthanides ($[Ln_3(bdc)_{4,5}(H_2O)_3(dmf)_2]$ (nLn-bdc); bdc^{2-}=benzene-1,4-dicarboxylate; Ln=Eu, Tb, Yb) and the polymers polystyrene sulfonate, pyrolyzed resorcinol-formaldehyde, and polysulfone as matrices. These materials have inherently distinct properties, the combination of which enables the emission of visible and near-infrared light as well as specific conductivity for multi-level counterfeit protection. The developed anti-counterfeiting materials ensure that changing one feature inevitably affects other features by the additive and interdependent nature of their security features, thereby enhancing the overall integrity and resilience of the security mechanism. Even the jet-black composites made of nLn-bdc and pyrolyzed resorcinol-formaldehyde exhibit bright light emission in the near-infrared range when stimulated with UV light suitable for black materials.

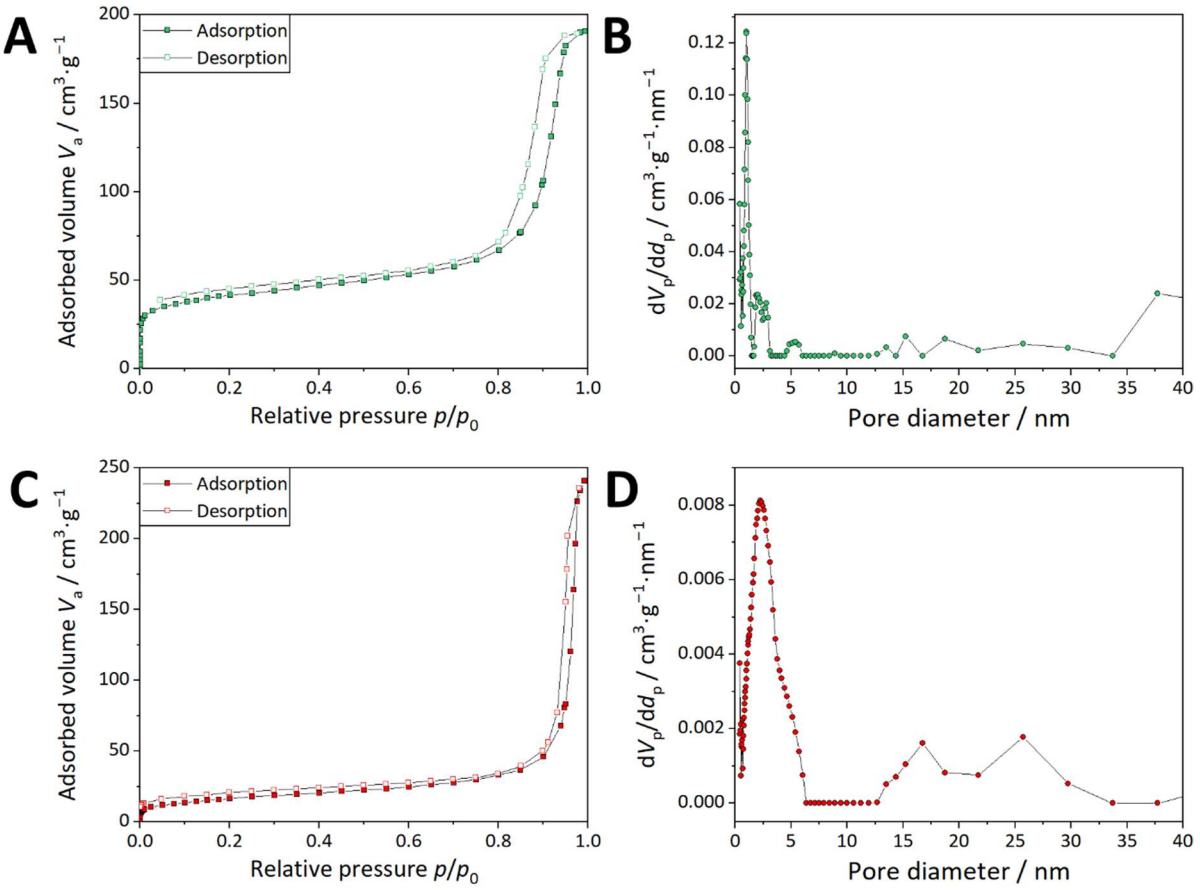

Figure 27: Nitrogen isotherms at 77 K and the derived pore size distribution of nTb-bdc (A,B) and nEu-bdc (C,D)

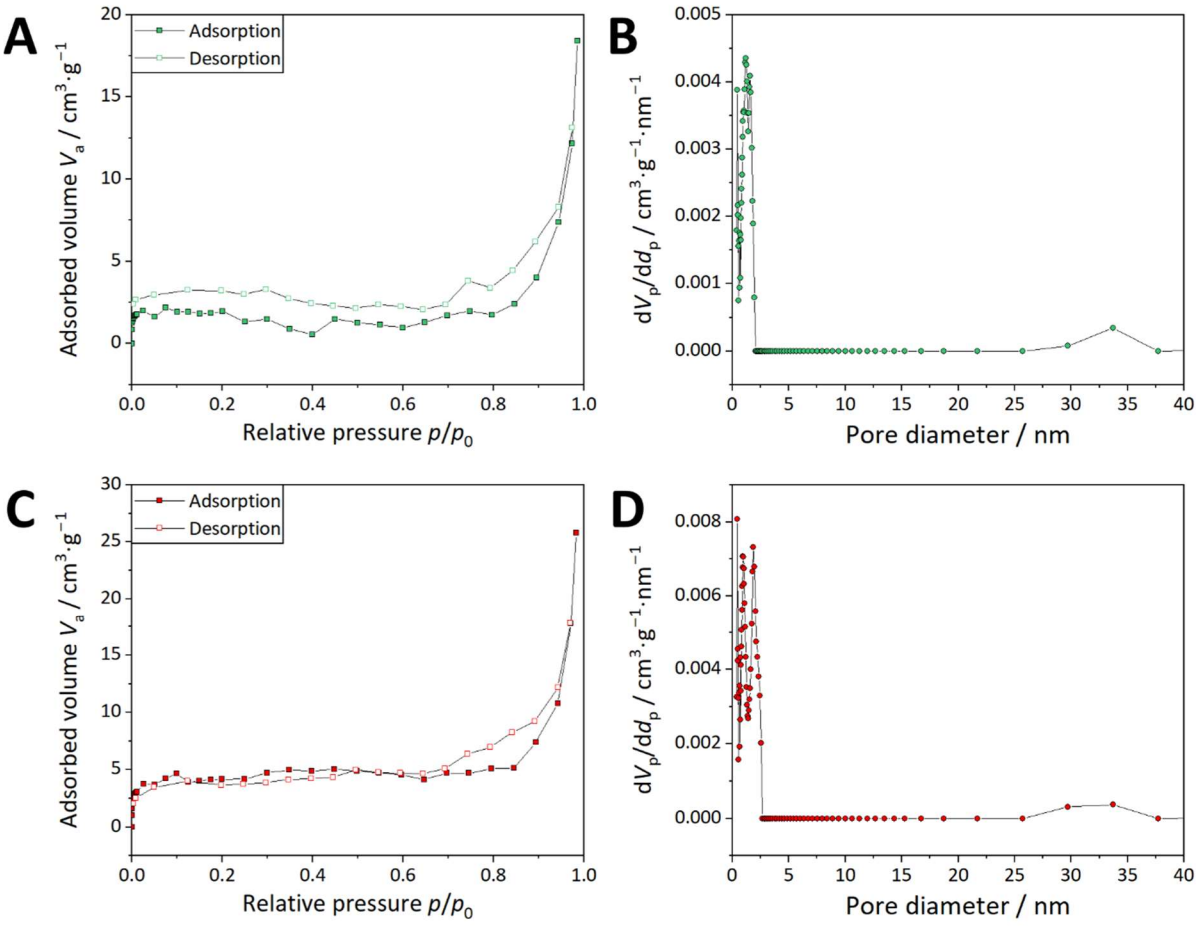

Figure 28: Nitrogen isotherms and pore size distribution of bulk Tb-bdc (A,B) and bulk Eu-bdc (C, D). Corrugation of isotherms is caused by the low adsorption values

3.3.16 Carbon dioxide adsorption properties in 3D ultramicroporous diamondoid lanthanide-oxalate frameworks

Khotchasanthong, K.; Wannarit, N.; Díaz Torres, R.; Arayachukiat, S.; Kielar, F.; Dungkaew, W.; Rungtaweevoranit, B.; Kheawhom, S.; **Oestreich, R.**; Janiak, C. & Chainok, K.

Journal of Materials Chemistry A, Royal Society of Chemistry (RSC), 2025, 13, 36091-36103

Reprint with permission from reference [42] © Royal Society of Chemistry

Contributions to this publication:

- Support with measurement and evaluation of isotherms

Two series of three-dimensional (3D) lanthanide-based MOFs (LnMOFs), namely $(Me_2NH_2)[Ln(C_2O_4)_2(H_2O)]*3H_2O$ (1Ln; Ln=Ce, Pr, Nd, Sm, Eu, Gd, Tb, Dy, Er) and $(Me_2NH_2)[Ln(C_2O_4)_2]H_2O$ (2Ln; Ln = Tm, Yb, Lu), were synthesized, with careful regulation of the ultramicropores to match the kinetic diameters of polarized CO_2 molecules. The coordination geometries $\{LnO_9\}$ in 1Ln and $\{LnO_8\}$ in 2Ln are linked by bidentate oxalate ligands ($C_2O_4^{2-}$) to form

diamond-like (dia) anionic frameworks containing charge-balancing dimethylammonium cations (Me2NH2+) in ultramicroporous channels. The removal and readsorption of water facilitates the transition between the crystal structures of 1Ln and 2Ln, resulting in changes in the coordination number and geometry of the metal centers. At cryogenic temperatures and ambient pressure, the tailor-made ultramicroporosity facilitates a sieving effect in LnMOFs, resulting in increased CO_2 uptake compared to N_2, CH_4, and Ar, as shown by the examples of 1Gd, 1Er, and 2Yb. Furthermore, investigations of CO_2 sorption at higher pressure for 1Gd and 2Yb show steep S-shaped adsorption-desorption isotherms characterized by hysteresis. In situ investigations using diffuse reflection infrared Fourier transform spectroscopy (DRIFTS) show, that this phenomenon is due to the formation of dimethylcarbamic acid, which results from the chemisorption of guest Me_2NH+ cations and carbon dioxide.

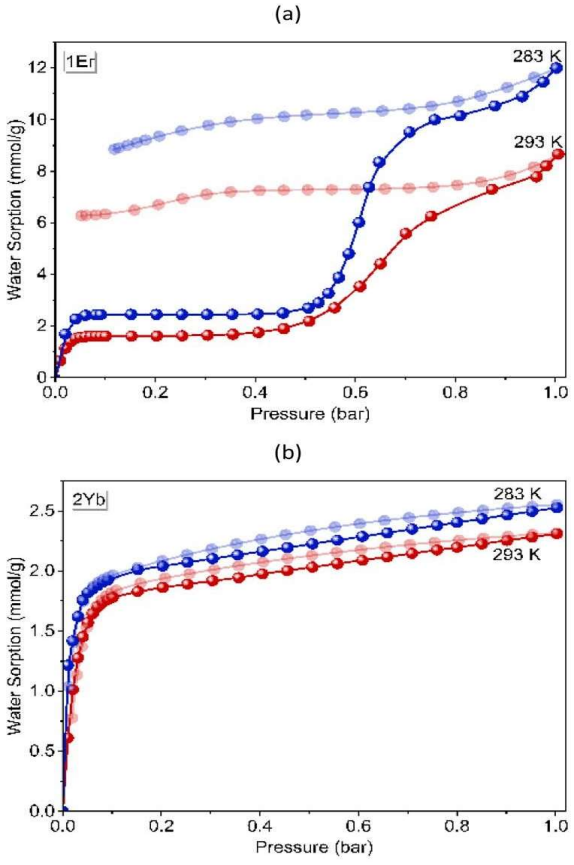

Figure 29 Water sorption isotherms at 283 and 293 K for (a) 1Er and (b) 2Yb.

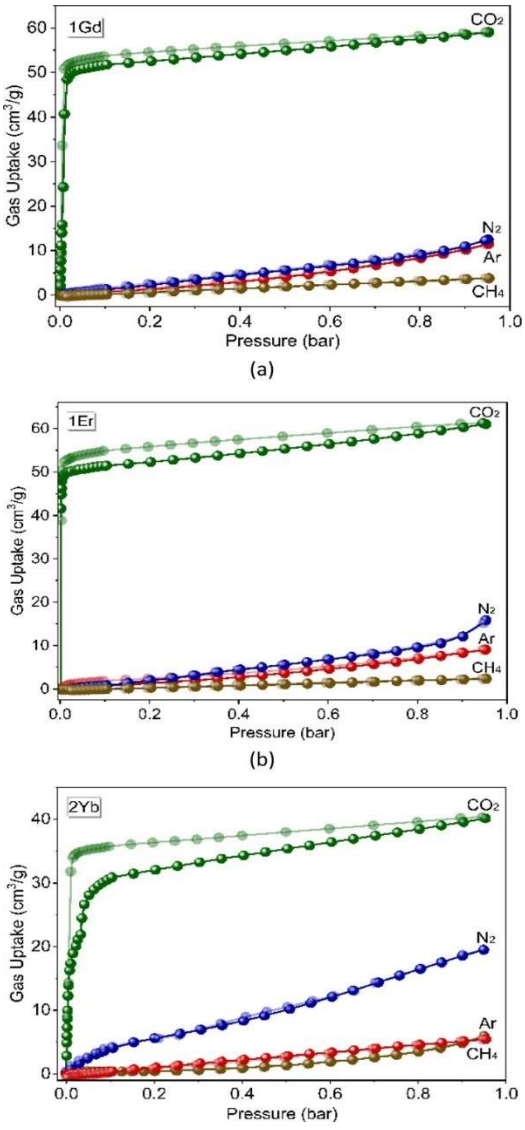

Figure 30 Adsorption (darker coloured spheres) and desorption (lighter- coloured spheres) isotherms for CO_2 (195 K), N_2 (77 K), Ar (87 K), and CH_4 (273 K) in (a) 1Gd, (b) 1Er, and (c) 2Yb.

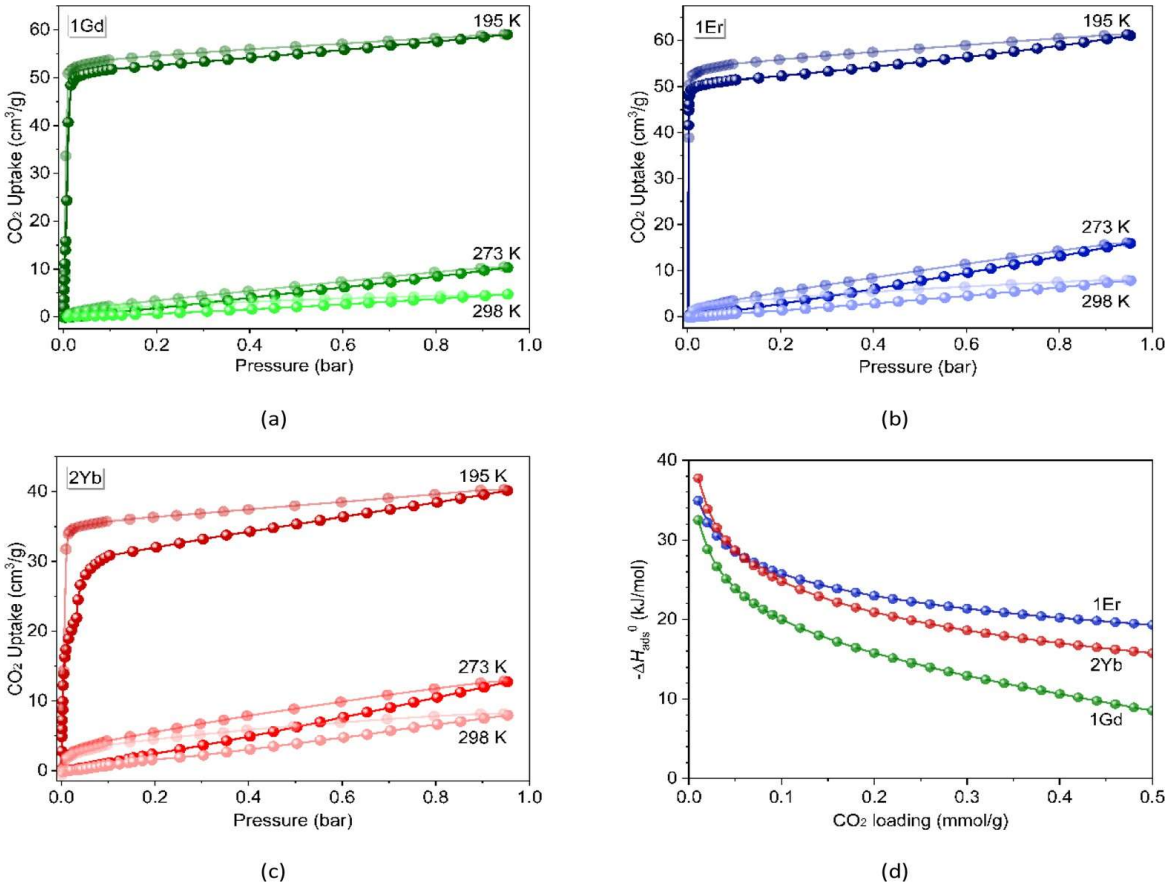

Figure 31: CO_2 adsorption (darker coloured spheres)–desorption (lighter-coloured spheres) isotherms at temperatures of 195, 273, and 298 K for (a) 1Gd, (b) 1Er, and (c) 2Yb. (d) The isosteric heat of adsorption for 1Gd, 1Er, and 2Yb, calculated from the CO_2 isotherm data obtained at 273 and 298 K.

5. Devices and measurement parameters

5. 1. Powder X-ray diffractometry (PXRD)

Powder diffractograms were measured at room temperature with a Bruker D2 Phaser (300 W, 30 kV, 10 mA) with Cu-Kα-radiation (λ = 1.541826 Å) and a scanning rate of 0.0125 °/s. Single crystal silica sample holders were used. The most intensive reflexes were normalized on a value of 1.

5.2. Sorption measurements

Sorption measurements were performed on a variety of instruments. The list includes the Autosorb-6iSA by Quantachrome, the Nova, the Quantachrome Autosorb IQ MP automatic adsorption analyzer, the 3P and the BELSORP-max II (*MicrotracBEL Corporation*), with the main part of the work conducted on that last one.

Temperature was regulated via liquid nitrogen (77 K), Julabo-Corio or Julabo Dyneo and an ethylene glycol water mixture (263 to 323 K) or a CTI Cryogenics Cryodine Refrigerator, CTI Cryogenics 8200 Compressor and a LakeShore Cryogenics temperature controller (87 or 195 K).

Evaluation was performed with the programs ASwin by Quantachrome, BELMaster Version 7.4.3.1 by

Microtrac and 3P sim by 3P instruments.

All gases had a purity of at least 99.995 %.

5.3. Scanning electron microscopy (SEM)

SEM pictures were recorded with the JSM-6510LV device by Jeol, using tungsten- and LaB_6 cathode

5.4 Thermogravimetric analysis (TGA)

Thermogravimetric analysis was conducted on a TG Tarsus 209 F3 by Netzsch.

5.5. Transmission electron microscopy (TEM)

TEM pictures were recorded with a FEI Tecnai G2 F20 or a CM20 by Philips. Measurements were performed with an acceleration voltage of 200 kV. Analysis was performed with Digital Micrograph.

5.6. Nuclear magnetic resonance (NMR)

NMR spectra were recorded with an Avance-III-600, Bruker Avance DRX-500 or a Bruker Avance III-300 spectrometer

5.7. Infrared spectroscopy (IR)

IR-spectra were recorded on a Bruker Tensor 37 IR and measured with an ATR cell or in solvent with a cuvette with KBr-window between 4000 – 600 cm^{-1} .

Literature

[1] C. Janiak und J. K. Vieth, „MOFs, MILs and more: concepts, properties and applications for porous coordination networks (PCNs),“ *New Journal of Chemistry,* Bd. 34, p. 2366, 2010.

[2] C. Janiak, „Engineering coordination polymers towards applications,“ *Dalton Transactions,* p. 2781, 2003.

[3] M. O'Keeffe, „Design of MOFs and intellectual content in reticular chemistry: a personal view,“ *Chemical Society Reviews,* Bd. 38, p. 1215, 2009.

[4] S. L. James, „Metal-organic frameworks,“ *Chemical Society Reviews,* Bd. 32, p. 276, 2003.

[5] „SciFinder,“ November 2025. [Online]. Available: https://scifinder-n.cas.org/. [Zugriff am 14 November 2025].

[6] C. Gao, S. Liu, L. Xie, C. Sun, J. Cao, Y. Ren, D. Feng und Z. Su, „Rational design microporous pillared-layer frameworks: syntheses, structures and gas sorption

properties," *CrystEngComm,* Bd. 11, p. 177–182, 2009.

[7] K. Li, J. Lee, D. H. Olson, T. J. Emge, W. Bi, M. J. Eibling und J. Li, „Unique gas and hydrocarbon adsorption in a highly porous metal-organic framework made of extended aliphatic ligands," *Chemical Communications,* p. 6123, 2008.

[8] J.-R. Li, R. J. Kuppler und H.-C. Zhou, „Selective gas adsorption and separation in metal-organic frameworks," *Chemical Society Reviews,* Bd. 38, p. 1477, 2009.

[9] J. Graetz, „New approaches to hydrogen storage," *Chem. Soc. Rev.,* Bd. 38, p. 73–82, 2009.

[10] U. Mueller, M. Schubert, F. Teich, H. Puetter, K. Schierle-Arndt und J. Pastré, „Metal-organic frameworks—prospective industrial applications," *J. Mater. Chem.,* Bd. 16, p. 626–636, 2006.

[11] G. Férey, „Some suggested perspectives for multifunctional hybrid porous solids," *Dalton Transactions,* p. 4400, 2009.

[12] A. P. Côté, A. I. Benin, N. W. Ockwig, M. O'Keeffe, A. J. Matzger und O. M. Yaghi, „Porous, Crystalline, Covalent Organic Frameworks," *Science,* Bd. 310, p. 1166–1170, November 2005.

[13] R.-B. Lin, Y. He, P. Li, H. Wang, W. Zhou und B. Chen, „Multifunctional porous hydrogen-bonded organic framework materials," *Chemical Society Reviews,* Bd. 48, p. 1362–1389, 2019.

[14] S.-L. Cai, Y.-B. Zhang, A. B. Pun, B. He, J. Yang, F. M. Toma, I. D. Sharp, O. M. Yaghi, J. Fan, S.-R. Zheng, W.-G. Zhang und Y. Liu, „Tunable electrical conductivity in oriented thin films of tetrathiafulvalene-based covalent organic framework," *Chem. Sci.,* Bd. 5, p. 4693–4700, 2014.

[15] C. J. Doonan, D. J. Tranchemontagne, T. G. Glover, J. R. Hunt und O. M. Yaghi, „Exceptional ammonia uptake by a covalent organic framework," *Nature Chemistry,* Bd. 2, p. 235–238, February 2010.

[16] H. Furukawa, F. Gándara, Y.-B. Zhang, J. Jiang, W. L. Queen, M. R. Hudson und O. M. Yaghi, „Water Adsorption in Porous Metal–Organic Frameworks and Related Materials," *Journal of the American Chemical Society,* Bd. 136, p. 4369–4381, March 2014.

[17] E. Klontzas, E. Tylianakis und G. E. Froudakis, „Designing 3D COFs with Enhanced Hydrogen Storage Capacity," *Nano Letters,* Bd. 10, p. 452–454, January 2010.

[18] S. Liu, L. Yao, Y. Lu, X. Hua, J. Liu, Z. Yang, H. Wei und Y. Mai, „All-organic covalent organic framework/polyaniline composites as stable electrode for high-performance supercapacitors," *Materials Letters,* Bd. 236, p. 354–357, February 2019.

[19] S. S. Han, H. Furukawa, O. M. Yaghi und W. A. Goddard, „Covalent Organic Frameworks as Exceptional Hydrogen Storage Materials," *Journal of the American Chemical Society,* Bd. 130, p. 11580–11581, August 2008.

[20] M. Thommes, „Physisorption of gases, with special reference to the evaluation of surface area and pore size distribution (IUPAC Technical Report)," *Pure and Applied Chemistry, Walter de Gruyter GmbH,* pp. 87, 1051-1069, 2015.

[21] K. S. W. Sing, „Reporting physisorption data for gas/solid systems with special reference to the determination of surface area and porosity (Recommendations 1984)," *Pure and Applied Chemistry,* Bd. 57, p. 603–619, January 1985.

[22] M. Thommes, K. Kaneko, A. V. Neimark, J. P. Olivier, F. Rodriguez-Reinoso, J. Rouquerol und K. S. W. Sing, „Physisorption of gases, with special reference to the evaluation of surface area and pore size distribution (IUPAC Technical Report)," *Pure and Applied Chemistry,* Bd. 87, p. 1051–1069, July 2015.

[23] S. Lowell, J. E. Shields, M. A. Thomas und M. Thommes, Characterization of Porous Solids and Powders: Surface Area, Pore Size and Density, Springer Netherlands, 2004.

[24] M. Thommes und K. A. Cychosz, „Physical adsorption characterization of nanoporous materials: progress and challenges," *Adsorption,* Bd. 20, p. 233–250, February 2014.

[25] J. Landers, G. Y. Gor und A. V. Neimark, „Density functional theory methods for characterization of porous materials," *Colloids and Surfaces A: Physicochemical and Engineering Aspects,* Bd. 437, p. 3–32, November 2013.

[26] F. Rouquerol, J. Rouquerol, K. S. W. Sing, P. Llewellyn und G. Maurin, Adsorption by Powders and Porous Solids, Elsevier, 2014.

[27] S. Brunauer, P. H. Emmett und E. Teller, „Adsorption of Gases in Multimolecular Layers," *Journal of the American Chemical Society,* Bd. 60, p. 309–319, February 1938.

[28] P. Tarazona und R. Evans, „A simple density functional theory for inhomogeneous liquids: Wetting by gas at a solid-liquid interface," *Molecular Physics,* Bd. 52, p. 847–857, July 1984.

[29] P. Tarazona, „Free-energy density functional for hard spheres," *Physical Review A,* Bd. 31, p. 2672–2679, April 1985.

[30] C. Lastoskie, K. E. Gubbins und N. Quirke, „Pore size distribution analysis of microporous carbons: a density functional theory approach," *The Journal of Physical Chemistry,* Bd. 97, p. 4786–4796, May 1993.

[31] C. Lastoskie, K. E. Gubbins und N. Quirke, „Pore size heterogeneity and the carbon slit pore: a density functional theory model," *Langmuir,* Bd. 9, p. 2693–2702, October 1993.

[32] J. P. Olivier, „Modeling physical adsorption on porous and nonporous solids using density functional theory," *Journal of Porous Materials,* Bd. 2, p. 9–17, July 1995.

[33] S. Watanabe, H. Sugiyama, H. Adachi, H. Tanaka und M. T. Miyahara, „Free energy analysis for adsorption-induced lattice transition of flexible coordination framework," *The Journal of Chemical Physics,* Bd. 130, April 2009.

[34] H. Pan, J. A. Ritter und P. B. Balbuena, „Examination of the Approximations Used in Determining the Isosteric Heat of Adsorption from the Clausius−Clapeyron Equation," *Langmuir,* Bd. 14, p. 6323–6327, September 1998.

[35] J. Tóth, „Uniform interpretation of gas/solid adsorption," *Advances in Colloid and Interface Science,* Bd. 55, p. 1–239, March 1995.

[36] A. L. Myers und J. M. Prausnitz, „Thermodynamics of mixed-gas adsorption," *AIChE Journal,* Bd. 11, p. 121–127, January 1965.

[37] K. S. Walton und D. S. Sholl, „Predicting multicomponent adsorption: 50 years of the ideal adsorbed solution theory," *AIChE Journal,* Bd. 61, p. 2757–2762, August 2015.

[38] V. Goetz, O. Pupier und A. Guillot, „Carbon dioxide-methane mixture adsorption on activated carbon," *Adsorption,* Bd. 12, p. 55–63, January 2006.

[39] E. Richter, S. Wilfried und A. L. Myers, „Effect of adsorption equation on prediction of multicomponent adsorption equilibria by the ideal adsorbed solution theory," *Chemical Engineering Science,* Bd. 44, p. 1609–1616, 1989.

[40] A. A. Apostol, R. Oestreich, C. Maxim, C. Romanitan, M. Badea, C. Janiak und M. Andruh, „Nano-Sized Channels Resulting from the Packing of Discrete 3d–4f Metal Complexes in Crystals," *Crystal Growth & Design,* Bd. 23, p. 3740–3746, March 2023.

[41] D. N. Jordan, T. Müller, R. Oestreich, T. Strothmann, I. Boldog und C. Janiak, „Metal-Organic Azolate Frameworks with an Acetylene-bis-pyrazolate Linker: Assessing the Role of the Triple-Bond Spacer in Gas and Vapor Sorption," *Crystal Growth & Design,* Bd. 24, p. 3837–3854, April 2024.

[42] K. Khotchasanthong, N. Wannarit, R. Díaz Torres, S. Arayachukiat, F. Kielar, W. Dungkaew, B. Rungtaweevoranit, S. Kheawhom, R. Oestreich, C. Janiak und K. Chainok, „Carbon dioxide adsorption properties in 3D ultramicroporous diamondoid lanthanide-oxalate frameworks," *Journal of Materials Chemistry A,* Bd. 13, p. 36091–36103, 2025.

[43] K. Xu, R. Oestreich, T. Haj Hassani Sohi, M. Lounasvuori, J. G. A. Ruthes, Y. Zorlu, J. Michalski, P. Seiffert, T. Strothmann, P. Tholen, A. Ozgur Yazaydin, M. Suta, V. Presser, T. Petit, C. Janiak, J. Beckmann, J. Schmedt auf der Günne und G. Yücesan, „Polyphosphonate covalent organic frameworks," *Nature Communications,* Bd. 15, September 2024.

[44] D. Woschko, S. Millan, M.-A. Ceyran, R. Oestreich und C. Janiak, „Synthesis of a Chiral 3,6T22-Zn-MOF with a T-Shaped Bifunctional Pyrazole-Isophthalate Ligand Following the Principles of the Supramolecular Building Layer Approach," *Molecules,* Bd. 27, p. 5374, August 2022.

[45] D. Woschko, S. Yilmaz, C. Jansen, A. Spieß, R. Oestreich, T. J. M. M. Ntep und C. Janiak, „Enhanced sorption in an indium-acetylenedicarboxylate octahedra," *Dalton Transactions,* Bd. 52, p. 977–989, 2023.

[46] R. Oestreich, M. N. A. Fetzer, Y. Zhang, A. Schreiber, A. Knebel, M. Suta, C. Janiak, G. Hanna und G. Yücesan, „Stable Ultramicroporous Metal-Organic Framework with Hydrophilic and Hydrophobic Domains for Selective Gas Adsorption," *Angewandte Chemie International Edition,* Bd. 64, August 2025.

[47] S. S. Navid, R. Hosseinzadeh, R. Oestreich, S. Abdpour, T. H. Y. Beglau und C. Janiak, „Calix[4]arene@MIL-101 as host@MOF for cage-in-cage pore space partitioning for enhanced CO2 separation and catalysis," *Journal of Materials Chemistry A,* Bd. 13, p. 3894–3902, 2025.

[48] B. H. Monjezi, B. Sapotta, S. Moulai, J. Zhang, R. Oestreich, B. P. Ladewig, K. Müller-Buschbaum, C. Janiak, T. Hashem und A. Knebel, „Metal-Organic Framework {MIL}-68(In)-{NH} on the Membrane Test Bench for Dye Removal and~Carbon Capture," *Chemie Ingenieur Technik,* Bd. 94, p. 135–144, January 2022.

[49] M. Maxeiner, R. Maile, M. Cuvalli, A. Wolf, A. Komal, R. Oestreich, C. Janiak, K. Mandel, A. Knebel und K. Müller-Buschbaum, „NanoMOF-Based Multilevel Anti-Counterfeiting by a Combination of Visible and Invisible Photoluminescence and Conductivity," *Advanced Functional Materials,* April 2025.

[50] Y. Lu, Y.-X. Liu, Y. Wang, R. Oestreich, Z.-Y. Xu, W. Zhang, P. Hügenell, C. Janiak und X.-Y. Yang, „A facile spray-pressing synthesis approach for reusable photothermal masks," *iScience,* Bd. 26, p. 107286, August 2023.

[51] Z. M. Hassan, W. Guo, A. Welle, R. Oestreich, C. Janiak und E. Redel, „Formation of Gold Nanoclusters from Goldcarbonyl Chloride inside the Metal-Organic Framework HKUST-1," *Molecules,* Bd. 28, p. 2716, March 2023.

[52] V. Gvilava, M. Vieten, R. Oestreich, D. Woschko, M. Steinert, I. Boldog, R. Bulánek, N. A. Fokina, P. R. Schreiner und C. Janiak, „A diamantane-4,9-dicarboxylate based UiO-66 analogue: challenging larger hydrocarbon cage platforms," *CrystEngComm,* Bd. 24, p. 7530–7534, 2022.

[53] V. Gvilava, M. Vieten, T. Heinen, R. Oestreich, I. Boldog und C. Janiak, „[Zr6(μ3-O)4(μ3-OH)4](1-adamantanecarboxylate)12]: a model for extrinsic "defect-engineerable"

porosity," *Zeitschrift für anorganische und allgemeine Chemie,* Bd. 649, July 2023.

[54] T. Fleck-Kunde, E. H. Wolpert, L. z. zur, R. Oestreich, C. Janiak, K. E. Jelfs und B. M. Schmidt, „Observation of Rare Tri6Di9 Imine Cages Using Highly Fluorinated Building Blocks," *Organic Materials,* Bd. 4, p. 255–260, November 2022.

[55] T. David, R. Oestreich, T. Pausch, Y. Wada, T. Fleck-Kunde, M. Kawano, C. Janiak und B. M. Schmidt, „Fluorinated vs. non-fluorinated tetrahedral Tri4Tri4 porous organic cages for H2, CO2, and CH4 adsorption," *Chemical Communications,* Bd. 60, p. 14762–14765, 2024.

[56] T. H. Y. Beglau, L. Rademacher, R. Oestreich und C. Janiak, „Synthesis of Ketjenblack Decorated Pillared Ni(Fe) Metal-Organic Frameworks as Precursor Electrocatalysts for Enhancing the Oxygen Evolution Reaction," *Molecules,* Bd. 28, p. 4464, May 2023.

[57] S. Abdpour, M. N. A. Fetzer, R. Oestreich, T. H. Y. Beglau, I. Boldog und C. Janiak, „Bimetallic CPM-37(Ni,Fe) metal–organic framework: enhanced porosity, stability and tunable composition," *Dalton Transactions,* Bd. 53, p. 4937–4951, 2024.